

ELECTROCHEMICAL ENERGY STORAGE INTEGRATION CHALLENGES
WITHIN HIGH VOLTAGE DISTRIBUTED GENERATION POWER SYSTEM
ARCHITECTURES

by

CHARLES N. NYBECK

Presented to the Faculty of the Graduate School of
The University of Texas at Arlington in Partial Fulfillment
of the Requirements
for the Degree of

DOCTOR OF PHILOSOPHY

THE UNIVERSITY OF TEXAS AT ARLINGTON

May 2019

Copyright © by Charles N. Nybeck 2019

All Rights Reserved



Acknowledgements

I would like to start by thanking my family for their support and encouragement through my academic career. My Father, Mathew, My stepmother, Sheri, and my siblings, Tiffany, Mitch, and Megan have always been there to support me throughout my time in school.

I would also like to thank the faculty and staff of the University of Texas at Arlington for all of their guidance throughout my time in college. The knowledge I gained from classes with Dr. Ali Davoudi, Dr. Wei-Jen Lee, Dr. Rasool Kanarangui, and Dr. William Dillon gave me the ability to accomplish the work I have performed here. I am also forever grateful to Dr. David Wetz and Dr. Gregory Turner for the opportunity to work in the Pulsed Power & Energy Laboratory, where I have gained good friends and invaluable experience.

Finally, I would like to thank my colleagues that I worked with over the years - David, Brian, Clint, Matt, Alex, Chris, and Caroline. They have always been there to help me when I needed. To David and Brian, thank you guys for everything, you guys are like brothers to me and I wish you both the best of luck.

-May 1, 2019

Abstract

ELECTROCHEMICAL ENERGY STORAGE INTEGRATION CHALLENGES WITHIN HIGH VOLTAGE DISTRIBUTED GENERATION POWER SYSTEM ARCHITECTURES

Charles N. Nybeck, Ph.D.

The University of Texas at Arlington, 2019

Supervising Professor: David Wetz, PhD

Future stationary and mobile microgrids may be deployed with a number of high power electrical loads that operate transiently. The transient nature of the loads will impart high stress on a microgrid's power system, possibly pushing it outside of the acceptable power quality standards. To restore power quality and increase system reliability, it is being proposed that electrochemical energy storage systems be used as a buffer. Energy storage systems that store a great deal of energy and could be used with open circuit potentials (OCPs) as high as 1 kV. Since size and weight on a mobile microgrid is limited, it is desired that energy storage systems be designed as compactly as possible.

Lithium-ion batteries (LIBs) are among those with a great deal of promise due to their high combined power and energy density that allows them to be very versatile as both the source and sink of high power aboard a mobile platform. Lithium-ion batteries are available in many different chemistries and each offers its own advantages and disadvantages with respect to voltage, power density, energy density, impedance, and safety. In most energy storage application LIBs should be considered although they may not be the most optimal solution.

Another electrochemical energy storage option of interest is the use of ultracapacitors (UCs). Although they are not as energy dense as LIBs, they do offer very high power densities, have very low impedance, and have a long cycle life when cycled at high rates. Due to their high energy densities, LIBs are a more viable solution for loads operating in continuous modes of operation, like during operational scenarios requiring greater than a second or so of conduction. On the other hand, because of their very low equivalent series resistance (ESR), UCs are better suited for sourcing transient loads that require high power in very short duration, i.e. less than a second. The research presented here is comprised of three different tests that provide insight into electrochemical energy storage integration challenges within high voltage distributed generation power system architectures.

These energy storage systems will likely be located in a different area of the microgrid than the loads they provide power to. Long cables will be used to connect busses that provide power to different loads introducing inductance to the system based on the length and diameter of those cables. High power electrical loads combined with the inductance introduced can lead to voltage transients over the energy storage systems OCP. The transients induced may even cause damage to electrochemical energy storage devices used to buffer the load and could result in punch through on a battery's separator causing the cell to fail, possibly leading to severe damage to system components.

Battery failure often leads to thermal runaway, a process in which an increase in temperature changes the conditions in a way that causes a further increase in temperature [1]. Each of the different battery chemistries fail in a different way and each has a different level of thermal runaway volatility. When a LIB fails, the high temperature leads to an increase in pressure within the cell that causes an internal burst diaphragm to rupture in attempt to relieve pressure and prevent

further thermal increase. Rupturing of the burst diaphragm releases internal gases in the form of vented organic electrolyte compounds to the surrounding environment. The chemical makeup of the vented gas is chemistry dependent with different levels of toxicity and flammability.

In most lithium ion batteries, the electrolyte solution consists of combinations of linear and cyclic alkyl carbonates including ethylene carbonate, dimethyl, diethyl, and ethyl-methyl carbonates (EC, DMC, DEC, and EMC) as well as electrolyte salts such as LiPF_6 or LiClO_4 [2]. Over a cell's useful lifetime, the electrolyte decomposes slowly, however when they are exposed to extreme voltage or temperature conditions, the electrolytes can react rapidly with the active electrode materials to release significant heat and gas [2, 3]. Thermal runaway begins as temperatures in excess of 200°C are reached, however breakdown of the solvents can occur slightly sooner. During these processes, many different gas products are produced, most of which are hydrocarbons with various levels of toxicity and flammability. Due to the dangerous nature of electrochemical energy storage integration challenges within high voltage distributed generation power system architectures, the research presented here is comprised of three different tests that provide insight into potential methods and solutions.

Table of Contents

Acknowledgements.....	1
Abstract.....	2
List of Figures.....	8
List of Tables.....	18
Chapter 1: Introduction.....	19
Introduction to Energy Storage.....	19
Batteries.....	20
Ultracapacitors.....	21
Energy Storage Integration.....	23
Voltage Transients.....	24
Voltage Transient Suppression Techniques.....	27
Lithium-iron-phosphate Batteries and Dielectric Breakdown.....	30
Chapter 2: Ultracapacitor Characterization.....	33
Characterization Methods.....	36
Electrochemical Impedance Spectroscopy (EIS).....	36
Single Transient Discharge.....	37
Repetitive Transient Cycling.....	38
Experimental Setups.....	40
Electrochemical Impedance Spectroscopy.....	40
Single Transient Discharge.....	41

Repetitive Transient Cycling.....	43
Ultracapacitor Characterization Results.....	51
Measurement of Impedance using Electrochemical Impedance Spectroscopy (EIS) and Initial Usable Capacitance.....	51
Single Transient Discharge Results.....	54
Repetitive Transient Cycling Results	57
Ultracapacitor Model.....	72
Model Validation.....	76
Conclusion.....	80
Chapter 3: Voltage Transient Suppression	83
Voltage Transient Experimental Setup	83
Voltage Transient Suppression Results.....	86
Unprotected Transient Results	86
TVS Protected Transient Results.....	87
MOV Protected Transient Results.....	97
Active Circuit Protection Results	103
Conclusion.....	108
Chapter 4: Effect of Vented Electrolyte.....	109
Dielectric Breakdown Testbed	110
Vented Electrolyte Breakdown Results.....	113
Conclusion.....	117

Chapter 5: Final Conclusion	118
Disclaimer	120
References.....	121
Biographical Statement.....	126

List of Figures

Figure 1: Diagram of a cylindrical Li-ion battery [10].	21
Figure 2: Schematic of a double layer ultracapacitor [11].	22
Figure 3: Ragone plot showing the specific energy and power of multiple electrochemical energy storage devices [12].	23
Figure 4: Current profile (left) experimentally evaluated using a 20S/1P module of lithium-ion batteries. Photograph of the cables connecting the source to the load (right).	26
Figure 5: Transient voltage spikes measured when the current profile shown in Figure 4 were executed using the 10S/1P module.	27
Figure 6: I-V relationship of a TVS diode and a list of a few key characteristics [21].	28
Figure 7: Symmetrical non-linear I-V relationship (left) microstructure of an MOV showing grains of ZnO of average size d separated by intergranular boundaries (right) [22].	29
Figure 8: MOV surge protection is lost (left) example of dangerous construction, where failed MOV, packed too tightly between adjacent components and cannot split open (right) [23].	29
Figure 9: Detected components of produced gases (mol%) [25].	31
Figure 10: Paschen curves for five different gases [27].	32
Figure 11: Picture of the UC modules used in this experiment along with some of their key characteristics.	35
Figure 12: The Autolab PGSTAT302N used in this experiment, along with some of its key features.	37

Figure 13: CAD drawing of the custom experimental testbed (left) along with a photograph of the testbed containing a Maxwell 3000 F cell (right). 38

Figure 14: Photographs of the programmable load and supplies used to cycle the cells and modules for this experiment..... 39

Figure 15: Photographs of the Maxwell (top left), Ioxus (top second left), JM Energy (top third left), Skeleton (top right), and General Capacitor (bottom) set up for initial characterization from the PGSTAT302N. 41

Figure 16: The single transient discharge experimental testbed with a cylindrical Maxwell (left) and prismatic JM Energy (right) cell firmly placed between the top and bottom plates. 42

Figure 17: Sample photographs of the Ioxus (upper left), Skeleton (upper right), Maxwell (middle left), JM Energy (middle right), and General Capacitor (bottom) cells prior to evaluation showing both the terminals and their connection to bus work..... 44

Figure 18: Maxwell 48 V module with the thermocouple placement (left) and the module inside the temperature chamber set up for testing. 46

Figure 19: Ioxus 48 V module opened up (left) fully instrumented inside the temperature chamber (middle), and the calibration data collected and calculated equation used to relate the module’s internal thermistor voltage to its respective temperature (right). 46

Figure 20: JM Energy 45 V module fully disassembled (left) to place thermocouples of the body of multiple cells (center). The module with multiple cells instrumented and reassembled (right)..... 47

Figure 21: Skelton 48 V module (technically it has a datasheet rating of 51 V)..... 49

Figure 22: Ioxus 96 V module instrumented inside the temperature chamber (left), in an ambient environment (middle), and the calibration data collected and calculated equation used to relate the module’s internal thermistor voltage to its respective temperature (right).
..... 50

Figure 23: Skeleton 170 V module sitting in an ambient environment, being cycled..... 50

Figure 24: Each of the UCs charge curves vs time (left) and their associated voltage curves (right). 51

Figure 25: Electrochemical impedance spectroscopy (EIS) measurements made from each respective type of cell studied including the SCA3200 (upper left), Ioxus iRB3000K270CT (upper right), Maxwell BCAP3400 (middle left), JM Energy Ultimo 3300F prismatic (middle right), and the General Capacitor 3000F (bottom), as a function of their charge voltage in 10% increments. 54

Figure 26: Single transient discharge voltage profiles for each of the cells (left) and their corresponding current profiles (right)..... 55

Figure 27: Plot of the power supplied by each cell (left) and each cell’s ESR vs the power supplied (right)..... 56

Figure 28: Voltage measurements made from each respective type of cell studied including the Ioxus iRB3000K270CT (upper left), JM Energy Ultimo 3300F prismatic (upper right), Maxwell BCAP3400 (middle left), Skeleton SCA3200 (middle right), and the General Capacitor 3000F (bottom), when subject to the repetitive transient procedure at 200 A..... 57

Figure 29: Thermal measurements made from each respective type of cell studied including the Skeleton SCA3200 (upper left), JM Energy Ultimo 3300F prismatic (upper right),

Ioxus iRB3000K270CT (middle left), Maxwell BCAP3400 (middle right), and the General Capacitor 3000F (bottom).	60
Figure 30: Voltage measurements made from each respective UC module studied including the Ioxus iMOD048V166A23 (top left), JM Energy Ultimo 3300F prismatic (top right), Maxwell BMOD0165 P048 C01 (bottom left), and SMOD48V178F (bottom right), when subject to the repetitive transient procedure at 200 A.	60
Figure 31: Thermal data gathered when cycling the Maxwell 48 V at 100 A (top left), 200A (top right), and 250 A (bottom).	61
Figure 32: Thermal data gathered when cycling the Ioxus 48 V at 100 A (top left), 200A (top right), 250 A (bottom left), and 300 A (bottom right).	62
Figure 33: Thermal data gathered when cycling the JM Energy 45 V module at 100 A.	63
Figure 34: Thermal data gathered when cycling the Skeleton 51 V at 100 A (top left), 200A (top right), 250 A (bottom left), and 300 A (bottom right).	64
Figure 35: Voltage measurements made from each respective UC module studied including the Ioxus iMOD096V083A23-LQ (left) and the Skeleton SMOD170V53F (right), when subject to the repetitive transient procedure at 200 A.	66
Figure 36: Thermal data collected when cycling the Ioxus 96 V module at 100 A (top left), 200A (top right), 250 A (bottom left), and 300 A (bottom right), in ambient room conditions with liquid cooling.	67
Figure 37: Thermal data gathered when cycling the Ioxus 96 V module at 100 A (top left), 200A (top right), 250 A (bottom left), and 300 A (bottom right), in an open room environment and without the use of liquid cooling.	68

Figure 38: Thermal data gathered when cycling the Skeleton 170 V module at 100 A (top left), 200A (top right), 250 A (bottom left), and 300 A (bottom right), in an open room environment and with the use of liquid cooling..... 70

Figure 39: Thermal data gathered when cycling the Skeleton 170 V module at 100 A (top left), 200A (top right), 250 A (bottom left), and 300 A (bottom right), in an open room environment and without the use of liquid cooling. 71

Figure 40: Diagram of an equivalent circuit representing the ultracapacitor model [31]..... 72

Figure 41: Diagram of the Stern model representing the output UC voltage seen in equation 3. 74

Figure 42: Diagram showing the time bounds used in equation 5 to determine the UC’s self-discharge current [31]. 74

Figure 43: Diagram of the self-discharge model representing the UC self -discharge equation 5. 75

Figure 44: Diagram of the UC model incorporating the Stern and self-discharge models..... 75

Figure 45: Diagram of the UC model simulating the single transient discharge experiment for each of the five UCs tested. 76

Figure 46: Comparison between the simulated and recorded transient discharge voltage profiles. 77

Figure 47: Comparison between the simulated and recorded transient discharge current profiles. 77

Figure 48: Comparison between the simulated and recorded repetitively cycled voltage profiles for the Ioxus EDLC when cycled at 200 A..... 78

Figure 49: Comparison between the simulated and recorded repetitively cycled voltage profiles for the Skeleton EDLC when cycled at 200 A..... 78

Figure 50: Comparison between the simulated and recorded repetitively cycled voltage profiles for the Maxwell EDLC when cycled at 200 A.	79
Figure 51: Comparison between the simulated and recorded repetitively cycled voltage profiles for the JM Energy LIC when cycled at 200 A.	79
Figure 52: Comparison between the simulated and recorded repetitively cycled voltage profiles for the General Capacitor LIC when cycled at 100 A.	79
Figure 53: The battery module in a 10S/1P configuration with BMS board attached.....	83
Figure 54: The NI-USB-6211 multifunction IO device used to control the load and supplies (left) the Chroma load used for discharge current (middle) one of the two Chroma supplies used for the charge current (right).	84
Figure 55: The schematic of the experimental setup (left) a photograph of the experimental setup used to produce voltage transients (right).....	86
Figure 56: Output from the system modeling the use of the shorter cables with an inductance of 6.8 μ H (top) and 8.82 μ H cables (below).	86
Figure 57: Current (above) and voltage (below) profiles for 465 cm cable (left) and 584 cm cable (right) respectively.....	87
Figure 58: Simulation results of (A) 15KPA33CA using 465 cm long cable, (B) 15KPA33CA using 584 cm long cable, (C) 15KPA40CA using 465 cm long cable and (D) 15KPA40CA using 584 cm long cable.....	90
Figure 59: The system setup using the 15KPA33CA, differential voltage probes, and current meter.	91
Figure 60: The transient voltage profile using the 15KPA33CA for suppression (left) the current shunted through the TVS diode (right).	92

Figure 61: The power consumed by the 15KPA33CA for each voltage transient produced (left) the power consumed integrated to energy of the same profile, both calculated using the equations 7 and 8 respectively (right). 92

Figure 62: 15KPA33CA with a T-type thermocouple thermal epoxied to the diode for temperature measurements (left) three tests showing the temperature rise of the TVS diode during the 60 cycle tests (right)..... 93

Figure 63: Transient voltage profile recorded during the last two of the 60 cycle test using the 15KPA33CA diode. 94

Figure 64: With the module nearly at peak charge the temperature started to increase drastically over long term use (left) the voltage suppression is identical to when the module was charged to its nominal voltage (right). 95

Figure 65: Transient voltage profile using the 15KPA40CA and the 584 cm cable (left) the current shunted by the 15KPA40CA (right). 95

Figure 66: The 15KPA40CA with a T-type thermocouple thermal epoxied to the diode for temperature measurements (left) three tests showing the temperature rise of the TVS diode during the 60 cycle tests (right)..... 96

Figure 67: Transient voltages recorded (left) and current recorded through the 15KPA40CA diode (right) during the last few cycles of a repetitive experiment using two identical diodes in two different experiments to demonstrate consistency of the TVS diode... 97

Figure 68: The V10E23P placed parallel to the bus with the differential voltage probes and the clamped-on current meter (left) the V07E30P with the same exact set up (middle) the V20E35P also with the same exact set up (right). 99

Figure 69: Transient voltage profiles measured during three tests performed using a 465 cm cable and a V10E23P MOV. Voltage (left) and MOV current (right) are shown. 99

Figure 70: Transient voltage profiles measured during three tests performed using a 584 cm cable and a V10E23P MOV. Voltage (left) and MOV current (right) are shown. 100

Figure 71: Transient voltage profiles measured during three tests performed using a 465 cm cable and a V07E30P MOV. Voltage (left) and MOV current (right) are shown. 100

Figure 72: Transient voltage profiles measured during three tests performed using a 584 cm cable and a V07E30P MOV. Voltage (left) and MOV current (right) are shown. 101

Figure 73: Transient voltage profiles measured during three tests performed using a 465 cm cable and a V20E35P MOV. Voltage (left) and MOV current (right) are shown. 101

Figure 74: Transient voltage profiles measured during three tests performed using a 584 cm cable and a V20E35P MOV. Voltage (left) and MOV current (right) are shown. 102

Figure 75: V10E23P with a T-type thermocouple attached using thermal epoxy for temperature measurements during the 60 cycle test (left) three temperature measurements of the V10E23P while clamping voltage transients during the 60 cycle tests (right). 102

Figure 76: Transient voltage profiles of the last two cycles during the 60 cycle test (left) current shunted by the V10E23P corresponding to the transient voltage profiles (right)..... 103

Figure 77: Circuit diagram of one active voltage transient suppression topology. 104

Figure 78: LTSPICE simulation results obtained from the active circuit topology shown in Figure 30. 105

Figure 79: Active voltage transient suppression device designed to mitigate voltage spikes. Photos of the protoboard circuit (left) and the PCB layout of the same circuit (right) are shown. 105

Figure 80: Voltage (left) and power resistor current (right) waveforms recorded from three experiments performed using the active suppression circuit shown in Figure 31. ...	106
Figure 81: Schematic of the active transient suppression design using logic for a variable clamping voltage.....	107
Figure 82: Photograph of the active transient suppression design shown in Figure 81 constructed on a protoboard.	107
Figure 83: Voltage (left) and power resistor current (right) waveforms recorded from three experiments performed using the revised active suppression circuit.....	108
Figure 84: Schematic of the dielectric breakdown test setup.	110
Figure 85: Photograph of the entire dielectric breakdown test setup.....	111
Figure 86: Photograph of the UTA dielectric breakdown experimental circuit setup.....	111
Figure 87: Sealed acrylic chamber containing electrodes used to induce voltage breakdown. ...	112
Figure 88: Pipe housing, heat tape, and LiFePO ₄ cell setup used to direct vented gas into the acrylic test chamber.	113
Figure 89: Breakdown voltage as a function of average gap distance. Error bars represent the standard deviation recorded over five measurements with each applied voltage.	114
Figure 90: Breakdown voltage plotted as a function of the product of chamber pressure and breakdown gap distance, for both experimental and calculated data.....	115
Figure 91: Breakdown distance measured multiple times from three identical vented LFP cells as well as ambient air, respectively, with an applied gap potential of 0.75 kV.	116
Figure 92: Breakdown distance measured multiple times from three identical vented LFP cells as well as ambient air, respectively, with an applied gap potential of 1.0 kV.	116

Figure 93: Breakdown distance measured multiple times from three identical vented LFP cells as well as ambient air, respectively, with an applied gap potential of 1.25 kV. 117

List of Tables

Table 1: List of the four experiments performed in this study.	34
Table 2: Ultracapacitor (UC) cells and their electrical properties given by their datasheets.	35
Table 3: Ultracapacitor (UC) modules and their electrical properties given by their datasheets.	36
Table 4: 48 V Skeleton Module CAN bus protocol.....	48
Table 5: Summary of the impedance, current, voltage, power, and power density values, respectively, measured during the single transient discharge experiments.	56
Table 6: The characteristics of the two tested TVS diodes, the 15KPA33CA and the 15KPA40CA.....	88
Table 7: The electrical characteristics for the MOVs used in this experiment, the V10E23P, V07E30P, and V20E35P.....	98

Chapter 1: Introduction

Introduction to Energy Storage

An effective means to store energy for on demand use has been sought and researched since Benjamin Franklin proved that lightning was electricity in 1752 [4]. In fact, Luigi Galvani and Alessandro Conte di Volta were both inadvertently working towards this goal in the late 1700's. Galvani discovered animal electricity, noticing that during his experiments a deceased frog's leg muscles would twitch from sparks created by contact with different metals. This phenomenon would later be known as galvanism, named after Galvani and his wife. Meanwhile his intellectual rival, Alessandro Volta, repeated Galvani's studies and determined that the frog's leg was serving as a conductor of electricity between two metals. Volta then began experimenting with metals in order to determine the effects of different metals placed in certain salt solutions. This led to the invention of the first modern energy storage device, a battery that Volta revealed to the Royal Society in London in 1800. The battery consisted of two electrodes, one made of zinc and the other of copper, separated by paper that was either saltwater or sodium hydroxide. This battery proved to be a steady source of electric current that did not need to be recharged like previous inventions and ultimately led to the creation of the field electrochemistry [5].

There are several different methods of energy storage, a few include mechanical, thermal, and electrochemical energy storage that each contain many different techniques. For example, one mechanical energy storage technique is hydroelectricity, water stored in reservoirs to be released at time when energy demands are high. Another method of mechanical energy storage is flywheel energy storage, rotational energy stored by accelerating a rotating disk at high speeds. One example of a thermal energy storage technique is seasonal thermal energy storage, storing thermal energy to be used months after the season passes. An example of an electrochemical energy storage

technique was mentioned earlier; rechargeable batteries utilize two metal electrodes separated by electrolyte to create a device to store electrical energy. Another method of electrochemical energy storage is the use of ultracapacitors, which stores energy electrostatically between two parallel metal electrodes separated by a very small distance. These methods of energy storage all have one common use, they are used to buffer existing electrical systems when energy is demanded. Microgrids are one promising area in which energy storage systems are used as a buffer between existing power generation and load demands [6-8].

Batteries

Batteries are one of the primary methods of electrochemical energy storage that is of interest for use in microgrid applications. As previously mentioned, batteries are comprised of three main components, two metal electrodes that are immersed in electrolyte. The electrolyte acts as a chemical medium that allows current to flow between the cells cathode and anode. During a battery's discharge, the electrolyte touching the anode releases electrons that move toward the negative terminal and ions in the electrolyte through redox reactions. The cathode accepts the electrons released from the redox reaction and completes the circuit for the flow of electrons through the battery. Rechargeable batteries are designed in such a way that electrical energy from outside the battery can be applied to the cell causing the operation to reverse and restore its energy [9].

Rechargeable batteries can be designed using different chemistries to achieve certain characteristics. There are four major types of rechargeable batteries, nickel-cadmium (Ni-Cd), nickel-metal hydride (Ni-MH), lead-acid, and lithium-ion (Li-ion), each with their own advantages and disadvantages. One chemistry of special interest for use in energy storage systems is lithium-ion. Lithium-ion batteries possess high energy density and offer the best

performance to weight ratio compared to the other chemistries. Figure 1 below contains a diagram of a cylindrical Li-ion battery [10].

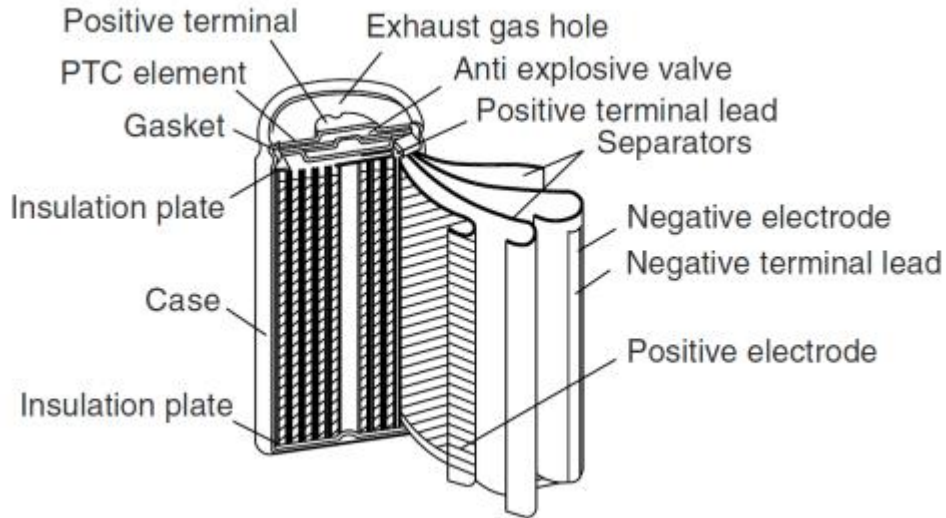


Figure 1: Diagram of a cylindrical Li-ion battery [10].

Figure 1 shows a diagram of a cylindrical Li-ion battery with the cathode and anode separated by a thin separator that is rolled into the cell body. The cathode is connected to the steel can and the anode is connected to the top cap creating the cells two terminals that are both immersed in the electrolyte solution allowing current to flow through the battery.

Ultracapacitors

Another electrochemical energy storage option of particular interest for microgrid applications are ultracapacitors. Unlike conventional capacitors, a UC's current collectors are coated with a sponge-like, porous activated carbon that significantly increases the collector's surface area and therefore also its capacitance. They are comprised of two electrodes, anode and cathode, that are immersed in electrolyte. A separator electrically isolates and ionically connects the two electrodes. When charged, UCs form a phenomenon called an 'electric double layer' (EDL) that consists of two layers of charges separated by a very thin dielectric layer. The separation distance between

the electrode surfaces to the center of the ion layer is in the order of a few angstroms, significantly increasing the capacitance but limiting the working voltage to typically no higher than 3 V. A schematic of an ultracapacitor can be seen in Figure 2 [11]. EDLCs typically have an extremely low ESR, typically well less than 1 m Ω . Another extremely important aspect of UCs is their safety, as they do not experience thermal runaway or volatile failures when overcharged. Instead UCs typically release pressure in a non-violent reaction.

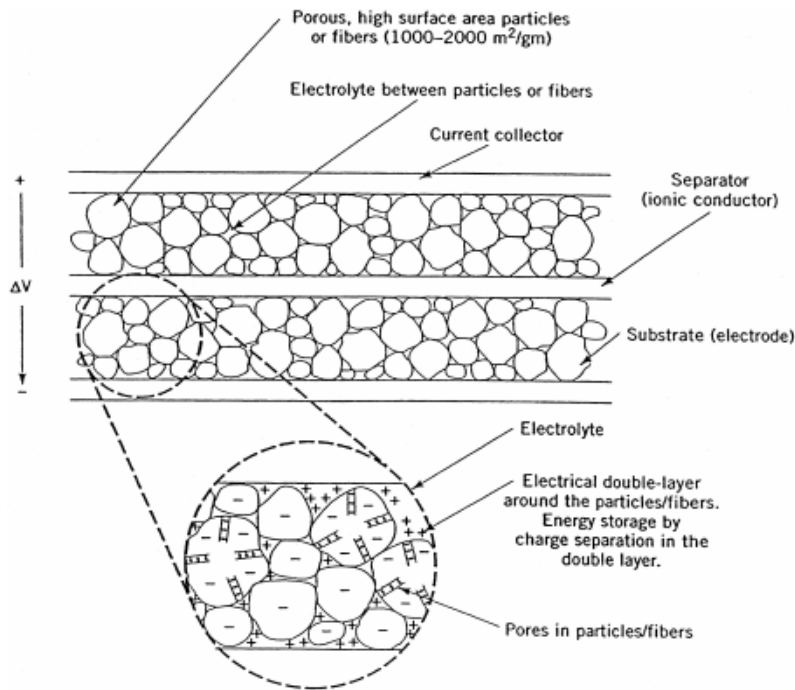


Figure 2: Schematic of a double layer ultracapacitor [11].

Another ultracapacitor topology of extreme interest is a hybrid device that has properties from both UCs and LIBs, called lithium-ion capacitors (LICs). LICs are comprised of a pre-doped carbon anode, similar to that of a Li-ion battery, and an activated carbon cathode, similar to other UCs. The result is an asymmetric capacitor that has a higher operational voltage than most UCs, roughly four times the energy density of most UCs, and also a minimum voltage of 2 V, similar to that of LIBs. Due to their battery-like properties, LICs have a higher ESR than EDLCs, although

it is still in the order of a few mΩ. Figure 3 plots a comparison of the energy and power densities of many different energy storage devices including rechargeable batteries and UCs [12]. Extensive literature has been published studying and characterizing batteries but little has been done to study emerging UCs and how they fit into prime power supplies [13]. Therefore, the work presented here will focus on the characterization on UCs for integration into high voltage distributed generation power system architectures.

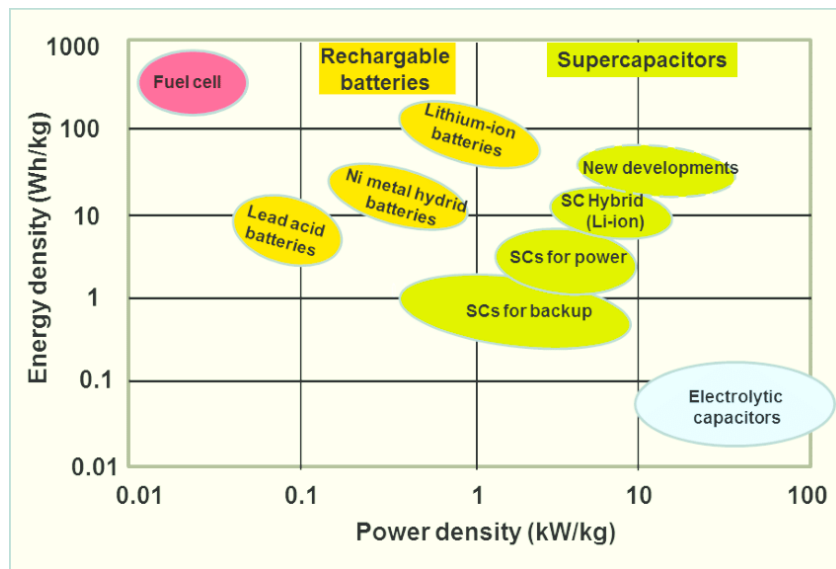


Figure 3: Ragone plot showing the specific energy and power of multiple electrochemical energy storage devices [12].

Energy Storage Integration

Future stationary and mobile microgrids may contain several unique high power loads which will be operated in both continuous and transient modes of operation [14, 15]. When transient loads are sourced, they drag down their source's DC or AC bus voltage considerably, heavily impacting power quality. While generators alone can likely be sized properly to account for large transient loads, they will be considerably large taking up valuable space in mobile microgrids that is desperately needed for other equipment. With this in mind, DC and AC sources can be integrated

into unique power system architectures that employ energy generation and storage capable of working together to supply power to the intermittent loads. The use of energy storage to buffer the generation minimized variations in generator output power allowing its power quality to be maintained [16-19]. Power system architectures which combine both electrochemical batteries, ultracapacitors, and the standard AC generation are preferred [18, 19]. This leads to both DC and AC buses existing in the architecture, requiring active power conversion between DC and AC sources. This is not a new challenge, as it is faced every day while power systems engineers try to integrate batteries, solar panels, and wind turbines onto the already existing electrical grid. The loads being sourced in those applications are different than those being sourced by a future stationary and mobile microgrids and therefore special attention and research is needed to understand how to overcome these challenges.

Voltage Transients

Once integrated into a combined power system, the energy storage system will supply high currents to transiently operated loads. As it would be optimal to locate the energy storage systems very close to the load, it is almost always impossible to do so. As a result long cables will be used to carry current from the energy storage to the load. Long cables translates into high equivalent resistances and inductances being placed in series with the energy storage and the load. The high slew rate of the transient loads coupled with the high currents being carried will result in large inductive voltage spikes being induced on the transmission system. A similar phenomena will be observed in the event of a high current protective fuse opening. The spikes are induced according to equation 1. While this problem is challenging enough to overcome, it is proposed that energy storage systems be implemented with open circuit potentials (OCP) in excess of 1 kV. High voltage spikes induced on top of this already high OCP can result in dangerously high voltage transients

occurring that can easily punch through electrical insulation. If this occurs, it can result in the formation of short circuits that bypass safety devices and quickly deplete the batteries at high current rates. These events could have very serious consequences and therefore proper understanding of how to mitigate them is necessary.

$$V_S = L \times \frac{di}{dt} (V) \quad (1)$$

In 2015, experiments were conducted using a current profile containing abrupt changes to simulate a specified load profile. While conducting these experiments it became clear the severity of these voltage transients were greater than expected. The transients encountered caused the programmable loads used to shut down and ultimately halted the experiment. The experiment was first conducted using a 20S/1P module of 30 Ah lithium-ion batteries evaluated under the current profile seen in the left side of Figure 4. There are portions of this waveform that have not been approved for public release, therefore those portions have been whited out and not shown in the following discussion. The work discussed here is aimed at mitigating the transients seen in the beginning and the end of the profile. Notice in the profile the abrupt changes in current which are the cause of the voltage transients produced. To the right of the transient profile is a photograph of the bus work connecting the battery to the programmable load. The current profile is comprised of a short discharge of 300 A, followed by a short recharge of 750 A to return the energy drained from the module. When attempting the experiment using the 20S/1P module transients as high as 113 V were observed. Keep in mind that the OCP of the battery is only 76 V. The Chroma programmable loads have a maximum rated voltage of 80 V, but contain their own internal transient protection that prevented any serious damage. To better understand the problem at hand, a 10S/1P battery was experimentally studied. In those experiments, transients were observed with peak voltages just under 90 V which allowed the load to remain operational. Figure 5 zooms in on

one of the voltage transient profiles measured from a 10S/1P battery when it was evaluated using the current profile from Figure 4. Note that in this case the OCP of the module used is only 38 V. Voltage transients such as these are extremely concerning considering the voltage spike produced is over twice the OCP of the module. If similar scale transients were to occur on 1 kV battery, they could exceed 2 kV and would be extremely dangerous to equipment and personnel. This prompted the investigation performed here that is aimed at evaluating different methods of voltage transient suppression to study their effectiveness. In this particular study three different voltage transient suppression techniques have been evaluated. These include transient voltage suppression (TVS) diodes, metal oxide varistors (MOV's), and an active voltage suppression circuit, respectively.

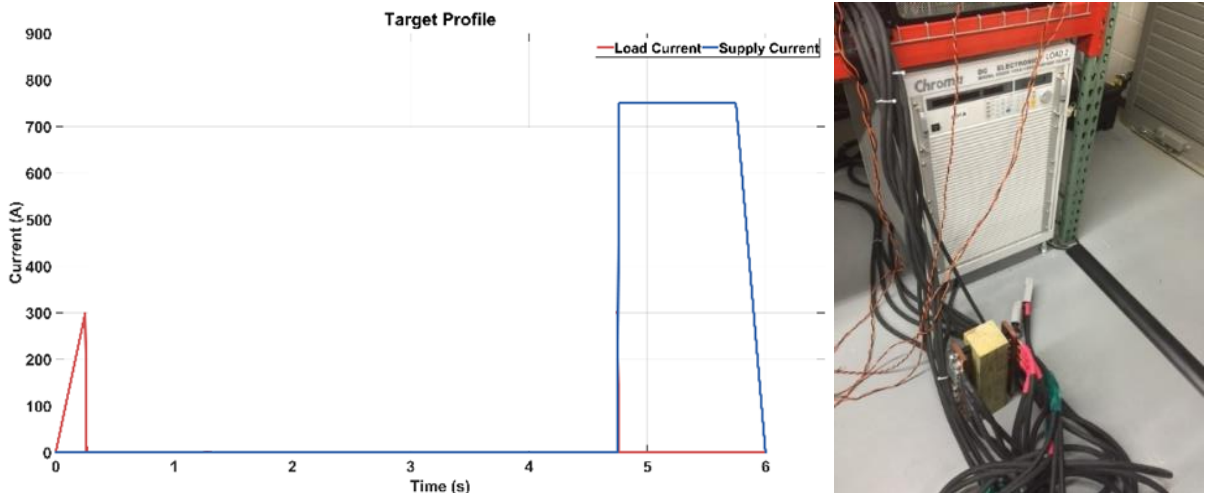


Figure 4: Current profile (left) experimentally evaluated using a 20S/1P module of lithium-ion batteries. Photograph of the cables connecting the source to the load (right).

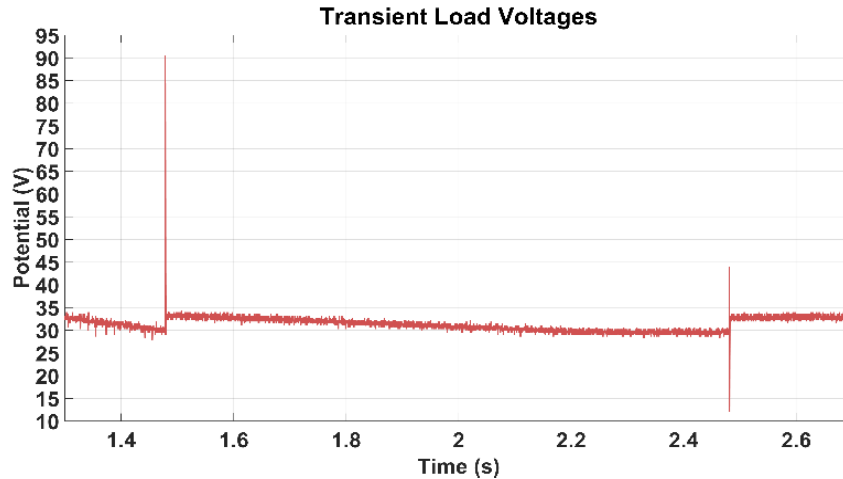


Figure 5: Transient voltage spikes measured when the current profile shown in Figure 4 were executed using the 10S/1P module.

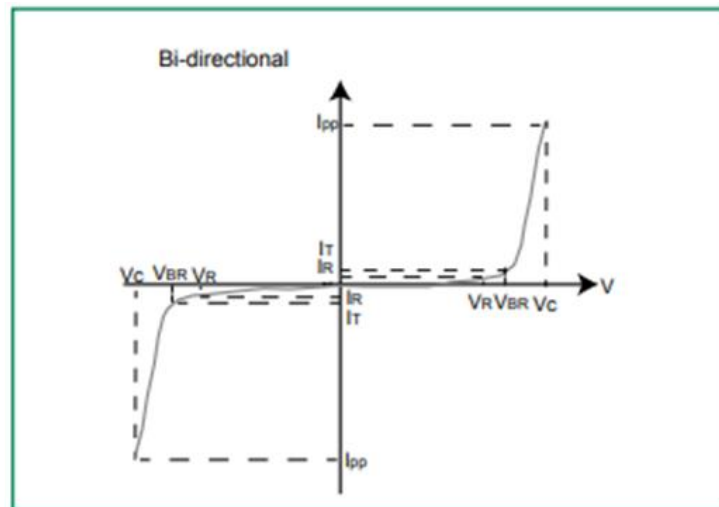
Voltage Transient Suppression Techniques

TVS Diodes

As mentioned, energy storage systems could be implemented with open circuit potentials (OCP) in excess of 1 kV and could cause catastrophic damage if a voltage transient were to occur. Therefore it is necessary to investigate different methods of transient suppression. The first suppression method to be discussed is the use of TVS diodes, which are solid state p-n junction devices designed to protect sensitive semiconductors from the damaging effects of transient voltage spikes. A TVS diode's electrical characteristics are primarily based on factors such as junction area, doping concentration, and substrate resistivity [20]. A TVS diode is able to clamp voltage by shunting current when the induced voltage is greater than the diodes avalanche potential. The clamping voltage is adjusted by varying the carrier doping levels within the diode. Figure 6 contains the I-V relationship for a bidirectional TVS diode, which shows the nonlinear relationship between voltage and current [21]. TVS diodes are known for having fast turn on times, typically 1-5 ns which results in a lower clamping voltage, but their switch off times are slightly slower and can result in extra power to be dissipated through the diode. If properly sized, a TVS

diode's performance is not significantly degraded with lifetime and the number of transients applied. It is important to note that the failure mode of a TVS diode is a short circuit, typically caused by over-specified voltage or current causing the device's p-n junction to quickly raise in temperature.

TVS diodes are offered at discretely incremented clamping voltages by most manufacturers. This is a bit of a problem if the voltages offered do not align well with the users intended application. Often a 'next best' solution must be adopted resulting in the allowance of transients that are slightly higher than desired. In many cases this is not problematic but it will of course compound if multiple devices must be combined in series for example.



- V_r Stand-off Voltage** – Maximum voltage that can be applied to the TVS without operation
- V_{BR} Breakdown Voltage** – Maximum current that flows through the TVS at a specified test current (I_T)
- V_c Clamping Voltage** – Peak voltage measured across the suppressor at a specified I_{ppm} (peak impulse current)
- I_r Reverse Leakage Current** – Current measured at V_r

Figure 6: I-V relationship of a TVS diode and a list of a few key characteristics [21].

Metal Oxide Varistors

The second protection method to be discussed is known as MOVs, which are essentially variable resistors, or varistors. Similar to TVS diodes, MOVs have a non-linear I-V curve, seen in Figure 7. Their body structure consists of ZnO grains separated by grain boundaries which provide p-n

junction characteristics. These boundaries are responsible for blocking conduction up to a certain voltage and are the source of the nonlinear electrical conduction at higher voltages [22].

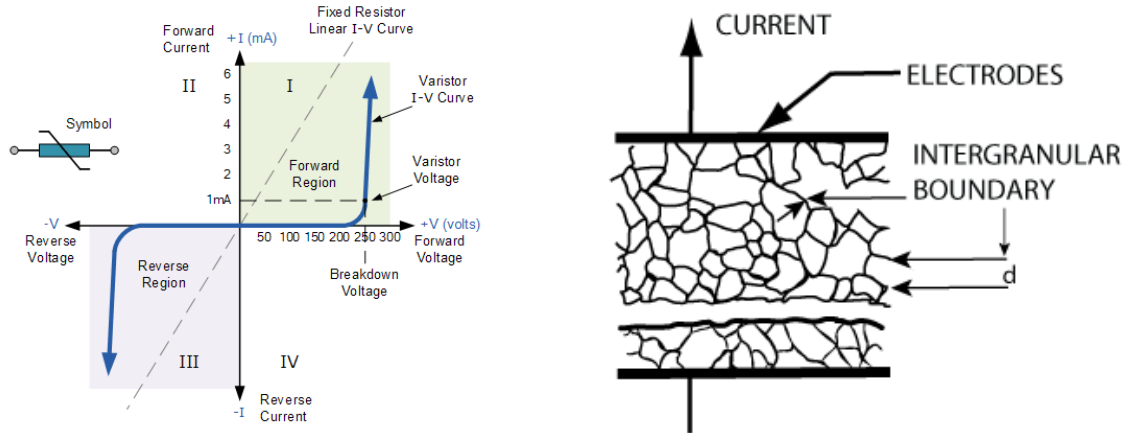


Figure 7: Symmetrical non-linear I-V relationship (left) microstructure of an MOV showing grains of ZnO of average size d separated by intergranular boundaries (right) [22].

MOVs tend to be able to dissipate more power at a smaller form factor and at a lower cost than TVS diodes. However unlike TVS diodes, their degradation is inversely proportional to the volume of the device. The data sheet for a specific device typically provides an approximate number of surges it can handle before failing. MOVs can fail as either an open circuit or, most often, a short circuit depending on the operating conditions and can result in the device exploding or catching fire as shown in Figure 8 [23].

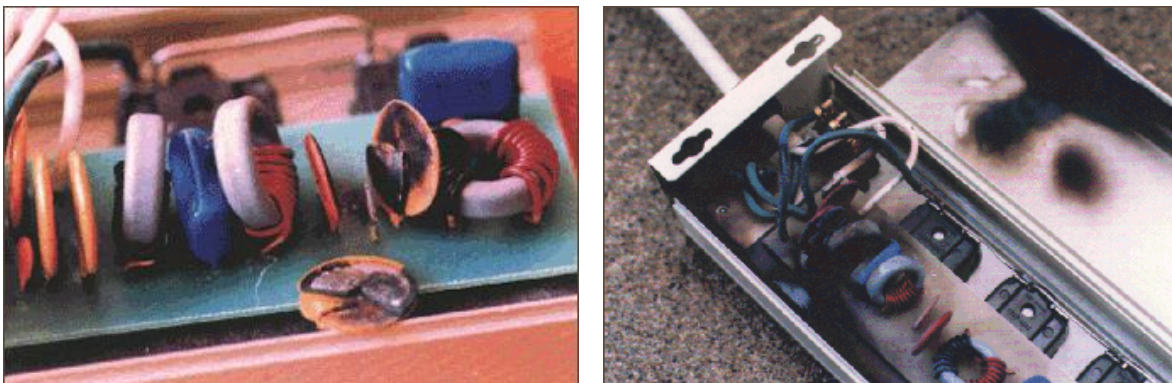


Figure 8: MOV surge protection is lost (left) example of dangerous construction, where failed MOV, packed too tightly between adjacent components and cannot split open (right) [23].

Active Suppression Technologies

The third method of voltage transient suppression explored in this work is an active design utilizing electronic components. The above mentioned methods of suppression use discrete components whereas with an active suppression design the voltage transient is suppressed using active components, such as logic ICs and MOSFETs. Active clamping brings some advantages including the ability to be adjusted by the user to meet dynamically changing requirements. A disadvantage they have is that they often have switching characteristics that are also transient in nature and therefore lack the same sort of nonlinear I-V curve that the TVS and MOV technologies offer. In the work performed here, a couple different active topologies have been designed and studied.

Lithium-iron-phosphate Batteries and Dielectric Breakdown

As mentioned earlier many different battery chemistries are currently being considered for use in electrochemical energy storage systems. One specific chemistry within the Li-ion blanket chemistry that is strongly being considered is lithium-iron-phosphate (LFP). The olivine LFP chemistry is safer than other layered or spinel battery chemistries but the increased safety comes with a reduced energy density in comparison with other chemistries. The Fe–P–O bond is stronger than the Co–O bond, so that when they are abused, the oxygen atoms are much harder to remove which reduces thermal runaway [24]. Venting of a lithium-ion cell can occur for a variety of reasons. One way that this can happen is when a cell develops an internal short circuit, which can cause it to heat up and build up excess internal pressure. External factors can also result in a cell becoming too hot, causing the cell to possibly vent. Another way that a cell can vent is from a situation that results in overcharging, which can cause the electrolyte's dielectric strength to be broken down. Previous research, Figure 9, has shown that when the LFP chemistry vents the gas

released is made up primarily of carbon dioxide (CO₂), hydrogen (H₂), and ethene (C₂H₄), along with a few others in smaller proportions [25]. These proportions have been validated with in-house research. How these gases affect the dielectric strength of a background gas is presently undocumented and must be studied as batteries are used more often in stationary and mobile microgrid applications.

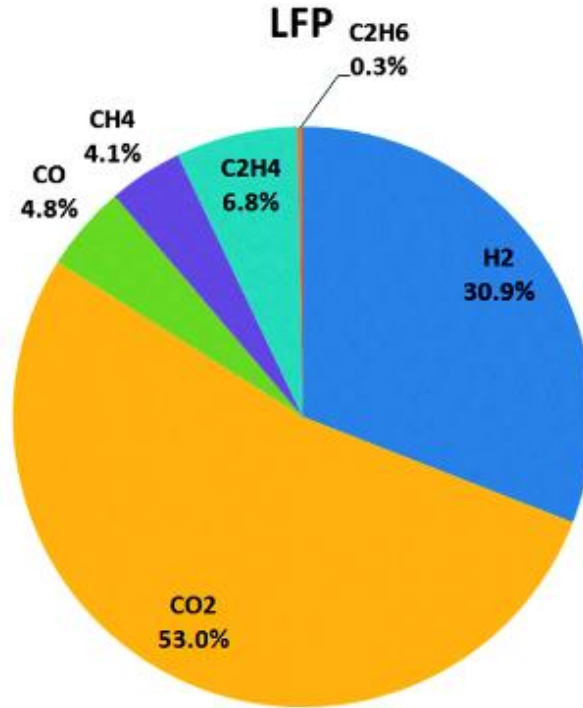


Figure 9: Detected components of produced gases (mol%) [25].

In 1889, Friedrich Paschen published what is now known as Paschen’s Law in which the breakdown voltage between two electrodes is a function of the product of chamber pressure and the distance between the electrodes [25, 26]. The Paschen equation is written as

$$V_B = \frac{B \times pd}{\ln\left(\frac{A \times pd}{\ln\left(\frac{1}{\gamma}\right)}\right)} \quad (2)$$

where V_B is the gap breakdown voltage in V, A and B are gas dependent constants, γ is the secondary electron emission coefficient or the number of secondary electrons produced per

incident positive ion, p is the gap pressure, and d is the distance between the two electrodes, respectively. Breakdown in a gas occurs as a result of free electrons colliding with neutral atoms as they accelerate from the cathode to the anode, due to the application of an electric field. At low pressure, the number of neutral ions present for ionization are low, decreasing the probability of streamer formation and breakdown occurring. At high pressures, the number of neutral ions is high, decreasing the ionization mean free path and the number of ions created, decreasing the likelihood for breakdown. The Paschen minimum defines the pressure-distance product, pd , that is optimum for breakdown to occur. Figure 10 plots the Paschen curve for a few different gases [27].

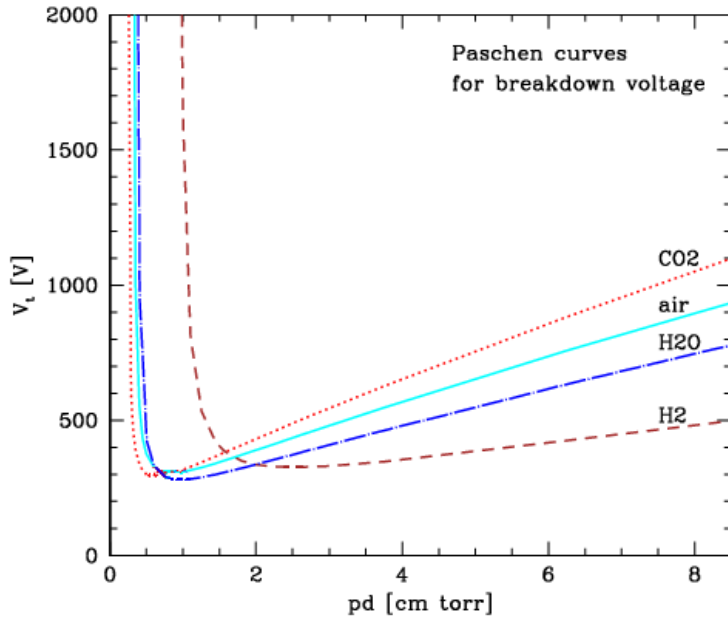


Figure 10: Paschen curves for five different gases [27].

In Figure 10, the respective Paschen curves for air, H₂, and CO₂, are all plotted. For a given pd product in the linear region, CO₂ has the highest breakdown voltage while H₂ has the lowest [27-29]. Since vented LFP electrolyte is almost entirely CO₂ and H₂, it could be hypothesized that its Paschen curve will resemble that of air. Speculation could be made that the breakdown potential may be slightly higher than that of air given that CO₂ is in slightly higher volume than H₂, however the other smaller gas players are unknown contributors, making it critical that the breakdown

potential be empirically studied. The work presented here will only investigate the impact the vented gas has on the ambient pressure condition, though ultimately, its impact across a full pressure range is of interest. As will be shown later, the pd products studied here range between 5 cm*torr and 35 cm*torr, placing them in the linear region shown Figure 10.

Chapter 2: Ultracapacitor Characterization

Technological advancements in UC and LIC technology has brought the necessity to evaluate and compare numerous technologies that are commercially available in order to better understand how well they perform under high power operation. In this experiment, research was performed to identify manufacturers who offer EDLC and LIC cells, with similar properties and characteristics so that a like-for-like comparison could be made. Maxwell, Ioxus, JM Energy, General Capacitor, and Skeleton, have been identified as viable manufacturers. Maxwell, Ioxus, and Skeleton each manufacture their representative type of EDLC whereas JM Energy and General Capacitor each make their own LICs. Cells and modules have been obtained from each of these manufacturers for study. Of the four manufacturers, Skeleton Technologies is of particular interest due to their use of curved graphene to coat their electrodes instead of regular activated carbon. This allows their cells to achieve a much lower ESR and therefore a higher power density than other similar cells.

The cells and modules procured in this effort were chosen to represent the most recent advanced technology that commercial UCs have to offer. Figure 11 contains pictures and detail some of the key characteristics of each of the cells and modules that were chosen for study. A more detailed list of each cell and modules' properties can be seen in Tables 2 and 3, respectively. At the cell level, each manufacturer's highest capacitance cell has been studied due to its ability to supply the highest power. The modules chosen are those offered at the 48 V level and are constructed from the same high capacitance cells offered by each manufacturer. Finally, a few higher voltage

modules, which again utilize the same high capacitance cells, were also procured for study. Each cell and module has a number of highlighted electrical characteristics that are of particular interest, the color is determined by comparison with the other cells or modules being studied. If highlighted in green then that cell or module's characteristic is better than the others compared, if highlighted yellow than it is considered average, and finally if highlighted red than that characteristic is worse than the other compared cells or modules. The work performed here was aimed at electrically and thermally characterizing these UCs in an effort to validate these datasheet properties and ultimately create a model of each of the UCs using Simulink and the data gathered during the experiments conducted. This study consists of three separate experiments, each of which will be described later and are listed as follows:

Table 1: List of the three experiments performed in this study.

Experiment Number	Type of Experiment
1	Initial capacitance and impedance characterization using electrochemical impedance spectroscopy (EIS)
2	Single transient discharge into near matched loads to evaluate transient power density
3	Repetitive transient cycling to evaluate repeated electrical and thermal equilibrium



2.85 V/3400F Cell
ESR 0.22/0.28 mΩ
Peak pulsed current of 2.0 kA
Peak cont. current of 211 A
E_{MAX} = 3.95 Whr



2.7 – 2.85V/3000F Cylindrical Titan HT Cell
ESR of 0.17/0.26mΩ
Peak pulsed current of 2.7kA
Peak cont. current of 139 A
E_{MAX} = 3.18Whr



2.85 V/3200F Cylindrical Cell
ESR of 0.13 mΩ
Peak pulsed current of 3.2 kA
Peak cont. current of 387 A
E_{MAX} = 3.61 Whr
FCT FUNDED



2.2 – 3.8 V/ 3300 F Cell
ESR of 1.0 mΩ
Peak pulsed current of ~1500 A
Peak cont current of 360 A
E_{MAX} = 4.42 Whr



2.2 – 3.8 V/ 3000 F Cell
ESR of 1.0 mΩ
Peak cont current of 150 A
E_{MAX} = 4.5 Whr



48 V/165 F Module
ESR of 6.3 mΩ
Peak current of 1.9 kA
E_{MAX} = 53 Whr



48V/165F Ioxus X-Series module
ESR of 3.5mΩ
Peak current of 2.6kA
E_{MAX} = 59.0Whr



96V/83F Ioxus X-Series Liquid cooled module
ESR of 6.1mΩ
Peak current of 2.7kA
E_{MAX} = 114.8Whr



51V/178F Skeleton Module
ESR of 2.6mΩ
Peak current of 2.921 kA
E_{MAX} = 64.0 Whr
FCT FUNDED



170V/53F Skeleton Liquid Cooled Module
ESR of 8.4mΩ
Peak current of 2.936 kA
E_{MAX} = 214.0Whr
FCT FUNDED



26.4 – 45.6 V/ 275 F LIC Module
ESR of ~11 mΩ
Peak Current of 1.1 kA
E_{MAX} = 54.6 Whr

Figure 11: Picture of the UC modules used in this experiment along with some of their key characteristics.

Table 2: Ultracapacitor (UC) cells and their electrical properties given by their datasheets.

Best	Average	Worst	Skeleton	Maxwell	Ioxus	JM Energy	General Capacitor
			SCA3200	BCAP3400	iRB3000K270CT	Ultimo 3300F Prismatic	LCA3000G
		V	2.85	2.85	2.85	2.2 - 3.8	2.2 - 3.8
		F	3200	3400	3150	3300	3000
		mΩ	0.12	0.22	0.17	1.00	1.7
		kA	3.3	2.0	2.7	1.1	Not listed on datasheet
		kA	24.0	10.0	15.5	Not listed on datasheet	Not listed on datasheet
		Wh	3.61	3.84	3.18	4.42	4.5
		Wh/kg	6.82	7.40	6.30	13	18
		Wh/L	9.30	9.60	7.80	20	30
		kW	16.90	9.36	11.73	3.61	1.86
		kW/kg	32	18	23	11	7.5
		kW/L	43.33	23.40	21.00	16.32	14
		kg	0.53	0.52	0.51	0.35	.25
		mm	60.0	60.4	60.2	150.2	241
		mm	138.0	138.0	144.0	93.2	126
		mm	N/A	N/A	N/A	15.8	5
		L	0.39	0.40	0.41	0.22	0.15
		cycles	1000000	1000000	1000000	600000	200,000

Table 3: Ultracapacitor (UC) modules and their electrical properties given by their datasheets.

Best	Average	Worst	Skeleton		Maxwell	Ioxus		JM Energy
Model Number			SMOD48V178F	SMOD170V53F	BMOD0165 P048 C01	iMOD096V083A23-LQ	iMOD048V166A 23	Ultimo 3300F Prismatic
Cooled		NO	YES		NO	YES	NO	NO
Rated Voltage	V	48.6	170.0		48.0	83.0	48.6	26.4 - 45.6
Rated Capacitance	F	178.0	53.0		165.0	97.2	175	275
DC ESR	mΩ	3.1	10.2		6.0	6.1	5.4	10.5
Max. Peak Current for 1 s	kA	2.80	2.94		1.90	2.70	2.7	1.1
Short Circuit Current	kA	18.90	16.70		8.10	15.8	15.8	Not listed on datasheet
Energy	Wh	58.3	214.0		53.0	109.4	57.4	53.0
Specific Energy#	Wh/kg	4.10	3.82		3.73	3.13	3.19	8.62
Energy Density	Wh/L	4.40	4.13		3.65	3.67	3.68	9.53
Power (matched impedance)	kW	193.0	708.3		96.0	282.3	109.4	49.5
Specific Power (matched impedance)	kW/kg	13.50	12.65		6.76	8.07	6.08	8.05
Power Density (matched impedance)	kW/L	14.50	13.66		6.61	9.47	7.01	8.90
Total Mass	kg	14.3	56.0		14.2	35.0	18.0	6.15
Length	mm	418.0	768.0		418.0	906.0	474.0	260.4
Width	mm	194.0	430.0		194.0	147.0	147.0	168.3
Height	mm	157.0	157.0		179.00	224.0	224.0	127.0
Volume	L	13.30	51.80		14.52	29.80	15.6	5.56

Characterization Methods

Electrochemical Impedance Spectroscopy (EIS)

At the cell level only, the study performed here has consisted of three separate experiments as listed above. The first test involves characterizing each cell's impedance using electrochemical impedance spectroscopy (EIS). EIS is a perturbative characterization, allowing the real and imaginary components of a UC's impedance to be measured as a function of frequency. EIS can be performed using two different methods, namely galvanostatic or potentiostatic. Galvanostatic mode perturbs the cell with a precise AC current and sweeps through a pre-defined frequency range. At each frequency step, the perturbation voltage and current are measured to determine the cells real and imaginary impedance values. It is the same idea for potentiostatic mode but instead of perturbing the cell with a set current, the cell is perturbed at a set voltage. In these experiments, an Autolab PGSTAT302N is used along with a 20 A booster, seen in Figure 12. Multiple cells from each manufacturer are characterized, as they are received, using EIS in the potentiostatic mode at 5 mV from 1 kHz to 10 mHz. The cells impedance is measured across their respectable

usable voltage range from 100% to 10%, in 10% increments. Along with performing EIS, the potentiostat is used to conduct a 15 A baseline that can be used to confirm each cell's initial DC ESR, as well as measure each cell's initial capacitance. The baseline is performed by first charging each cell to its rated voltage and then discharging the cell to 10 mV. Once a cell has been initially characterized using the potentiostat, it can undergo any of the other two tests, including single transient discharge into near match impedance loads or repetitive pulsing.



Key features	
Electrode connections	2, 3 and 4
Potential range	+/- 10 V
Compliance voltage	+/- 30 V
Maximum current	+/- 2 A (20 A with BOOSTER20A)
Current ranges	1 A to 10 nA (100 pA with ECD module)
Potential accuracy	+/- 0.2 %
Potential resolution	0.3 μ V
Current accuracy	+/- 0.2 %
Current resolution	0.0003 % (of current range)
Input impedance	> 1 T Ω m
Potentiostat bandwidth	1 MHz
Computer interface	USB
Control software	NOVA

Figure 12: The Autolab PGSTAT302N used in this experiment, along with some of its key features.

Single Transient Discharge

Cells that have been characterized from each manufacturer next undergo single transient discharges into a near matched impedance load. This is accomplished using a custom experimental testbed, seen in Figure 13, designed and constructed at UTA as part of an ONR YIP grant in 2011 [18]. The testbed was designed to handle 10 kA peak current transient discharges from electrochemical energy storage devices. It is able to achieve load impedances as low as $\sim 350 \mu\Omega$. The testbed was recommissioned for use in these experiments to study each cell's peak power density by discharging the device under test for 200 ms into the low impedance load. In this round of experimentation, at least one of each type of cell procured was experimentally discharged using

the test stand three times. Between each discharge, the cell under test is removed from the stand, recharged, and then replaced in the stand and tested again. This provides a degree of statistical variation into the tests to ensure that the results are statistically relevant. It should be noted that the modules studied were not evaluated in this manner.

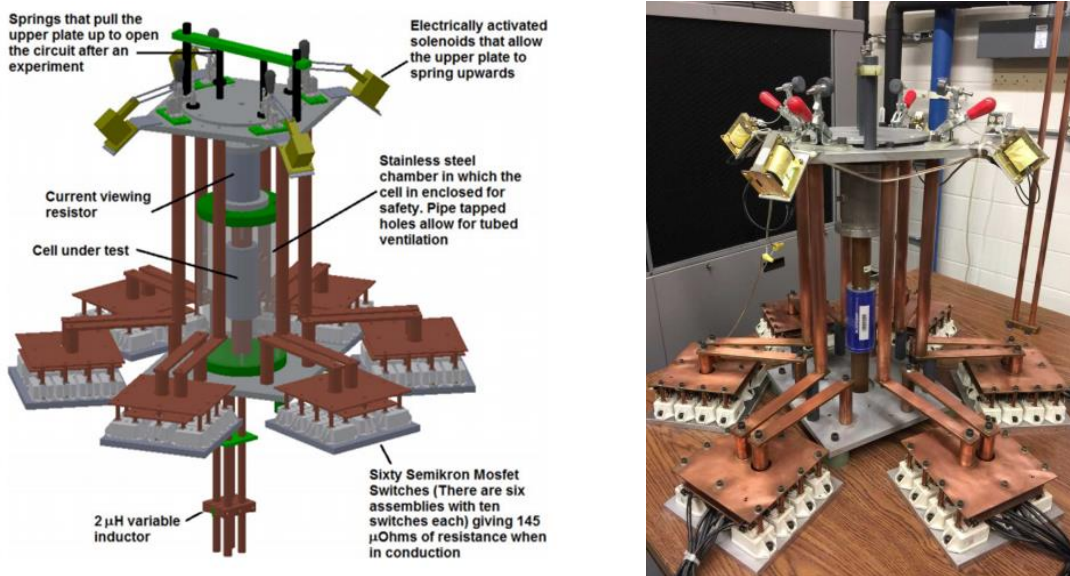


Figure 13: CAD drawing of the custom experimental testbed (left) along with a photograph of the testbed containing a Maxwell 3000 F cell (right).

Repetitive Transient Cycling

In the next series of experiments, each cell undergoes a series of repetitive transient cycling to evaluate their electrical and thermal characteristics. Repetitive pulsing is performed at as many as four different rates, 100 A, 200 A, 250 A, and 300 A until thermal equilibrium is reached, depending on the maximum recommended current by the manufacturer. At the 100 A, 200 A, and 250 A rates, respectively each cell is cycled at 100% duty cycle, with 50% consisting of a charge and 50% consisting of a discharge. This means that there is ideally a 0 J net energy change in the capacitor after each charge/discharge cycle. Each cycle operates the capacitor between roughly 90% and 70% of its rated voltage. In the 300 A repetitive experiments, the cells were cycled in the

same manner but the operational voltage window was expanded to between 100% and 50% due to the higher voltage drop induced at this higher current. Because the impedance of the JM Energy and General Capacitor LICs are significantly higher than the other cells, the operational window was opened up to between 90% and 40 % for the 100 A, 200 A, and 250 A rates. In the 300 A experiments, the two LICs were cycled between 90% and 10% of their rated voltage. Each test is conducted with the cell placed within a temperature chamber that is held at 20°C. Each cell is instrumented with a T-type thermocouple placed at the center of the cell to monitor its body temperature during testing. The repetitive transient cycling is performed using a Chroma model 63209 programmable load, with the capability of sinking current as high as 1000 A and two Sorensen power supplies, each capable of sourcing up to 188 A. The load and supplies are controlled remotely using SCPI communication via GPIB and LXI, respectively. A custom virtual instrument (VI) was created using LabVIEW to control the supplies and loads, monitor the system for thermal or voltage cutoffs, and record the resulting voltage, current, and thermal data.



Figure 14: Photographs of the programmable load and supplies used to cycle the cells and modules for this experiment.

A similar series of repetitive transient cycling experiments were performed on each of the higher voltage modules procured as well. The procedure at the module level is performed in exactly the same way as it is at the cell level. This means that the same current values are studied across

proportional voltage ranges. When studying the modules, additional thermocouples are added as needed and as possible to ensure that the module is well characterized. As will be discussed in the module specific results later, some of the modules procured are internally potted with thermal compound for higher thermal conductivity to the containment. This unfortunately prevented some of the modules from being able to be internally instrumented. As shown in Table 2, four of the modules evaluated are roughly 48 V, one is 96 V, and the other is 170 V. The 96 V and 170 V modules are liquid cooled and they were studied both with and without liquid cooling. All of the ~48 V modules were cycled using the same Chroma 63209 loads and Sorensen power supplies used in the cell level while the 96 V and 170 V modules were cycled using a Chroma 17030 500 kW cyler, capable of 36 - 1200 V and up to 700 A. For the cooled modules, a glycol coolant mixture was used that was held at 20°C by a PolyScience chiller at the flow rate given by each modules respective users' manual. Flow rates of 15 L/min were used in evaluation of the Ioxus 96 V module and 5 L/min was used in the evaluation of the Skeleton 170 V module.

Experimental Setups

Electrochemical Impedance Spectroscopy

Since every cell has a unique termination style, each one requires that a unique bus work scheme be fabricated to connect it to the potentiostat. The bus work must accommodate the working and common electrodes such that the cell can be charged/discharged and sense leads can be connected to monitor the cell under tests' voltage. Figure 15 contains a photograph of each of the cells with their respective bus work and sense leads attached.

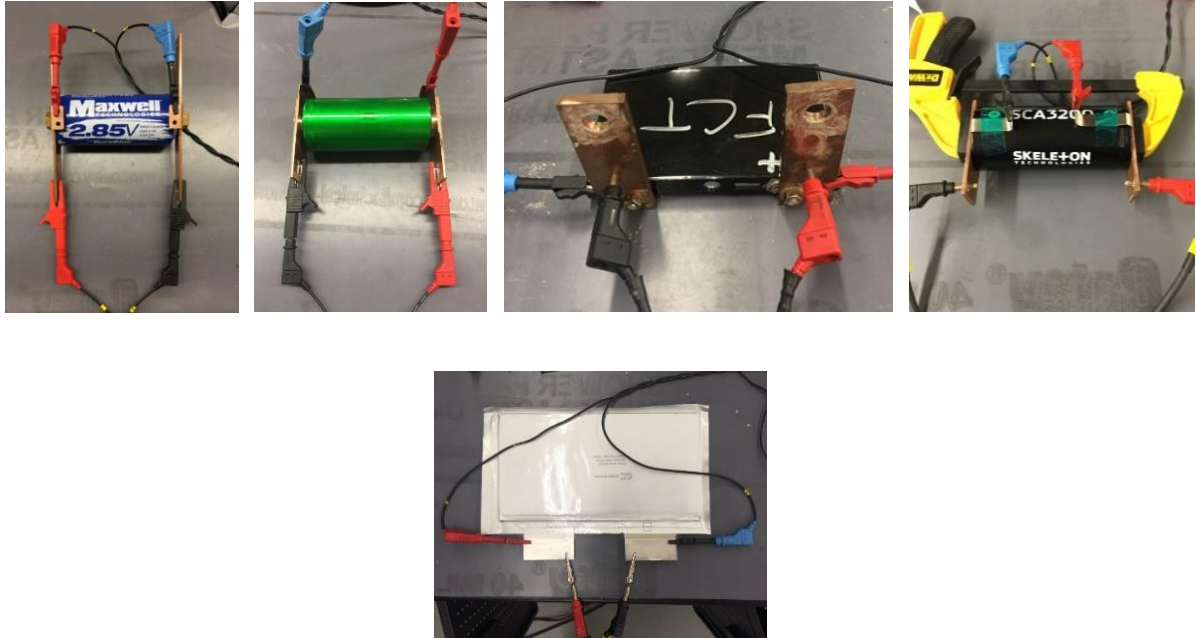


Figure 15: Photographs of the Maxwell (top left), Ioxus (top second left), JM Energy (top third left), Skeleton (top right), and General Capacitor (bottom) set up for initial characterization from the PGSTAT302N.

Single Transient Discharge

Once a cell has completed an initial characterization using EIS, it is then able proceed to the single transient discharge testing stage. As described earlier, a unique low impedance testbed that is capable of discharging cells at transient currents as high as 10 kA was used. The load is shown photographically below in Figure 16. In short, the stand works by discharging the cell under test into a series of sixty high power MOSFETs that are all connected in parallel. Each MOSFET has an on-state impedance of roughly 8 m Ω equating to an equivalent resistance of roughly 135 $\mu\Omega$. The series connection of the MOSFETS with the other bus work that makes up the stand creates a load impedance that varies between 350 $\mu\Omega$ and 500 $\mu\Omega$. This is on the order of the impedance of most UCs meaning that near matched load impedances can be evaluated. Though the stand can be tuned using externally variable bus work, no tuning occurred in the experiments performed here. Instead the stands lowest achievable impedance was utilized.

The cell under test is placed firmly between the top and bottom plates of the testbed using a series of 3/4 inch copper rods. All electrical interfaces are coated in a conductive lubricant to minimize contact resistance. The three cylindrical cells were all able to use relatively the same setup due to their similar size and shape. The JM Energy LIC is a prismatic cell that required unique bus work to adapt it into the stand and the General Capacitor LIC is a pouch cell that was even more difficult to adapt.

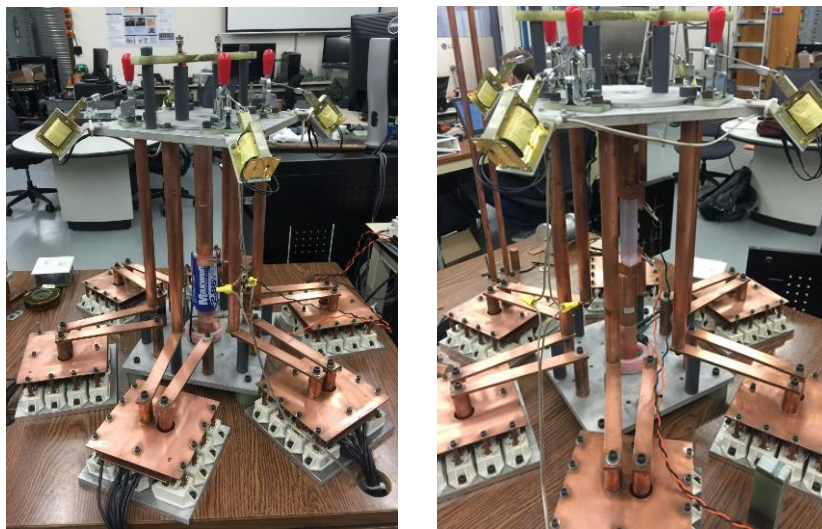


Figure 16: The single transient discharge experimental testbed with a cylindrical Maxwell (left) and prismatic JM Energy (right) cell firmly placed between the top and bottom plates.

When pulsing the cell under test, its voltage is measured using a differential voltage monitor and its discharge current is measured using a CWT rogowski coil, both of which can be seen in the images above. Along with being responsible for controlling the MOSFETs switching frequency, LabVIEW is used to record the voltage and current through the use of a PXI chassis data acquisition system. As already described, each cell was transiently discharged for 200 ms into the lowest impedance possible. By taking the initial change in voltage as it transitions from an open circuit potential to a conduction potential, and dividing that change by the current measured, the

internal impedance of the cell can be characterized under high current, transient DC conditions. That value is then able to be compared with that presented by the manufacturer in their datasheet.

Repetitive Transient Cycling

As previously stated, Chroma 63209 programmable loads and Sorensen power supplies are used to load and recharge the cells and 48 V modules when they are subject to repetitive transient cycling. The programmable load and supplies are connected to a central bus using 3/0 copper welding cable. Another set of cables extend from the central bus and into the temperature chamber where they are connected to the cell for repetitive transient testing. Conductive lubricant is applied to the each cells' terminals and on the cable terminations to minimize contact impedance. A thermocouple is placed on the body of each cell and another is set freely in the temperature chamber for ambient temperature measurement. The only thing that differs between each respective test is the bus work that is necessary to connect the cell to the cabling. Photographs of each cell set up for repetitive transient testing can be seen in Figure 17.

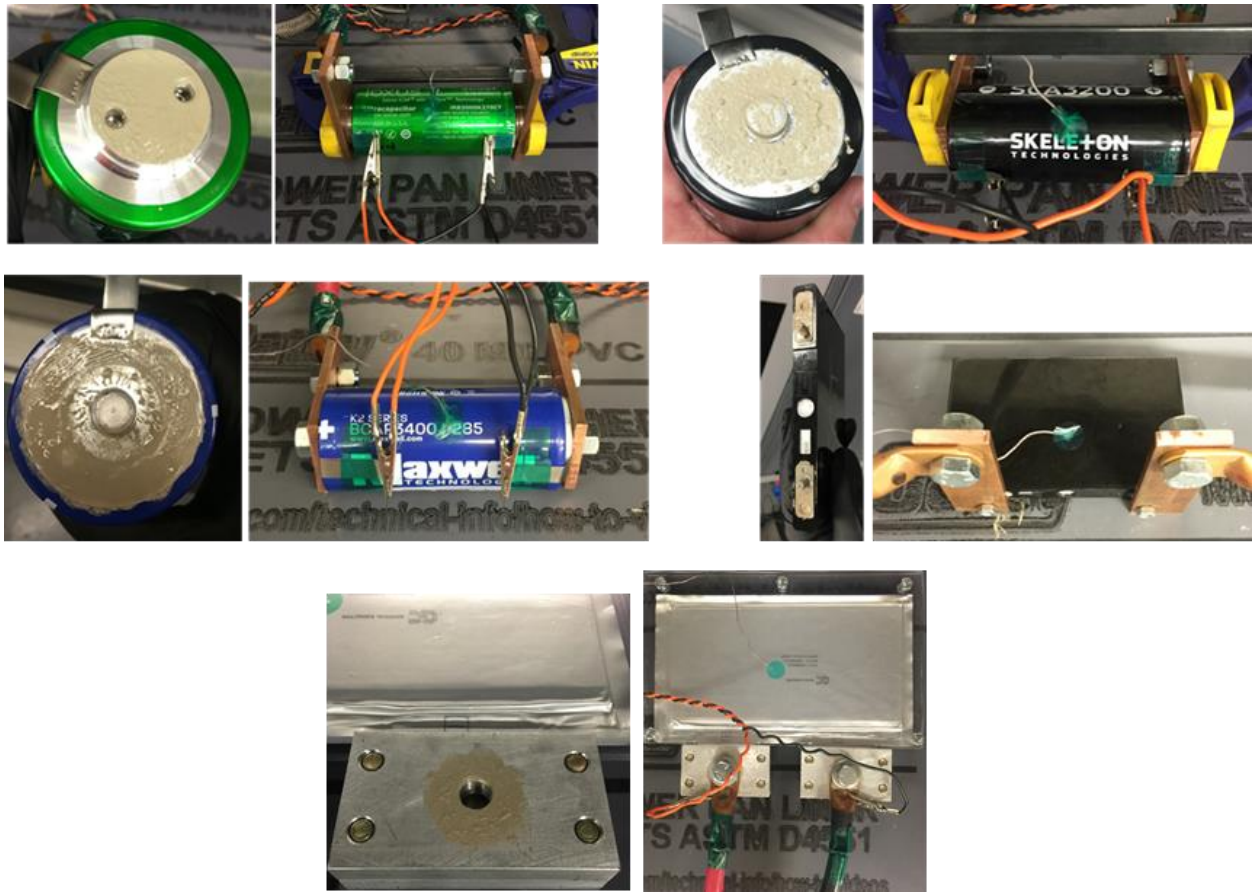


Figure 17: Sample photographs of the Ioxus (upper left), Skeleton (upper right), Maxwell (middle left), JM Energy (middle right), and General Capacitor (bottom) cells prior to evaluation showing both the terminals and their connection to bus work.

The Maxwell 48 V, Ioxus 48 V, Skeleton 51 V, and JM Energy 45 V modules are all air cooled modules that are similar in shape and form factor. Each was evaluated under the same repetitive test profiles as their cell counterparts were while placed inside of the temperature chamber set to 20°C. The only major difference in the test setup of these modules was the thermal instrumentation. When the bottom of the module was opened, the Maxwell cell has air between the cells and therefore thermocouples were able to be strategically placed on cell bodies throughout the module, as shown in Figure 18. Thermocouples were able to be placed on the cells labeled, where A is the cell connected to the modules negative terminal and F is the cell connected to the positive terminal. Thermocouples were placed on several other cells including the center cell C and the central bus

bar D. The remaining thermocouples, B's and E's, are all placed on the body of the respective cells. Though the Maxwell module has an internally placed thermistor, it was not measured due to the ability to place so many thermocouples internal to the module.

The Ioxus module on the other hand, uses thermal potting compound between the cells to improve its thermal heat transfer to the case. As a result, when it was opened, only a few thermocouples were able to be strategically placed on cells near the end of the module, as shown in Figure 19. Due to the inability to place thermocouples throughout the Ioxus module, the internal thermistor installed by Ioxus was used measure the internal temperature of the module. The thermistor is a NTC type with a base resistance of 10 k Ω at 25°C. A monitoring circuit was assembled that places a 2.7 k Ω resistor in series with the thermistor, creating a resistive divider. Using a 10 V applied voltage, the voltage drop across the thermistor is measured and calibrated to the module's temperature. The thermistor was calibrated by placing the module in the temperature chamber and allowing it to soak at temperatures ranging from 20°C to 70°C, in 5 degree increments. Once the module was soaked at each temperature so long as for thermal equilibrium to be reached, the voltage drop across the thermistor was recorded. The corresponding voltage measured at each temperature was used to form a mathematical relationship between the module's temperature and the thermistor voltage, shown in Figure 19.



Figure 18: Maxwell 48 V module with the thermocouple placement (left) and the module inside the temperature chamber set up for testing.

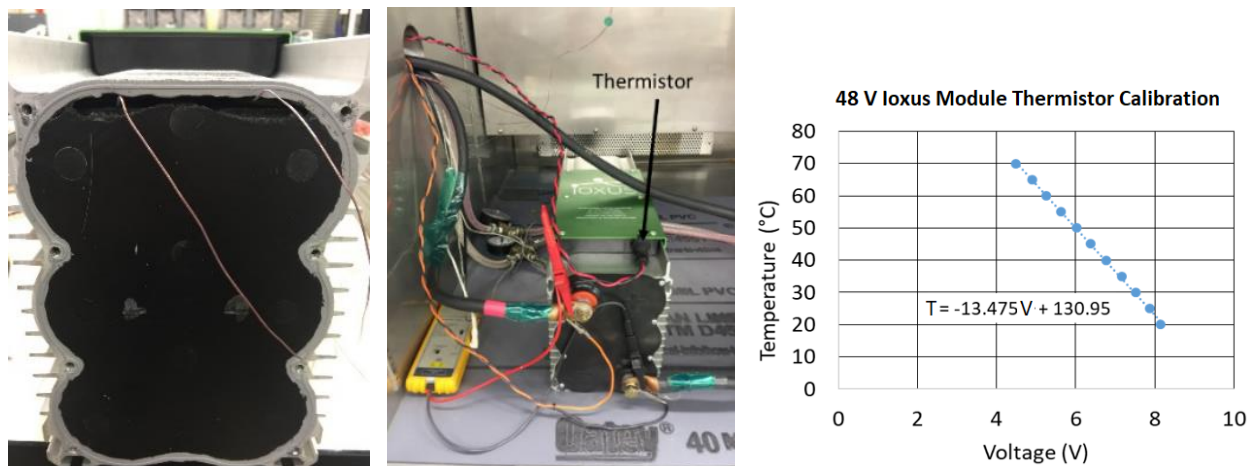


Figure 19: Ioxus 48 V module opened up (left) fully instrumented inside the temperature chamber (middle), and the calibration data collected and calculated equation used to relate the module's internal thermistor voltage to its respective temperature (right).

The JM Energy module was disassembled, as shown in Figure 20, and individual cells were instrumented for thorough thermal measurement. As shown, there is no significant method used by JM Energy to extract heat from the module and, as will be shown later, this prevented it from being able to provide significant current for long periods of time. Thermocouples were also placed on the positive and negative terminals of the module and on the bus work, which is relatively thin.



Figure 20: JM Energy 45 V module fully disassembled (left) to place thermocouples of the body of multiple cells (center). The module with multiple cells instrumented and reassembled (right).

Similar to the 48 V Ioxus module, the Skeleton 48 V module is internally potted with thermal compound preventing it from being heavily instrumented with thermocouples. The thermal data gathered relied solely on the data provided by the module's four internal thermistors. Though the Ioxus and Maxwell modules each only have one thermistor internal to them, the Skeleton has four and utilizes CAN communication to relay the data out of the module. The management system includes active resistive cell balancing, temperature sensing, and voltage monitoring and reporting at the cell and module levels, respectively. Despite having four thermistors, the CAN module utilizes internal logic to report only the highest temperature recorded amongst them. Table 3 summarizes the data, data type, and a description of the information that is sent over the CAN bus, all of which is necessary when setting up the communication protocol. Each module comes with a

unique 29-bit CAN bus identifier to establish communication. CAN communication and data recording was achieved using one of National Instruments' (NI's) CAN data acquisition cards that is comprised of NI-XNET and USB-8502. The USB-8502 allows for a physical means of CAN communication between the module and the host computer. NI-XNET is the software in which the data given in Table 4 is used to properly configure the module under test. Once communication has been setup, its voltage and temperature data is reported over the CAN bus at a rate of 2 Hz. A photograph of the Skeleton 48 V module is shown in Figure 21. The digital nature of the CAN measurements along with the slower sample rate are slight downfalls but provide the information needed to thermally characterize the module.

Table 4: 48 V Skeleton Module CAN bus protocol.

	Byte 0	Byte 1	Byte 2	Byte 3	Byte 4	Byte 5	Byte 6
Data	Fault Flags	Warning Flags	Module or System Voltage		Highest Temperature	Highest Cell Voltage	Average Cell Voltage
Data Type	Bit-wise Boolean	Bit-wise Boolean	Unsigned 16 bit		Unsigned 8 bit	Unsigned 8 bit	Unsigned 8 bit
Description	See Table 3		0.1 V precision		1 °C precision Offset at -45 °C	0.01V precision Offset at 0.5 V	0.01V precision Offset at 0.5 V

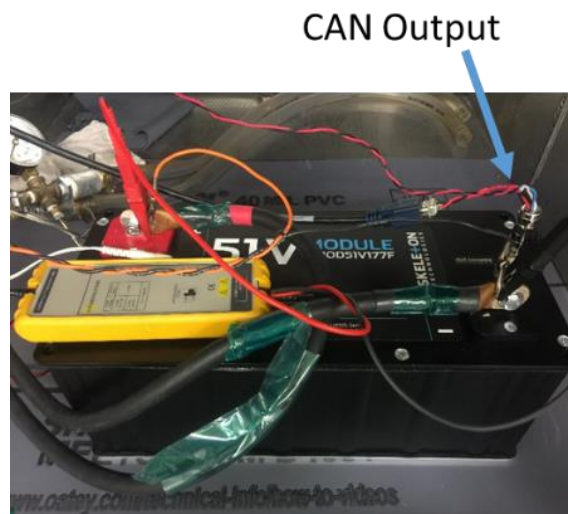


Figure 21: Skelton 48 V module (technically it has a datasheet rating of 51 V).

The 96 V Ioxus module is assembled very similarly to the 48 V Ioxus module is. It is potted with thermal compound, which prevented further thermocouple instrumentation. It is manufactured with a single loop liquid cold plate placed between the arrays of cells. As was the case with the 48 V module, an NTC thermistor is manufactured internal to the module and it was utilized for all thermal monitoring. The thermistor was calibrated identically as the one within the 48 V Ioxus module was, discussed earlier. A photograph of the module assembled in the test chamber is shown in Figure 22. The module was evaluated with and without liquid cooling flowing through the cold plate. Evaluation of the 96 V occurred in two different ways. In the first, the module was assembled in the environmental chamber and it was cycled using the 80 V Chroma 63209 programmable loads and the 80 V Sorensen power supplies. Because that set of loads and supplies are not able to cycle the module up to its full 96 V rated voltage, the operational voltage window was widened such that the energy removed during each charge/discharge is equivalent to what should be removed at full voltage. Since the module is cycled at constant current, the I^2R losses should be the same, resulting in roughly the same temperature rise as when it is operated across its full voltage range. That data will not be presented here as the data collected is nearly identical to that obtained using the second method in which the modules were able to be cycled across their full voltage range using the Chroma 17030 cycler. The only difference between the two series of experiments was that the module was not cycled in a thermal chamber due to it being located in a different room. The module was instead placed out in an ambient environment that does fluctuate slightly.

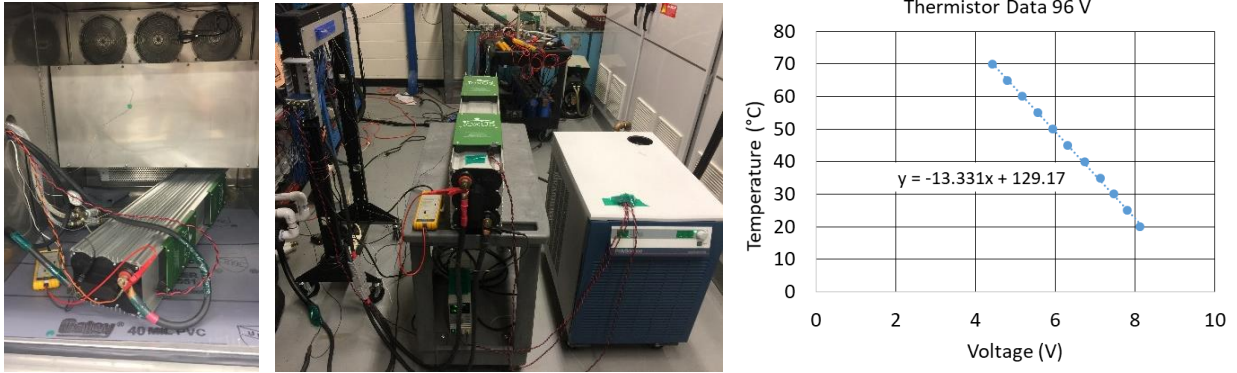


Figure 22: Ioxus 96 V module instrumented inside the temperature chamber (left), in an ambient environment (middle), and the calibration data collected and calculated equation used to relate the module’s internal thermistor voltage to its respective temperature (right).

The last module studied was the 170 V Skeleton module. Like its 48 V counterpart, the module is configured with CAN communication over which it reports its peak temperature and module voltage. The module is liquid cooled however, due to its rugged casing and larger size, it is unclear how many passes it has or how it’s configured internally. Due to its larger size and its high voltage, this module was only cycled in an ambient environment, with and without the use of liquid cooling, using the Chroma 17030. A photograph showing it setup for testing is shown in Figure 23.



Figure 23: Skeleton 170 V module sitting in an ambient environment, being cycled.

Ultracapacitor Characterization Results

Measurement of Impedance using Electrochemical Impedance Spectroscopy (EIS) and Initial Usable Capacitance

As discussed earlier, the impedance and usable capacity of each cell studied was characterized using a potentiostat. The usable capacity of each cell was measured by first charging it up using a 15 A constant current and then discharging it using a similar constant current discharge procedure. The measured usable charge, measured in Coulombs, as a function of time from each cell is shown in the leftmost plot of Figure 24 while a plot of the conduction voltage of each cell as a function of time is plotted in the rightmost figure. Note that the LICs cannot be discharged below 2.2 V and is the reason why they are not discharged to 0.01 V as the EDLCs are.

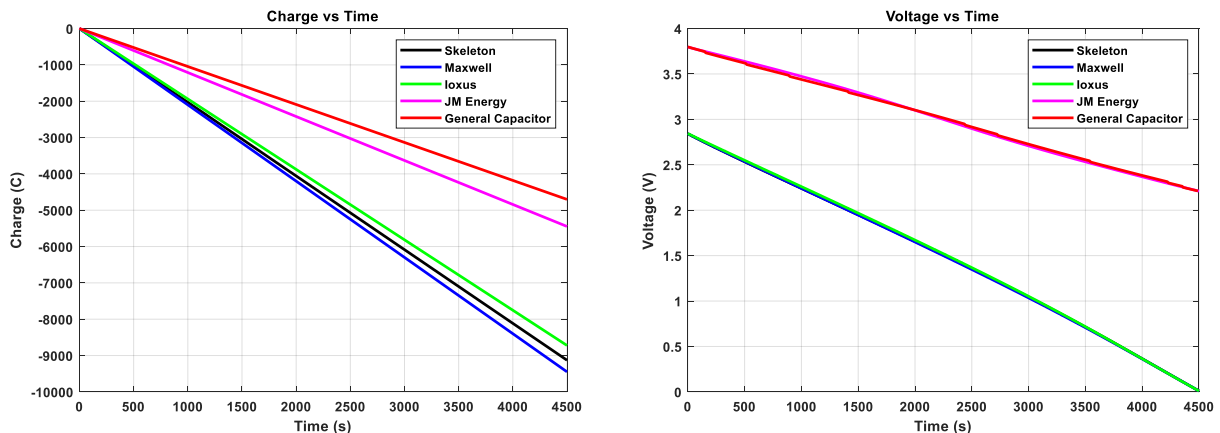


Figure 24: Each of the UCs charge curves vs time (left) and their associated voltage curves (right).

The voltage curves of each of the three respective EDLCs are nearly identical, as expected, due to their similar characteristics. The charge curves are used to determine each cell's initial capacitance. The initial stored electric charge of the Skeleton cell was 9129 C, which equates to a capacitance of roughly 3203 F. This aligns well with the cell's rated capacitance of 3200 F, given by the datasheet. The initial usable electric charge of the Maxwell cell was 9357 C, which translates

to a capacitance of 3283 F that is slightly less than the cells rated capacitance of 3400 F. The initial usable electric charge of the Ioxus cell was 8723 C, which translates to a capacitance of 3060 F, just slightly under the rated value of 3150 F. The JM Energy LIC's initial usable electric charge was 5447 C, translating to a capacitance of 3404 F, which is just slightly above the rated capacitance of 3300 F. The final cell is the General Capacitor LIC, which had an initial usable electric charge of 4741 C. This translates to a capacitance of 2963.3 F, slightly lower than the cells rated capacitance of 3000 F.

The impedance measured from each respective EIS scan is shown in Figure 25. As discussed earlier, the EIS profiles are used to speculate on how a cells' impedance changes as a function of its charge voltage. Analysis of the Skeleton cell's EIS profile approximates that the DC ESR ranges from 90 $\mu\Omega$ to 105 $\mu\Omega$, which is slightly lower than the datasheet typical/max of 110 $\mu\Omega$ /130 $\mu\Omega$. That of the Ioxus cell estimates that its DC ESR ranges from roughly 172 $\mu\Omega$ to 185 $\mu\Omega$, lying between the typical/max values of 170 $\mu\Omega$ /260 $\mu\Omega$ given by the datasheet. The Maxwell cell's EIS profile approximates that the DC ESR ranges from 160 $\mu\Omega$ to 180 $\mu\Omega$, which is slightly lower than the typical/max of 220 $\mu\Omega$ /280 $\mu\Omega$ given by the datasheet. As expected, the DC ESR of the Maxwell and Ioxus cells, respectively, are nearly the same while that of the Skeleton cell is significantly lower. The EIS measurement made from the JM Energy cell approximates that its DC ESR ranges from 880 $\mu\Omega$ to 950 $\mu\Omega$, which is slightly lower than the datasheet value of 1 m Ω . The General Capacitor EIS profile estimates that the cells DC ESR ranges from 1.36 m Ω to 1.39 m Ω , within the datasheet range of ≤ 2 m Ω . The EIS profile for the General Capacitor cells did not intersect zero using the frequency range of 1 kHz to 10 mHz. In order to determine the cells DC ESR the frequency range was increased to 10 kHz to 10 mHz. It is important to note that the hybrid

nature of the two respective LICs makes their ESR significantly higher than that of the UCs and that it is not fair to really compare the ESR of LICs to those of EDLCs.

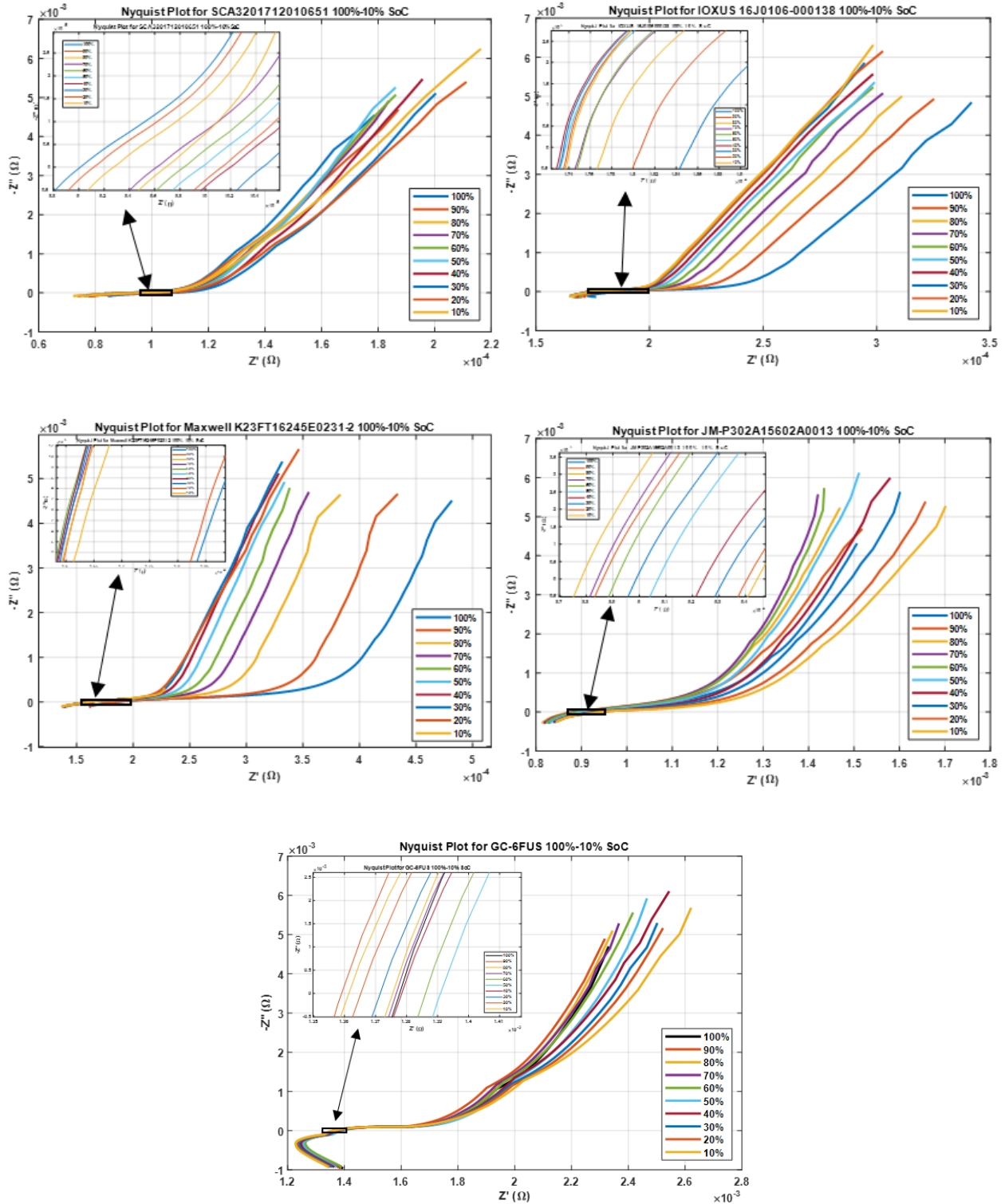


Figure 25: Electrochemical impedance spectroscopy (EIS) measurements made from each respective type of cell studied including the SCA3200 (upper left), Ioxus iRB3000K270CT (upper right), Maxwell BCAP3400 (middle left), JM Energy Ultimo 3300F prismatic (middle right), and the General Capacitor 3000F (bottom), as a function of their charge voltage in 10% increments.

In conclusion to this portion of the test procedure, the capacity and impedance results measured from each respective cell evaluated aligns well with the values specified by each manufacturer. The results confirm the claims of Skelton that the impedance of their cells, as a result of their rolled graphene electrodes, is significantly less than that offered by US UC manufacturers.

Single Transient Discharge Results

The next series of results presented are those collected when each type of cell was discharged for 200 ms into a low impedance load using UTA’s custom discharge stand. This experiment was aimed at further characterizing each cells’ DC impedance when conducting high current as well as measuring their power density into near matched loads. Figure 26 presents the conduction voltages (left) and the conduction currents (right) measured from each respective cell. The impedance is measured by subtracting a cells’ conduction voltage from the open circuit potential it is at prior to conduction. Dividing the voltage drop measured by the conduction current results in an accurate estimate of the cell’s internal DC resistance. A higher conduction voltage and higher transient current equates to a cell with a lower internal resistance.

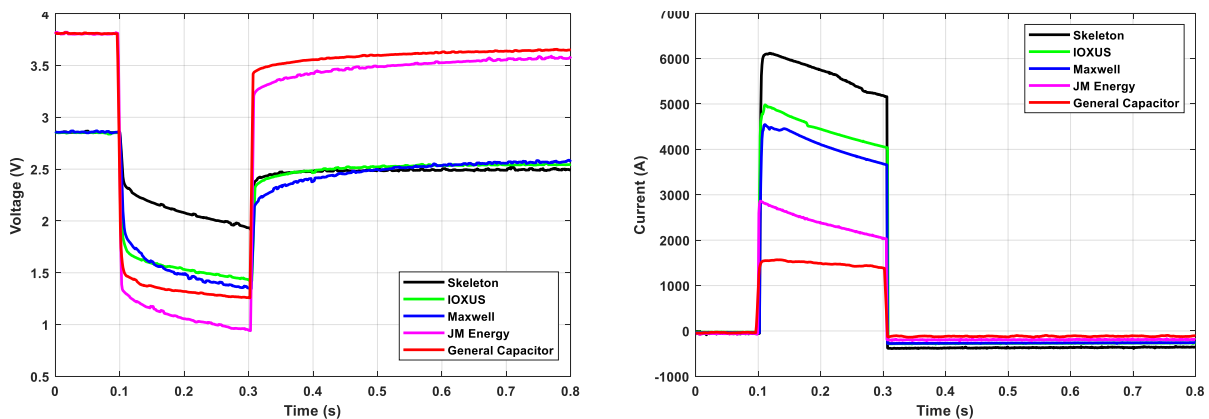


Figure 26: Single transient discharge voltage profiles for each of the cells (left) and their corresponding current profiles (right).

The Skeleton cell was discharged into a $373 \mu\Omega$ load impedance supplying a peak current of 6.11 kA, as shown in Figure 26. The cell's impedance is calculated to be $93.8 \mu\Omega$, aligning well with what the manufacturer indicates on their datasheet. The cell supplied a peak power of 14.16 kW, resulting in a specific power density of 26.72 kW/kg, just slightly lower than the 28 kW/kg the datasheet lists. Note that in this case, the impedance of the cell is significantly less than that of the stand so maximum power transfer is not achieved, attributing to the slight variation from the datasheet. The Ioxus cell was discharged into a load impedance of $343 \mu\Omega$ conducting a peak current of 4.98 kA. Using the same method, the cell's impedance is calculated to be $229 \mu\Omega$, which aligns well with the datasheet's min/max values of $176 \mu\Omega / 260 \mu\Omega$. The Ioxus cell supplied a peak power of 8.58 kW, resulting in a specific power of 16.5 kW/kg, which is slightly lower than the value given by the datasheet. The impedance is again slightly lower than that of the stand. The Maxwell cell was discharged into a load impedance of $403 \mu\Omega$, producing a peak current of 4.56 kA. The cell's impedance is calculated to be approximately $225 \mu\Omega$, which aligns well with the datasheet min/max of $220 \mu\Omega / 280 \mu\Omega$. The Maxwell cell supplied a peak power of 8.41 kW, resulting in a specific power of 16.17 kW/kg, this aligns well with the datasheet. The JM Energy cell was discharged into a $467 \mu\Omega$ load impedance, much lower than that of the cell, producing a peak current of 2.86 kA. The cell's impedance is calculated to be $862 \mu\Omega$, which aligns with the JM Energy cell's EIS profile and the datasheet value. The cell supplied a peak power of 3.92 kW, resulting in a specific power of 11.2 kW/kg, aligning well with the value given in the datasheet. The General Capacitor cell was discharged into an $894 \mu\Omega$ load impedance, much lower than that of the cell, producing a peak current of 1.57 kA. The cell's impedance is calculated to be $1.5 \text{ m}\Omega$, which aligns closely with the General Capacitor cell's EIS profile and the datasheet value. The cell

supplied a peak power of 2.44 kW, resulting in a specific power of 9.74 kW/kg, aligning well with the value given in the datasheet. Figure 27 shows a Ragone chart that summarizes each respective cells DC impedance and the power it supplied to the low impedance load. Table 5 summarizes the impedance, conduction current, conduction voltage, power supplied, specific power density, and volumetric power density.

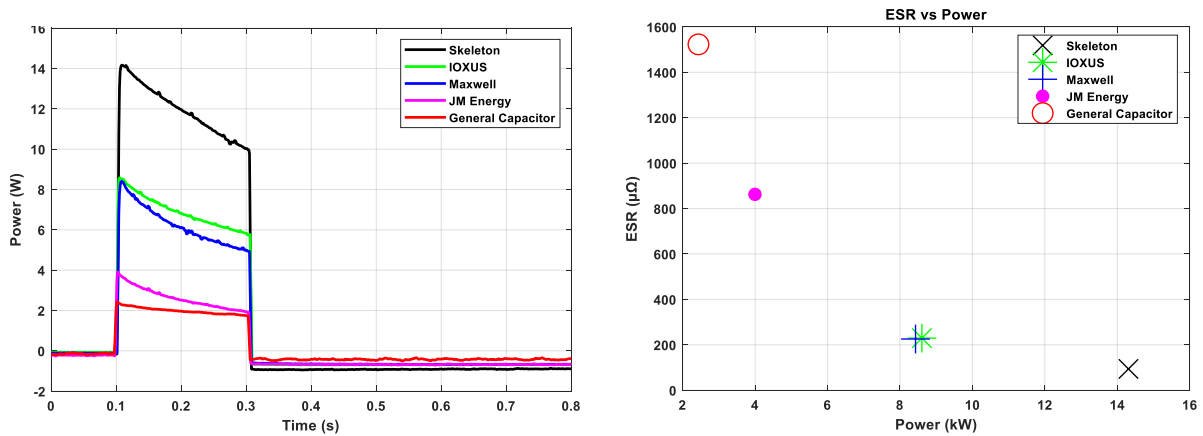


Figure 27: Plot of the power supplied by each cell (left) and each cell’s ESR vs the power supplied (right).

Table 5: Summary of the impedance, current, voltage, power, and power density values, respectively, measured during the single transient discharge experiments.

Property	Unit	Skeleton	Maxwell	Ioxus	JM Energy	General Capacitor
		SCA3200	BCAP3400	iRB3000K270CT	3300F Pris.	3000F Pris.
Load Impedance	mΩ	0.373	0.403	0.343	0.467	0.894
Peak Current Sourced	kA	6.11	4.56	4.98	2.86	1.57
Conduction Voltage	V	2.28	1.83	1.71	1.34	1.41
ESR	mΩ	0.094	0.225	0.229	0.862	1.5
Power	kW	14.16	8.41	8.58	3.92	2.44
Specific Power (matched impedance)	kW/kg	26.72	16.17	16.5	11.20	9.74
Power Density	kW/L	36.31	21.02	20.92	17.82	16.26

The results obtained from the single transient discharge experiments further confirm the results obtained from the EIS measurements. Those are that the Maxwell and Ioxus cells are very comparable while the Skeleton cell’s impedance and power density is significantly better than that of any of

the other cells studied, validating Skeleton’s claims. The impedance of the LICs, both the JM Energy and the General Capacitor, respectively, are significantly higher than any of the EDLCs, as expected.

Repetitive Transient Cycling Results

The following results presented are collected from each type of cell when subject to the repetitive transient testing, described in detail in the previous sections. These tests are conducted to determine how each type of cell will perform electrically and thermally when subject to a series of cycling profiles, with currents ranging from 100 A to 300 A. Figure 28 contains the electrical data gathered for each of the type of cell when subject to the repetitive test procedure at 200 A. The voltage profiles give insight to how each cell will perform when subject to a repetitively transient load.

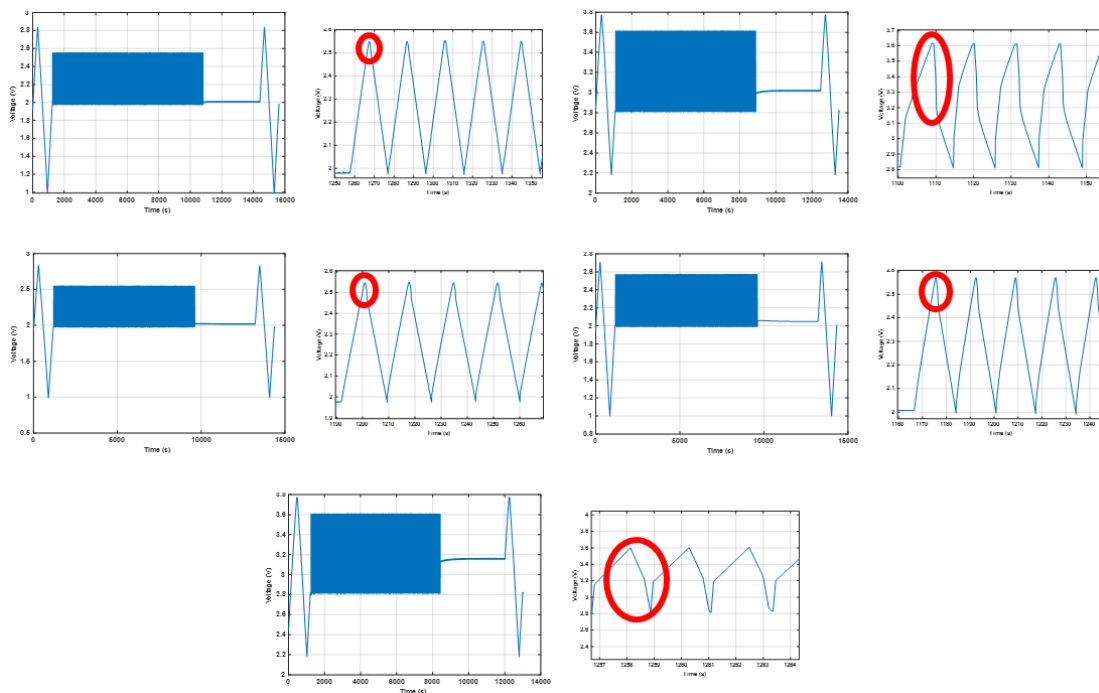


Figure 28: Voltage measurements made from each respective type of cell studied including the Ioxus iRB3000K270CT (upper left), JM Energy Ultimo 3300F prismatic (upper right), Maxwell BCAP3400 (middle left), Skeleton SCA3200 (middle right), and the General Capacitor 3000F (bottom), when subject to the repetitive transient procedure at 200 A.

A voltage drop can be seen during the transition from charge to discharge and vice versa in the voltage profiles in Figure 28. These voltage drops are circled in red and are caused by the transitional current and each respective cell's ESR. The higher the cell's ESR, the larger the voltage drop due to the charge transition. The Skeleton cell has been confirmed to have the lowest ESR by both the EIS and single transient procedures, resulting in the lowest voltage drop among the cells tested. The Maxwell and Ioxus cells have similar voltage drops due to their nearly identical ESR. The two UCs with the largest voltage drop are the JM Energy and the General Capacitor cells. Both cells are LICs, which as already mentioned have higher ESRs than the other UCs.

Figure 29 contains the thermal results corresponding to each respective cell, for the entire range of testing. The General Capacitor and JM Energy cells reached high temperatures during the experiment, experiencing much higher temperatures than the EDLCs. The General Capacitor cell reached a maximum temperature of 54°C when cycled at 200 A and was the only UC that was not able to complete the full range of tests. Similarly the maximum temperature of the JM Energy cell body reached 53°C when cycled at 300 A, which is at 20°C higher than the maximum temperatures of any of the EDLCs. The two LICs poor thermal performance is a direct result of ohmic heating caused by their high ESR. As expected, the Maxwell and Ioxus cells had very similar thermal performance during the repetitive cycling, with the two cell's maximum body temperatures reaching 33°C and 30°C respectively, when cycled at 300 A. The two UCs have shown to have nearly the same ESR through the previous tests performed. The Skeleton cell experienced the lowest raise in temperature during this test, reaching a maximum temperature of roughly 28°C. During the full range of evaluation of the Skeleton cell, its body temperature did not increase more

than 10°C over the ambient chamber temperature. The results validate the claims of Skeleton that their cells do perform better than the other competitive UCs.

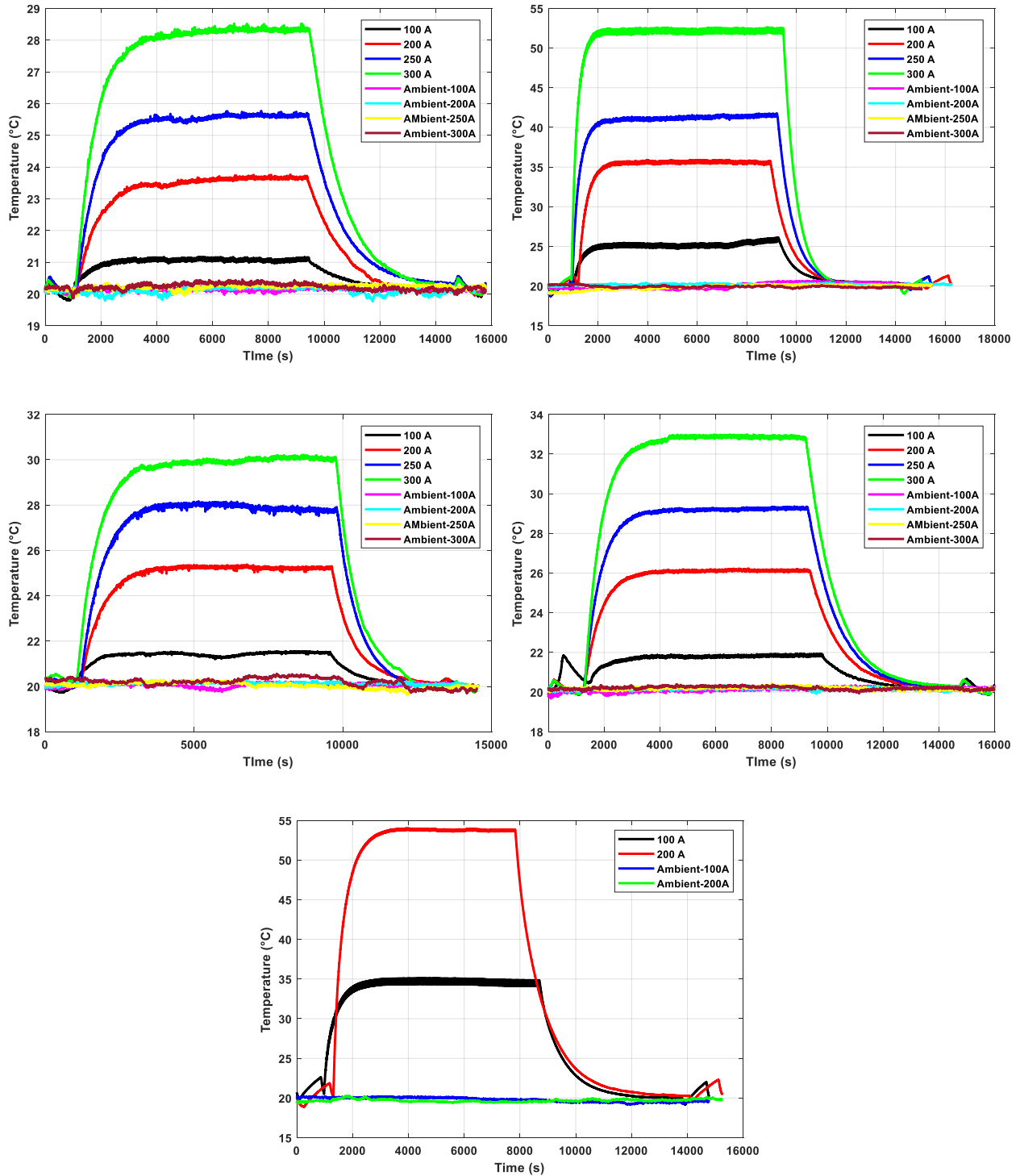


Figure 29: Thermal measurements made from each respective type of cell studied including the Skeleton SCA3200 (upper left), JM Energy Ultimo 3300F prismatic (upper right), Ioxus iRB3000K270CT (middle left), Maxwell BCAP3400 (middle right), and the General Capacitor 3000F (bottom).

The modules procured were subject to the same cycling procedure as their cell counterparts but they were cycled longer due to their higher thermal mass. Figure 30 displays the electrical data collected when cycling reach respective 48 V module. Similar to the repetitive experiments conducted at the cell level, voltage drops due to each respective module are observed during the charge and discharge transitions. As one would expect, the electrical data collected is very similar in nature to that collected at the cell level. The Skeleton module has less than half the ESR as the other modules tested, which results in the lowest voltage drop. The Maxwell and Ioxus modules have nearly identical ESRs since the individual cells are so similar. The JM energy module experienced the largest voltage drop due to the module's overall higher ESR. The module data gathered aligns well with the tests conducted on each of the individual cells.

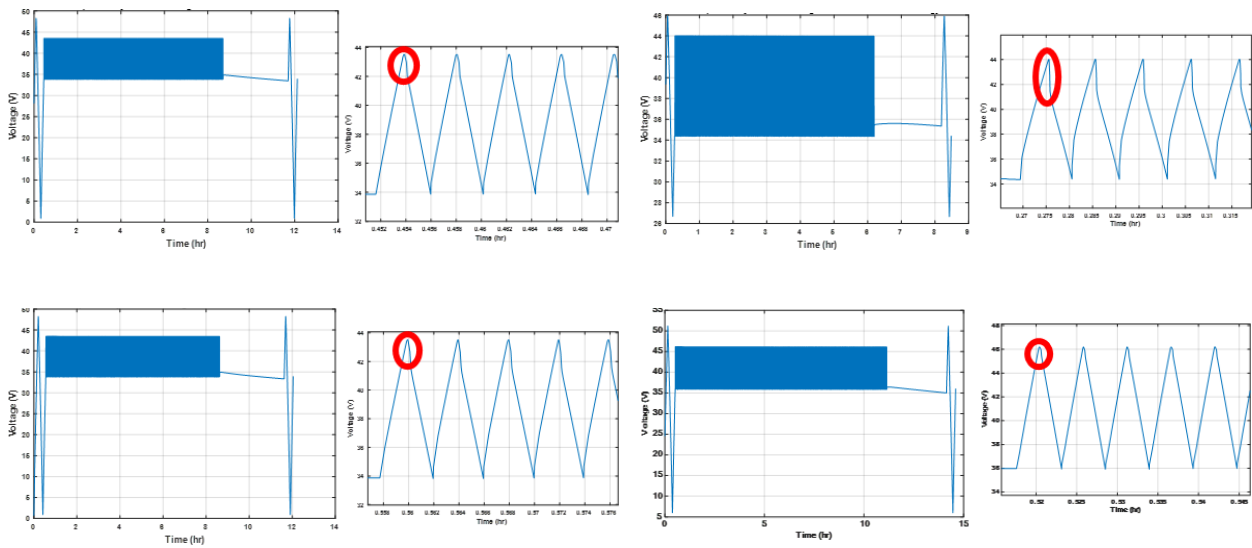


Figure 30: Voltage measurements made from each respective UC module studied including the Ioxus iMOD048V166A23 (top left), JM Energy Ultimo 3300F prismatic (top right), Maxwell

BMOD0165 P048 C01 (bottom left), and SMOD48V178F (bottom right), when subject to the repetitive transient procedure at 200 A.

The thermal data collected during each 48 V module level experiment are shown below. The modules were cycled until thermal equilibrium was reached or until its rated temperature was exceeded. The data collected from the 48 V Maxwell module is shown in Figure 31.

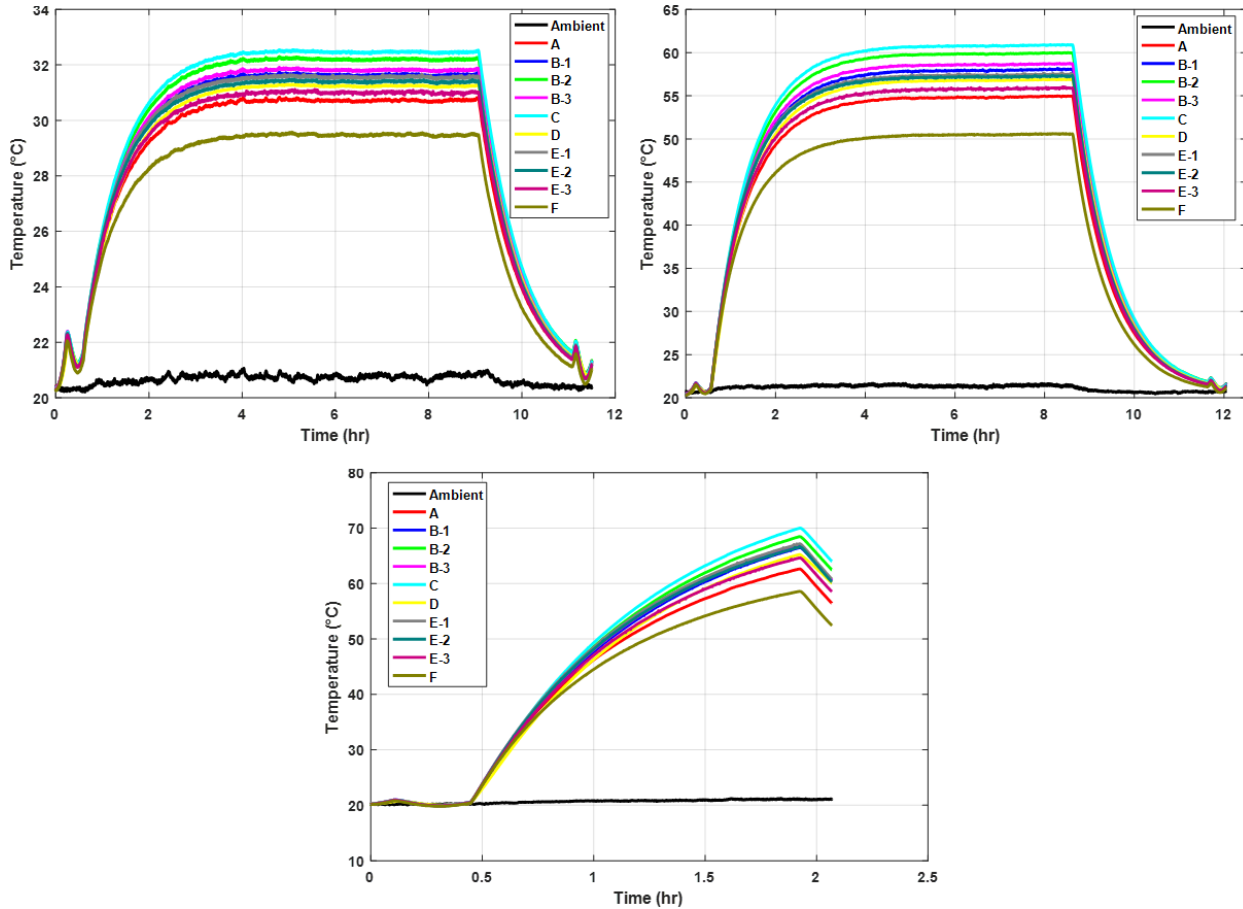


Figure 31: Thermal data gathered when cycling the Maxwell 48 V at 100 A (top left), 200A (top right), and 250 A (bottom).

The Maxwell 48 V module was evaluated at currents of 100 A, 200 A, and 250 A tests. It was only able to complete the 100 A and 200 A tests, respectively. The module reached and was able to maintain thermal equilibrium at 65°C during the 200 A test. The 250 A test was aborted once the modules temperature reached 70°C, nearly 2 hours into the test, in order avoid any damage to the cells. Each of the plots in Figure 31 contain a legend that corresponds with the thermocouple

placement seen in Figure 18. Figure 32 contains the thermal data gathered when testing the Ioxus 48 V module.

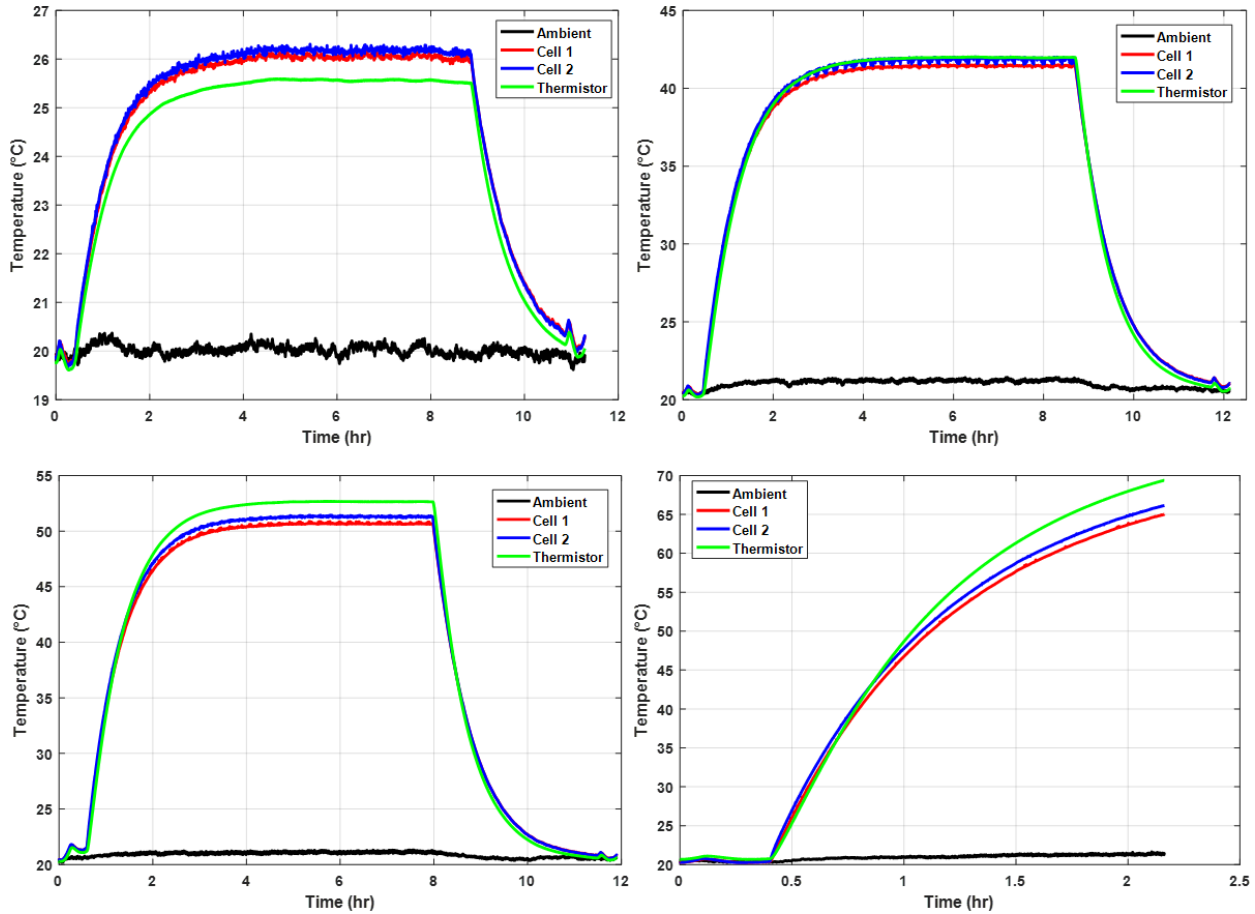


Figure 32: Thermal data gathered when cycling the Ioxus 48 V at 100 A (top left), 200A (top right), 250 A (bottom left), and 300 A (bottom right).

The Ioxus module was evaluated at current rates of 100 A, 200 A, 250 A, and 300 A, respectively. It was only able to complete the 100 A, 200 A, and 250 A experiments. The repetitive cycling procedure was cutoff just over 2 hours into the 300 A test when its temperature reached 70°C. The thermal data gathered when cycling the JM Energy 45 V module can be seen in Figure 33 below.

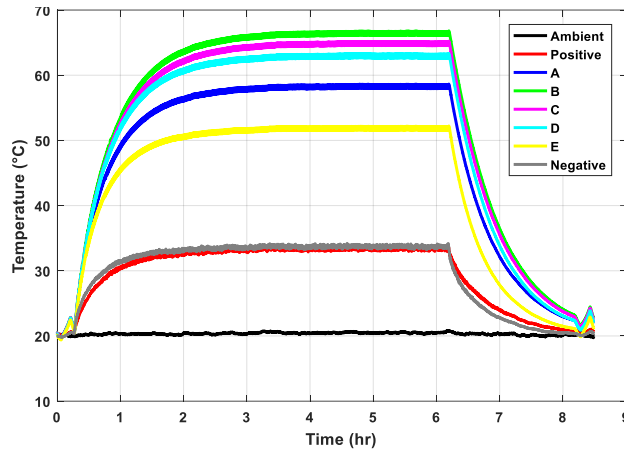


Figure 33: Thermal data gathered when cycling the JM Energy 45 V module at 100 A.

The JM Energy module was only able to complete the 100 A experiment, reaching thermal equilibrium at roughly 66°C. Due to the module reaching thermal equilibrium at its rated operating temperature, additional experiments were not even attempted. The thermal data gathered from the Skeleton 51 V module can be seen below in Figure 34.

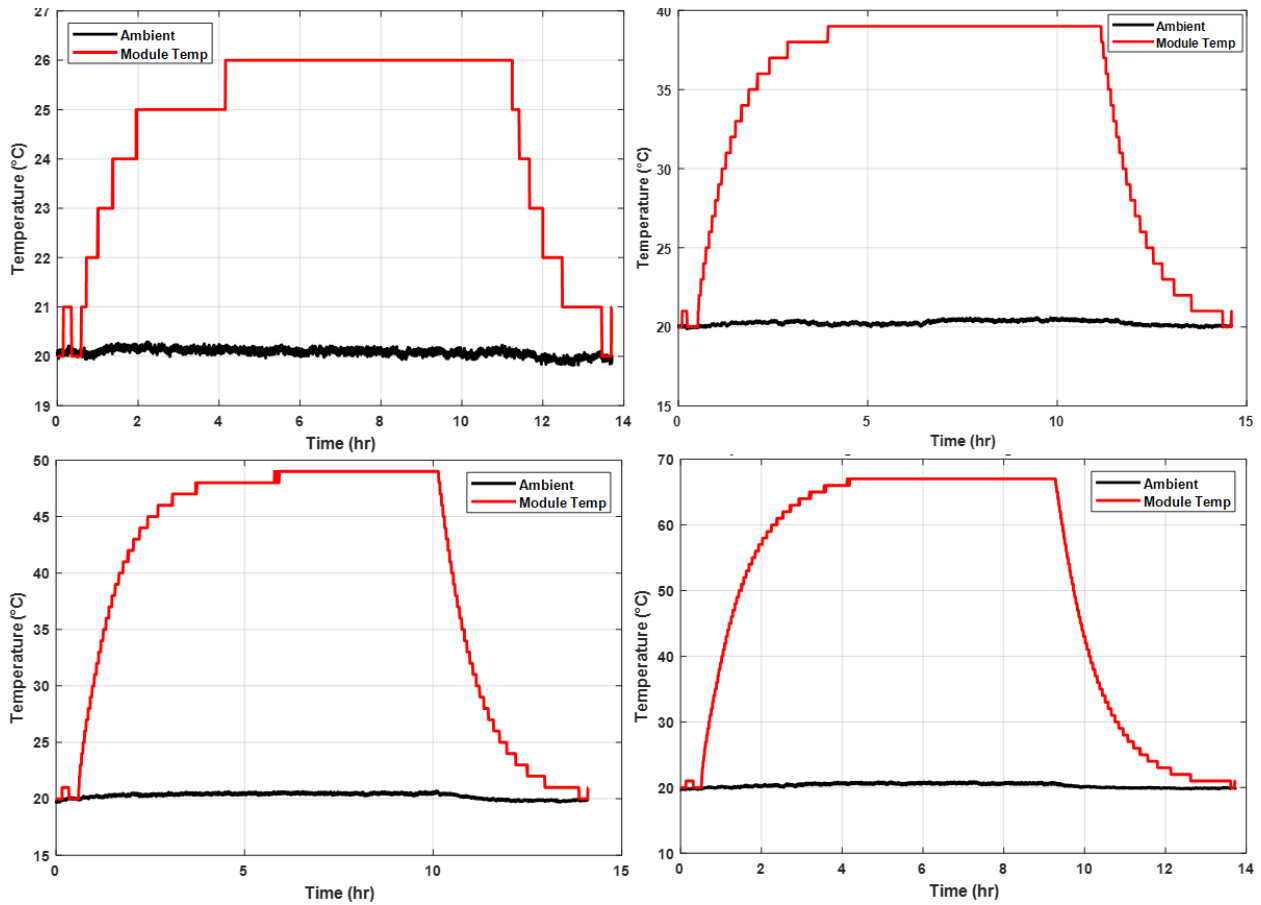


Figure 34: Thermal data gathered when cycling the Skeleton 51 V at 100 A (top left), 200A (top right), 250 A (bottom left), and 300 A (bottom right).

The Skeleton 51 V module was able to complete all experiments at 100 A, 200 A, 250 A, and 300 A, respectively, without experiencing any temperature cutoffs. The maximum temperature the module reached was roughly 66°C thermal equilibrium during the 300 A test. The highest temperature inside the module is determined by four temperature sensors that are preinstalled and the information is sent via CAN communication.

The experiments show that the Maxwell and Ioxus cells are almost identical in their electrical and thermal performance. While the electrical performance is still nearly identical at the modular level, their thermal performance does differ significantly. The Maxwell 48 V module was only able to complete the 100 A and 200 A tests, reaching a peak temperature of 61°C. The module,

when subject to the 250 A test, could not cycle for over 2 hours before reaching thermal cutoff at 70°C. However, the Ioxus module was able to complete the 100 A, 200 A, and 250 A test, reaching a peak temperature of only 53°C. The Ioxus module was also subject to the 300 A test and was able to cycle for just over 2 hours before exceeding its thermal limits. The difference in the thermal performance in the two module is likely not due to the electrical characteristic of the individual cells, but rather the methods used to encase the cells within the modules. Figure 18 contains a photograph of the inside of the Maxwell 48 V module. The photograph shows that the cells are oriented vertically and are connected using bus work directly under the top of the module. Similarly Figure 19 contains a photograph of the inside of the Ioxus 48 V module. It may not be clear in the photograph, but the cells are oriented horizontally and the module is filled with the thermal interface material previously mentioned. The JM Energy 45 V module was only able to complete the 100 A repetitive transient test, reaching a peak temperature of roughly 66°C, just above the cell's rated operating temperature. Due to the individual LICs' high ESR the module was not able to perform any test at higher current ranges without reaching thermal cutoff. The high temperatures are likely due to ohmic heating, seen in the cell thermal profiles in Figure 33, and the construction of the module itself. Figure 20 contains a photograph of the module, the cells are pressed against one another with no structure acting as a heat sink to dissipate the cell's heat, unlike in the Maxwell and Ioxus 48 V modules. The Skeleton module was the only low voltage UC module that was able to complete the full range of the repetitive transient procedure. This is likely due to the combination of the individual cell's low ESR and the fact that the module is potted, similar to the Ioxus module.

The two modules with higher rated voltages were also subjected to the same repetitive transient procedure. The Ioxus 96 V and Skeleton 170 V modules were tested with and without the use of

liquid cooling, as discussed in the experimental test plan section. Figure 35 plots a sample of the electrical data collected from each respective module.

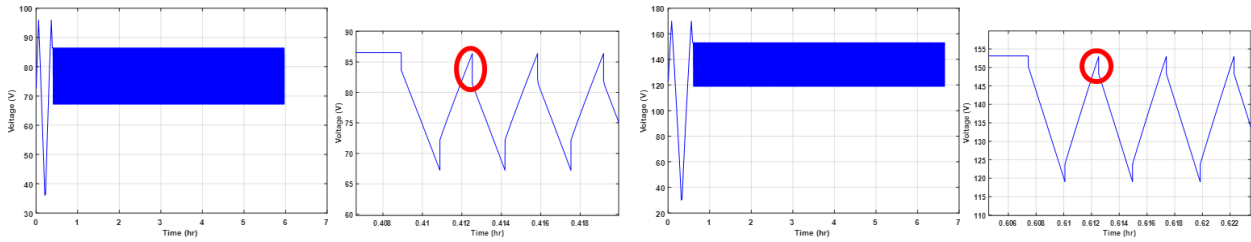


Figure 35: Voltage measurements made from each respective UC module studied including the Ioxus iMOD096V083A23-LQ (left) and the Skeleton SMOD170V53F (right), when subject to the repetitive transient procedure at 200 A.

The Ioxus 96 V module contains 36 individual iRB3000K270CT cells and the Skeleton 170 V module contains 60 SCA3200 cells. Even though the Skeleton module is comprised of nearly twice the number of cells, the two modules' voltage drops are nearly the same. In fact, the Ioxus 96 V module has a slightly larger voltage drop than the Skeleton module. The baseline conducted at the beginning of the repetitive transient test revealed that the Ioxus 96 V has an ESR of roughly 13 m Ω and Skeleton 170 V has an ESR of roughly 10 m Ω . In the 200 A test, seen in Figure 35, the difference in ESR accounts for a 0.6 V difference in the two module's transitional voltage drop.

As stated previously, both modules were cycled in an open room ambient condition, with and without the use of liquid cooling. The open room ambient condition means that the ambient air temperature will fluctuate throughout the test and is likely more representative of the modules typical operational environment. Figure 36 shows the thermal results collected from the Ioxus 96 V module when subject to the full range of repetitive transient testing with the use of liquid cooling.

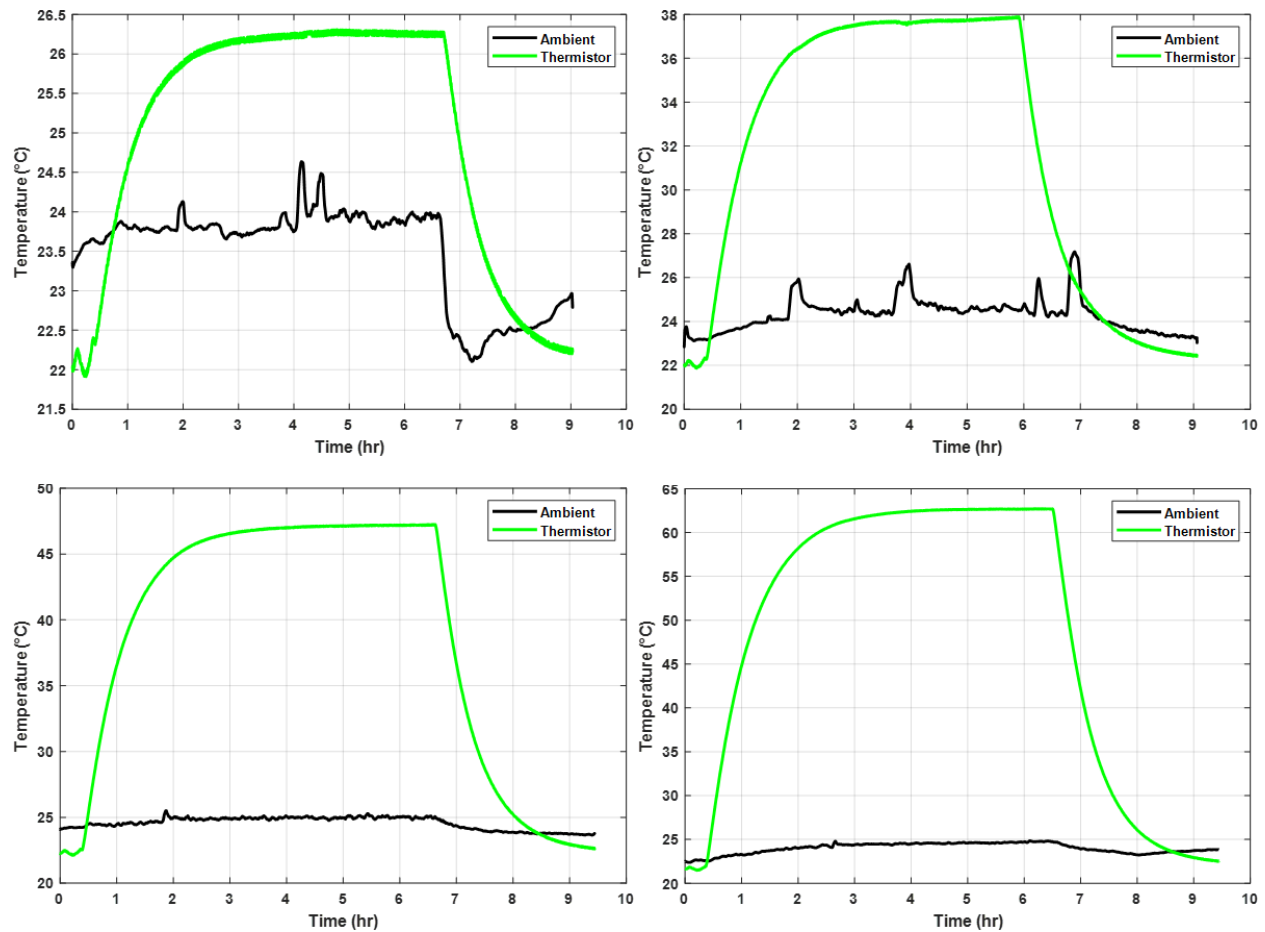


Figure 36: Thermal data collected when cycling the Ioxus 96 V module at 100 A (top left), 200A (top right), 250 A (bottom left), and 300 A (bottom right), in ambient room conditions with liquid cooling.

During the 300 A test, the module evaluated in this study reached a peak temperature of roughly 63°C. In this study, through the use of liquid cooling, the Ioxus 96 V module was able to reach thermal equilibrium and complete the repetitive transient procedure for each current range. As previously mentioned, the ambient temperature does fluctuate a bit. The sudden drop in ambient temperature is due to the Chroma cycler being shut off upon the tests completion. It is evident from Figure 36 that the module reached a peak temperature of roughly 63°C during the 300 A test. The Ioxus module's datasheet is a bit different from the others in the fact that they list a rated temperature based on the operational voltage. At a rated voltage of 2.7 V the cell has a rated

temperature of 85°C and when operated at a rated voltage of 2.85 the cell has a rated temperature of 65°C. When subject to the 300 A test, the voltage window is 50% - 100% and the cell reached 63°C, only 2°C below the module’s rated temperature. The other tests were performed with a voltage window of 70% - 90% and a peak temperature of 47°C was witnessed during the 250 A test. Therefore when cycled from 70% - 90% of the cells rated voltage, the peak temperature was roughly 38°C under the module’s rated temperature. Figure 37 contains the thermal data using the same module when subject to the same tests but without the use of liquid cooling.

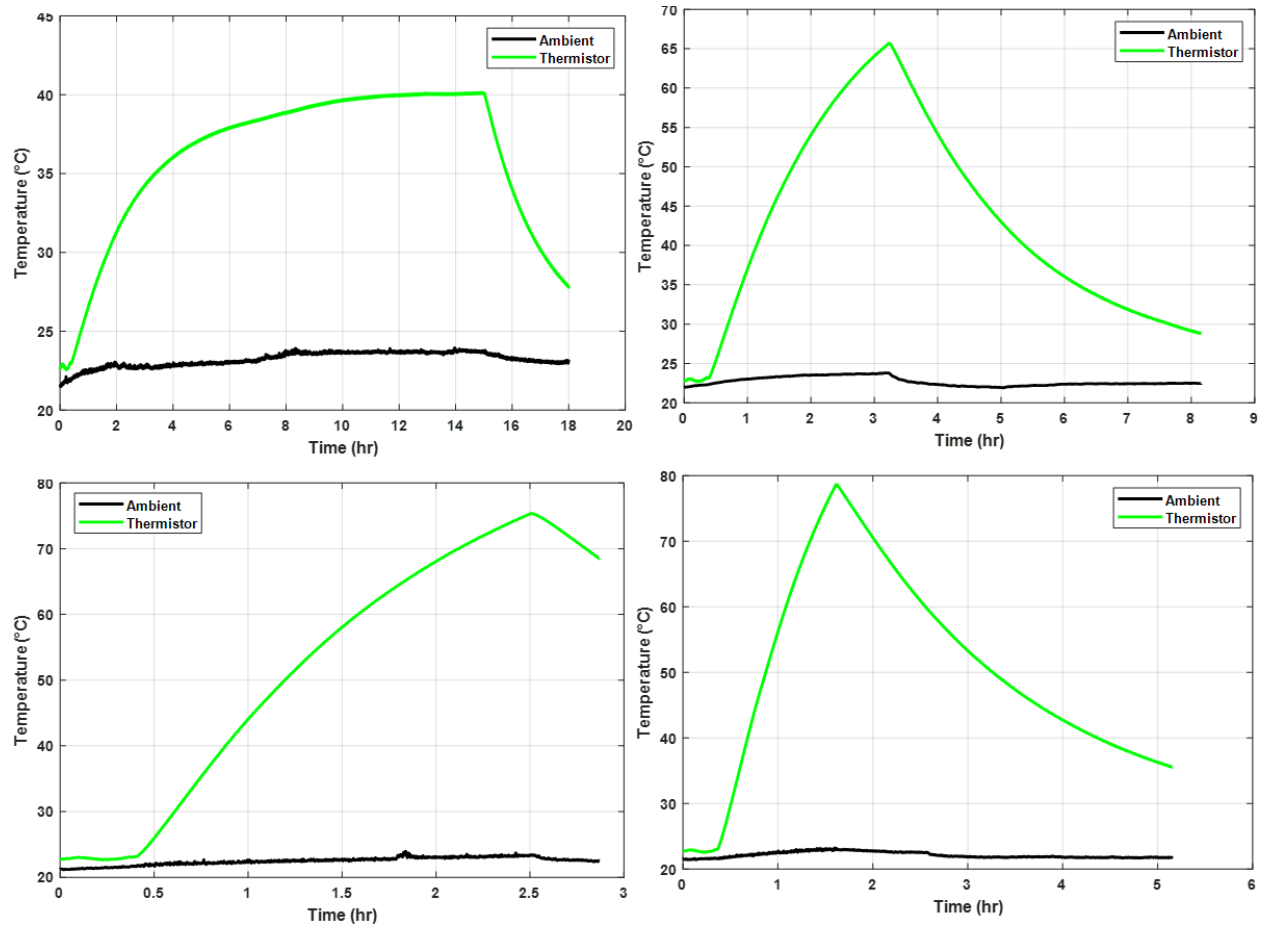
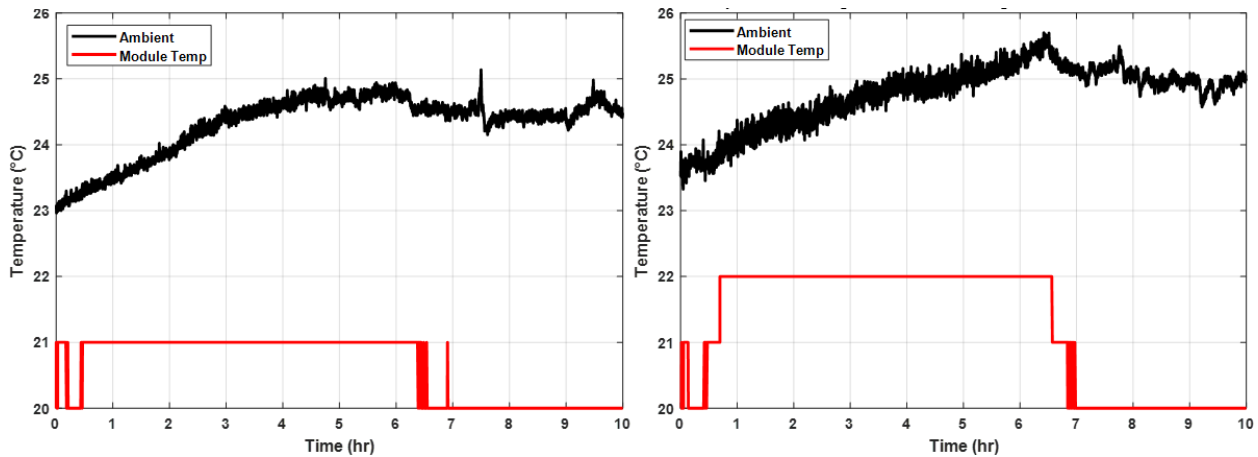


Figure 37: Thermal data gathered when cycling the Ioxus 96 V module at 100 A (top left), 200A (top right), 250 A (bottom left), and 300 A (bottom right), in an open room environment and without the use of liquid cooling.

Without the use of liquid cooling, the Ioxus 96 V module was only able to reach thermal equilibrium and complete the 100 A test. The module was subject to the other remaining tests but each was terminated to avoid damage due to high temperatures. It is apparent that the use of liquid cooling at 20°C has a large impact on the thermal performance of the module.

The Skeleton 170 V module was subject to the same repetitive test procedure in the same environment in which the Ioxus 96 V module was tested. Figure 38 contains the thermal results measured from the Skeleton 170 V module when subjected to the full range of repetitive transient testing with the use of liquid cooling. Similar to the Ioxus 96 V module, the Skeleton 170 V module was able to complete the entire range of repetitive transient testing. The module reached a peak temperature of 26°C when cycled at 300 A repetitively. With the use of liquid cooling, the temperature of the Skeleton module did not exceed the ambient air temperature until it was cycled at 300 A test during which the module reach thermal equilibrium roughly 1°C over ambient temperature. Even when cycled at 300 A the Skeleton module reached thermal equilibrium nearly 40°C below its rated temperature.



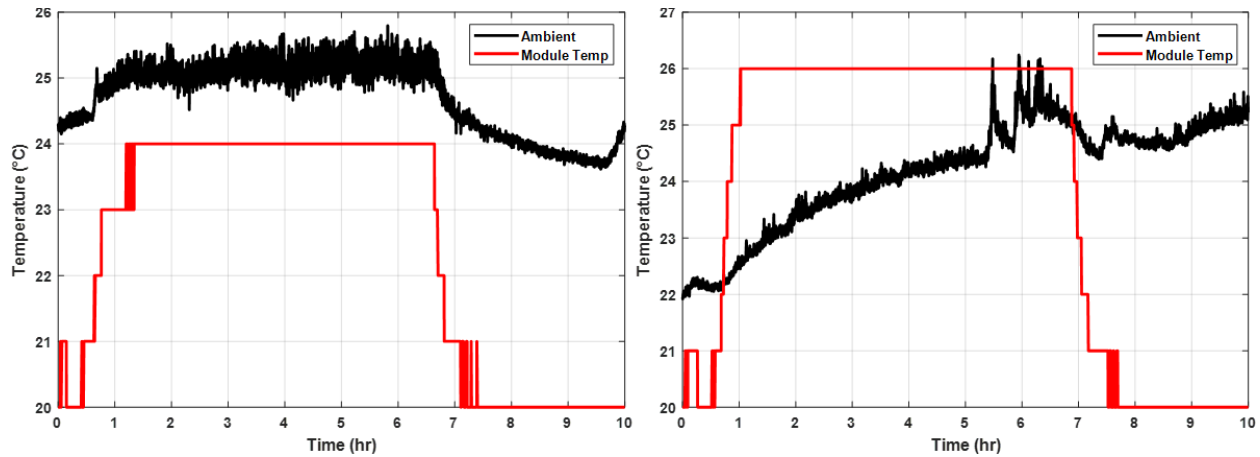


Figure 38: Thermal data gathered when cycling the Skeleton 170 V module at 100 A (top left), 200A (top right), 250 A (bottom left), and 300 A (bottom right), in an open room environment and with the use of liquid cooling.

Once the Skeleton 170 V module completed the series of repetitive transient tests with the use of liquid cooling, the module was then evaluated in the same way but without the use of liquid cooling. Figure 39 presents the thermal data collected when the Skeleton module was cycled without the use of liquid cooling. During those experiments, the Skeleton 170 V module was able to reach thermal equilibrium and complete the 100 A and 200 A tests. When cycled at 250 A and 300 A, respectively, the module reached thermal cutoff before thermal equilibrium was achieved.

Analysis of these results show that the Skeleton module outperformed the Ioxus thermally throughout the entire range of repetitive transient testing, with and without the use of liquid cooling. Though the Skeleton module’s voltage is substantially higher, the overall performance is significantly better. The temperature of the Skeleton module is consistently and significantly lower than the temperature of the Ioxus module for each respective test, even though the Skeleton cell has more cells in series. During the series of experiments performed with liquid cooling, the Ioxus module exceeded 60°C during the 300 A test. The Skeleton module, on the other hand, reached a peak temperature of only 26°C, only slightly above the temperature of the surrounding ambient

air. Without the use of liquid cooling, the Ioxus 96 V module was only able to reach thermal equilibrium during the 100 A test without reaching dangerously high temperatures. The Skeleton module was able to reach thermal equilibrium during the 100 A and 200 A tests. The Skeleton module also was able to cycle for longer periods of time than the Ioxus module before reaching thermal cutoff. Overall the low ESR and method of the Skeleton module construction led to a higher thermal performance than the Ioxus module.

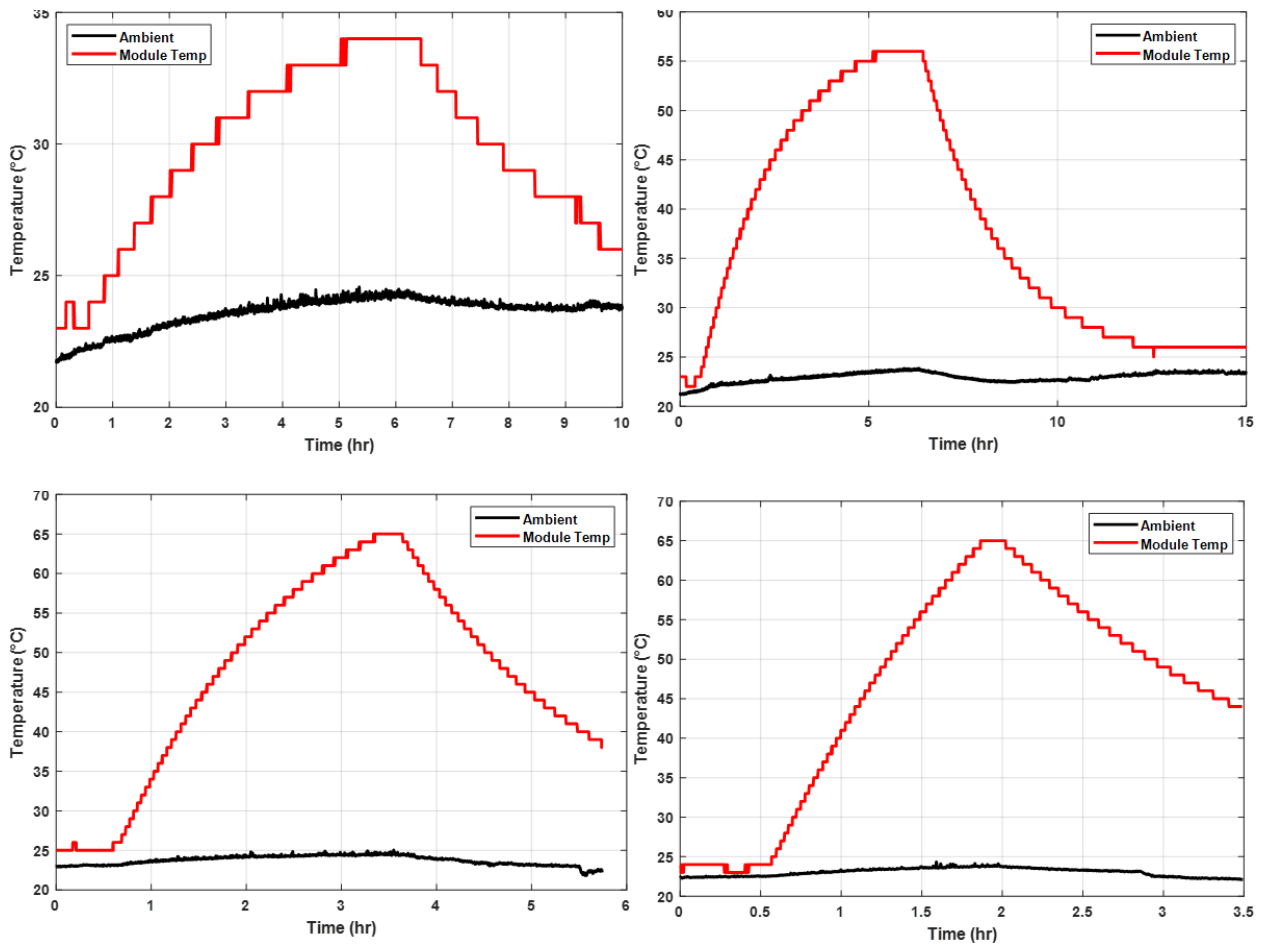


Figure 39: Thermal data gathered when cycling the Skeleton 170 V module at 100 A (top left), 200A (top right), 250 A (bottom left), and 300 A (bottom right), in an open room environment and without the use of liquid cooling.

Ultracapacitor Model

Once the experiments discussed above are completed, an accurate UC cell model is created using the electrical data gathered during testing. The model was created using the blocks provided within the Simulink environment, equations from existing literature, and the data gathered for each respective UC evaluated in this study [30, 31]. The model can be validated against the results gathered from the single transient discharge and the repetitive transient cycling tests. Below, Figure 40 contains a diagram of the equivalent circuit representing a UC model.

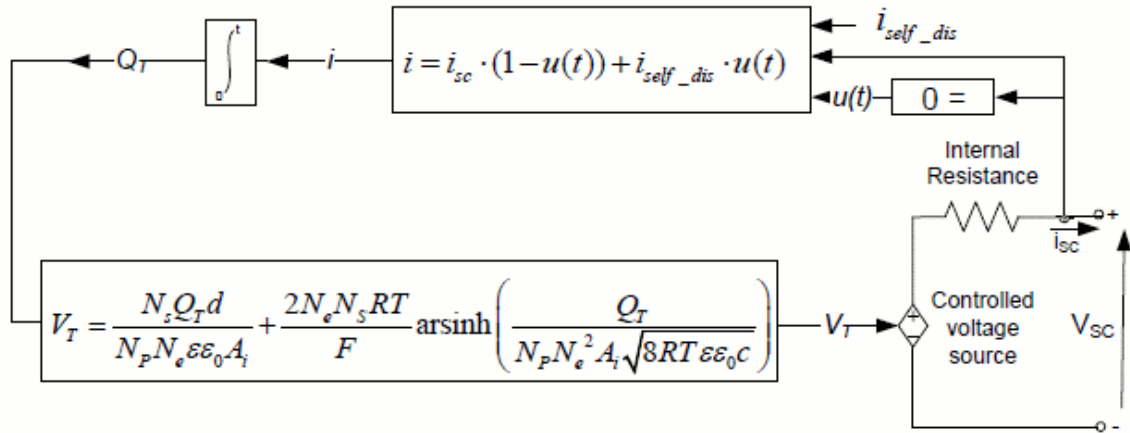


Figure 40: Diagram of an equivalent circuit representing the ultracapacitor model [31].

Where,

A_i is the interfacial area between electrodes and electrolyte (m^2)

c is the molar concentration

F is the Faraday constant

i_{sc} is the ultracapacitor current (A)

V_{SC} is the ultracapacitor voltage (V)

N_e is the number of layers of electrodes

N_p is the number of parallel ultracapacitors

N_s is the number of series ultracapacitors

Q_T is the electric charge (C)

R is the ideal gas constant

R_{SC} is the total resistance (Ω)

D is the molecular radius

T is the operating temperature (K)

E is the permittivity of material

ϵ_0 is the permittivity of free space

The UC output voltage can be derived from the equivalent circuit diagram shown in Figure 40.

The model is split into two subsystems, the Stern model that represents equation 3 and the self-discharge model that represents when equation 4 is equal to zero. The first subsystem discussed is the stern model that can be seen in Figure 41.

$$V_{SC} = \frac{N_s Q_T d}{N_p N_e \epsilon \epsilon_0 A_i} + \frac{2 N_e N_s R T}{F} \sinh^{-1} \left(\frac{Q_T}{N_p N_e^2 A_i \sqrt{8 R T \epsilon \epsilon_0 c}} \right) - R_{SC} \cdot i_{SC} \quad (3)$$

where,

$$Q_T = \int i_{SC} dt \quad (4)$$

Figure 41 contains a diagram the Stern model subsystem, which represents the UC output voltage seen above expressed in equation 3. The parameters are allowed to be specified for the type of UC being modeled and the mathematical blocks provided in the Simulink environment are used to calculate the UC's output voltage and capacitance.

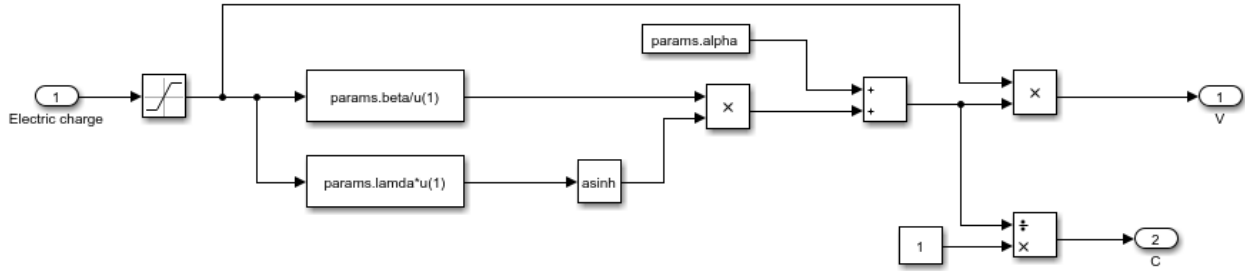


Figure 41: Diagram of the Stern model representing the output UC voltage seen in equation 3.

The other subsystem is the self-discharge model used to simulate when the current through the UC is equal to zero. The self-discharge current is determined using equation 5, with the equations time intervals corresponding to Figure 42 below. The constants a_1 , a_2 , and a_3 are the rates of change of the UC voltage during the time intervals shown in equation 5.

$$i_{self_dis} = \begin{cases} \frac{C_T \alpha_1}{1 + sR_{SC}C_T} & \text{if } t - t_{oc} \leq t_3 \\ \frac{C_T \alpha_2}{1 + sR_{SC}C_T} & \text{if } t_3 < t - t_{oc} \leq t_4 \\ \frac{C_T \alpha_3}{1 + sR_{SC}C_T} & \text{if } t - t_{oc} > t_4 \end{cases} \quad (5)$$

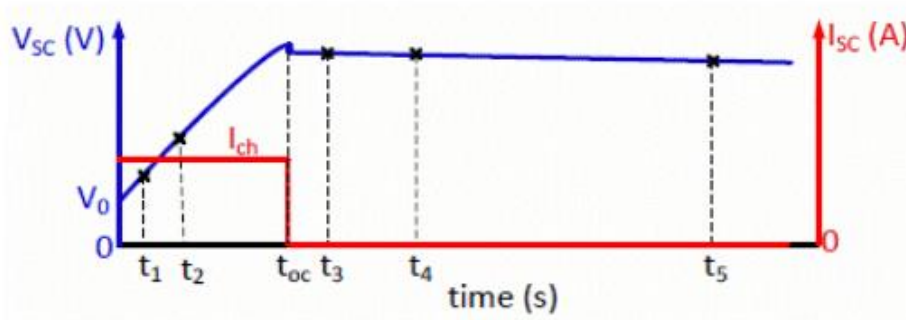


Figure 42: Diagram showing the time bounds used in equation 5 to determine the UC's self-discharge current [31].

Similar to the stern model, the parameters are set according the type of UC being modeled. The model allows the user to input the current prior to open circuit and then allows for the input of the cells voltage corresponding to t_{oc} , t_3 , t_4 , and t_5 to simulate the cell's self-discharge. The math is then carried out using a number of the mathematical blocks offered in the Simulink environment.

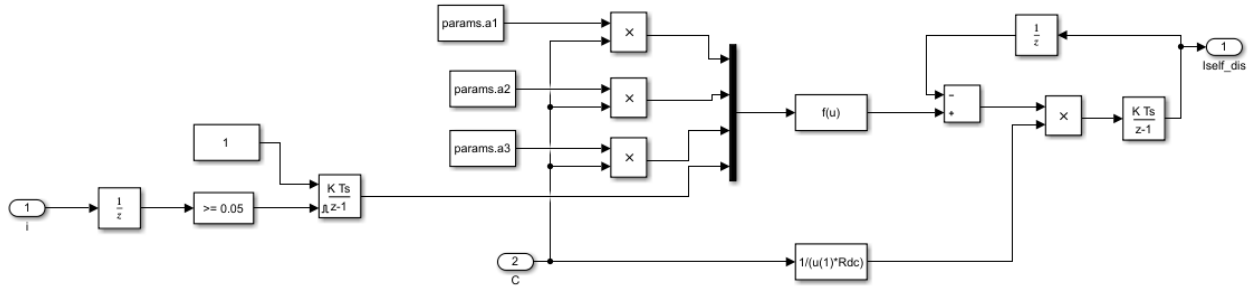


Figure 43: Diagram of the self-discharge model representing the UC self -discharge equation 5. The calculated self-discharge current is then passed to the primary UC model shown in Figure 44. The diagram shows the Stern model and self-discharge model in subsystems with their UC voltage and current calculations being output for measurement. The self-discharge current is subtracted from the current through the capacitor and then integrated to calculate charge, which is added to the cell's initial charge to determine the total charge stored in the cell. The cell's rated charge is then calculated and the difference between the cell's rated charge and calculated charge is used to determine the UC's state of charge (SoC).

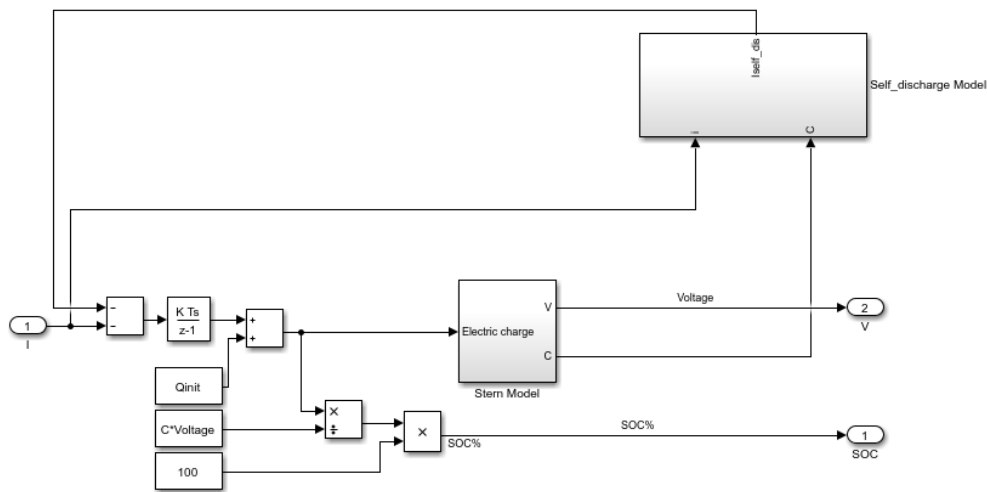


Figure 44: Diagram of the UC model incorporating the Stern and self-discharge models.

Model Validation

The UC model is validated using the electrical data gathered from the single transient discharge and repetitively transient cycling tests discussed in the sections above. Figure 45 shows a diagram of the model that contains each of the UCs simulating the single transient discharge experiment. The transient discharge test stand is represented in the model by a resistive and inductive branch that is then connected to an ideal switch. The ideal switch is controlled by a signal generator that commands the switch to be closed for 200 ms, representing the parallel MOSFETs and the control signal from labVIEW. Each of the UCs output voltage and current are sent to MATLAB to generate the single discharge voltage and current profiles shown in Figures 46 and 47.

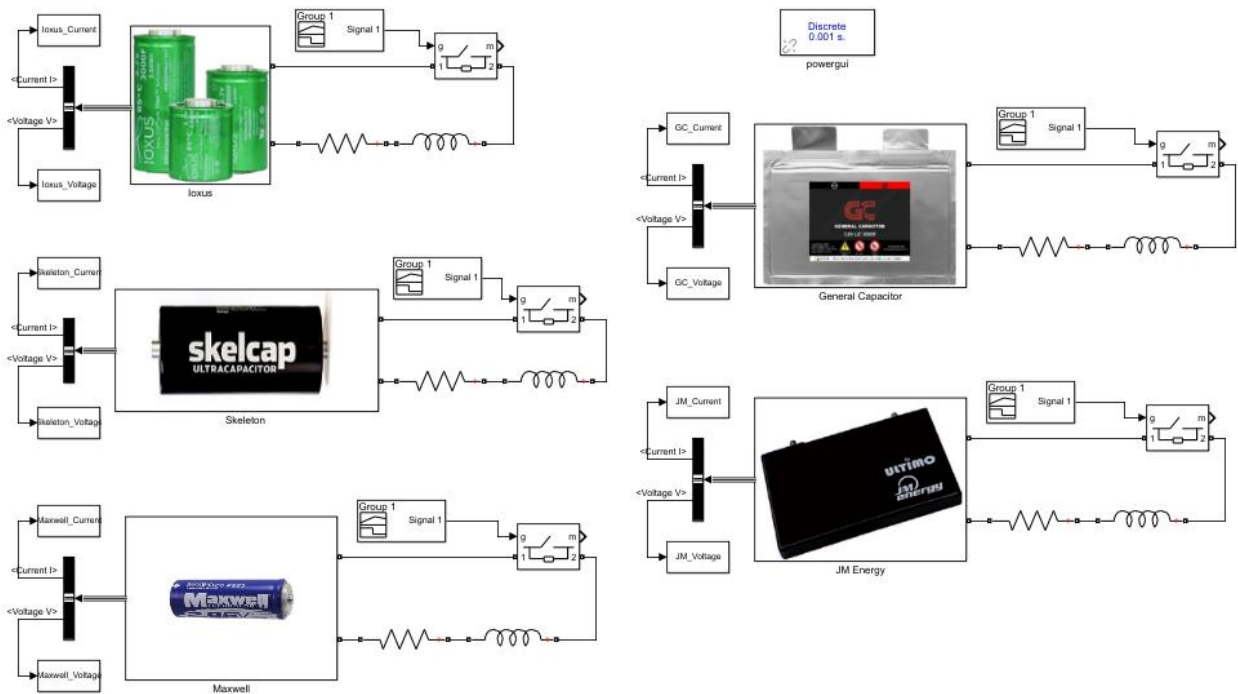


Figure 45: Diagram of the UC model simulating the single transient discharge experiment for each of the five UCs tested.

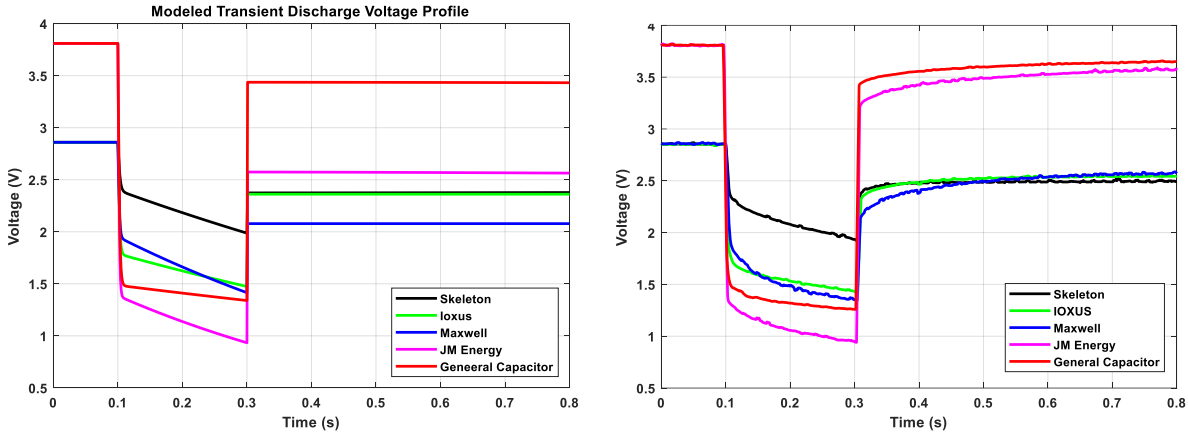


Figure 46: Comparison between the simulated and recorded transient discharge voltage profiles.

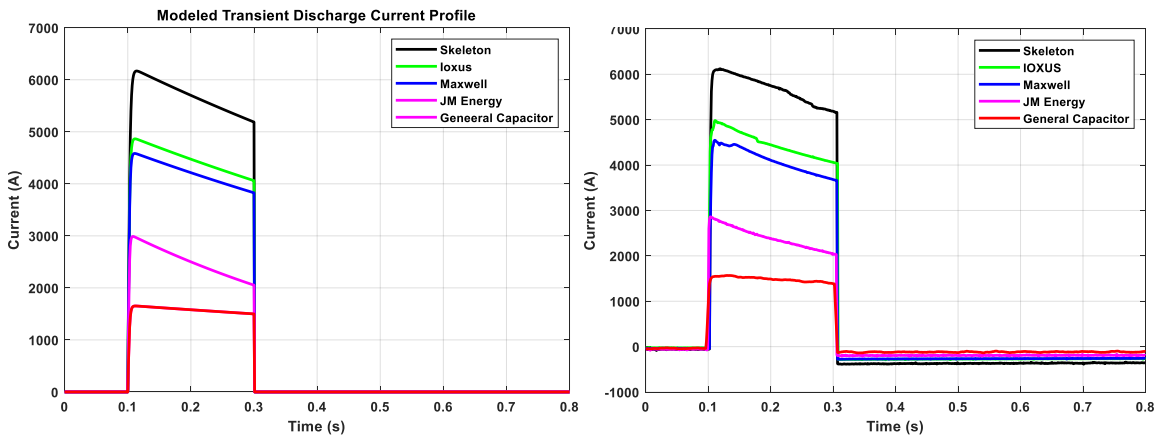


Figure 47: Comparison between the simulated and recorded transient discharge current profiles.

Figures 46 and 47 provide a comparison of the simulated and recorded single transient discharge voltage and current profiles. The simulated voltage and current profiles of each of the five UCs align well with the data recorded from testing. The next validation method is to use the model to simulate the repetitive transient cycling testing and compare the simulated and recorded data. The model shown in Figure 45 was modified to simulate the repetitive transient cycling test at 200 A for all UCs. Due to the General Capacitors cell's high ESR the voltage profile was distorted due to the power supply and load reaching constant voltage (CV) when the cell transitioned during cycling. Therefore the simulation current for the General Capacitor was set to 100 A and will be

compared to the data recorded when the cell was cycled at 100 A. Figures 48 – 52 contain comparisons of the simulated and recorded voltage profiles for the repetitive transient cycling tests.

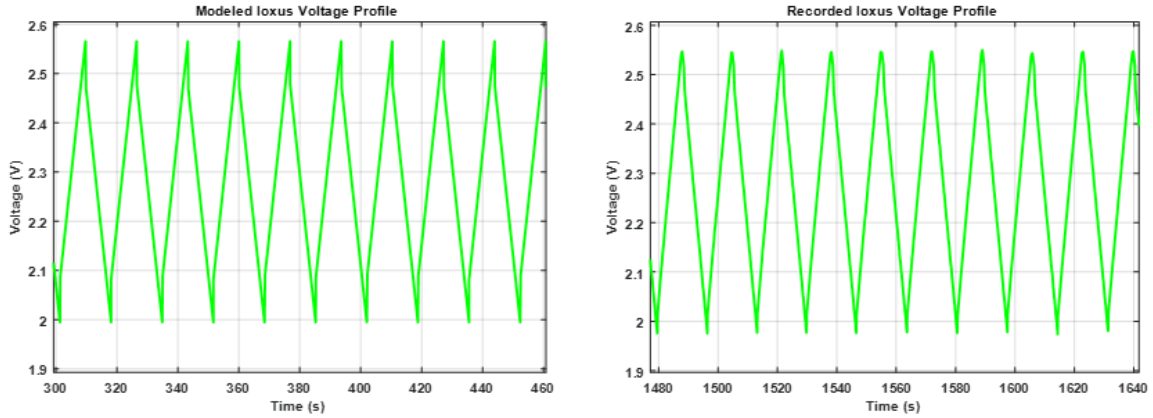


Figure 48: Comparison between the simulated and recorded repetitively cycled voltage profiles for the Ioxus EDLC when cycled at 200 A.

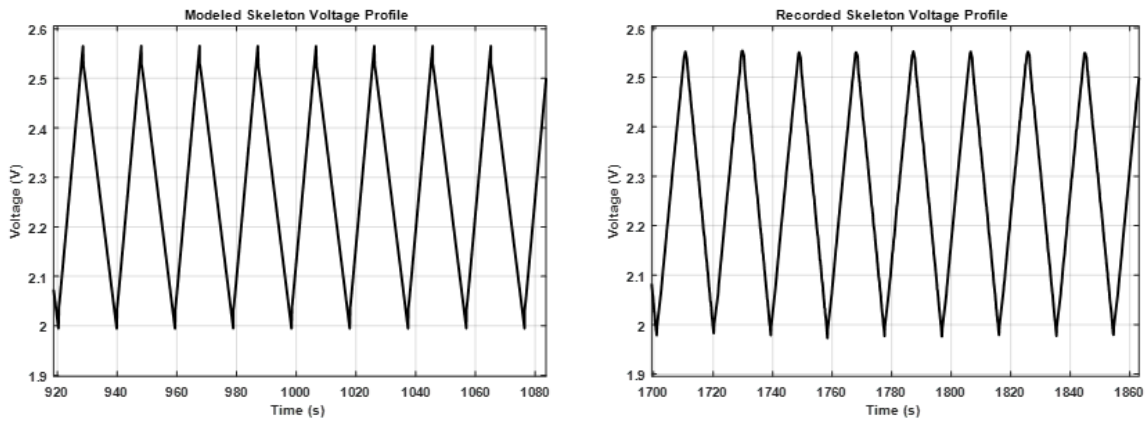


Figure 49: Comparison between the simulated and recorded repetitively cycled voltage profiles for the Skeleton EDLC when cycled at 200 A.

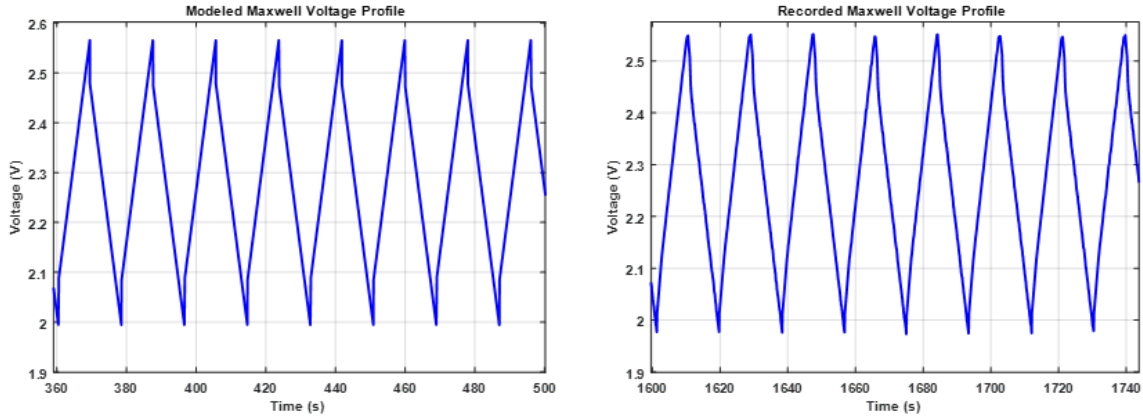


Figure 50: Comparison between the simulated and recorded repetitively cycled voltage profiles for the Maxwell EDLC when cycled at 200 A.

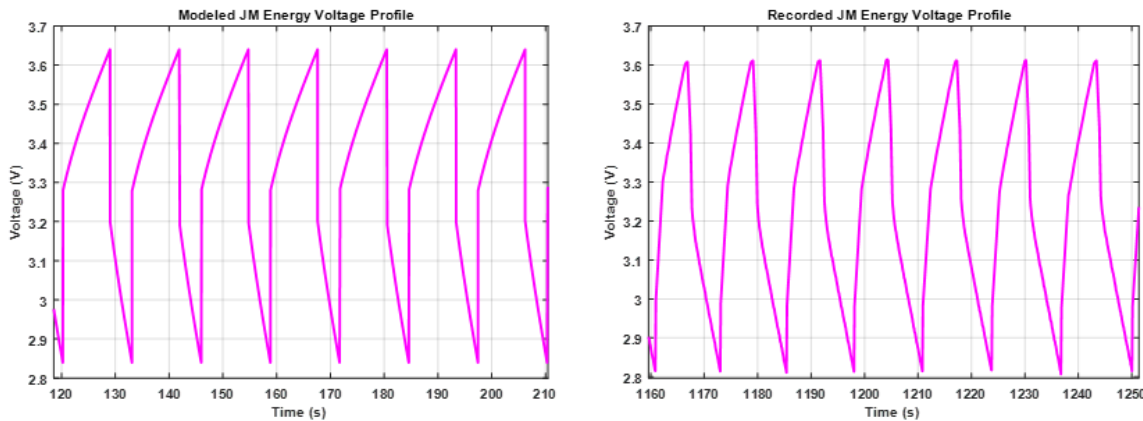


Figure 51: Comparison between the simulated and recorded repetitively cycled voltage profiles for the JM Energy LIC when cycled at 200 A.

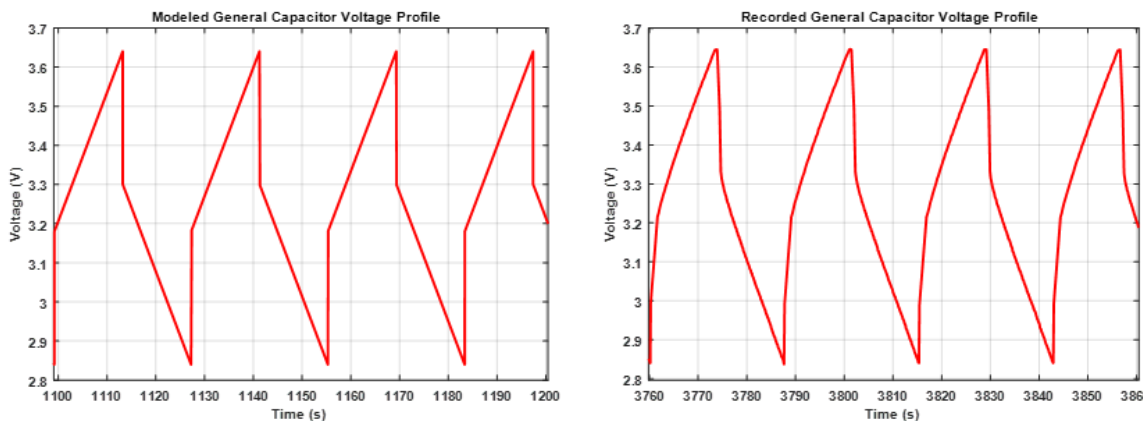


Figure 52: Comparison between the simulated and recorded repetitively cycled voltage profiles for the General Capacitor LIC when cycled at 100 A.

Conclusion

This study was an effort to perform a like-for-like comparison across different UC technologies, with a focus on the recent claims made by Skeleton Technologies. Through the use of curved graphene Skeleton Technologies claims that their UCs have a significantly lower ESR than other competitive UCs, resulting in a much higher power density. A comparison was made through the execution of multiple tests discussed in the sections above that determine each cells electrical and thermal characteristics.

The first of these tests is the initial characterization of each cells capacity and ESR through the use of EIS. Each of the cells had an initial capacitance at or above the rated capacitance given in their respective datasheets, with the exception of the Maxwell cell which was roughly 100 F under its rated value. The EIS measurements revealed that the Skeleton 3200 F cell had just over half of the DC ESR as the other EDLCs and approximately 1/10th the DC ESR as the LICs. This was a validation of Skeleton Technologies' claim that their use of curved graphene dramatically reduced their cells ESR.

The following test was the low impedance load single transient experiment that was used to validate each of the cells impedance, as well as each of the cells respective peak power and therefore power density. This experiment validated the findings from the EIS measurements and clearly showed that the Skeleton 3200 F cell has significantly lower ESR than any of the other cells. Using each cells conduction voltage and current, measurements each of the cells peak power was determined. The Skeleton cell was able to produce over 3 kW more power than the other cells. This resulted in a cell that was 10 kW/kg more power dense than any of the other cells tested in this experiment. Once again confirming the claims made by Skeleton Technologies, that their cells have less ESR and are more power dense than their competitors.

The third set of tests were the cell and module repetitive transient evaluation to determine electrical and thermal characteristics. From the electrical data gathered on the cell level it is apparent that the EDLCs experienced a significantly lower transitional voltage drop due to their ESR. The LICs experience such a large voltage drop during charge and discharge transitions that their operational window was widened and the General Capacitor cell would transition into CV when cycled at 200 A. The size of the transitional voltage drop that each cell experienced was directly related to the amount of heat the cell created when cycled. The Skeleton cell, due to its significantly lower ESR, performed the best in this set of experiments. The other two EDLCs experienced maximum temperatures a few degree higher than the Skeleton cell. The LICs experienced the largest increase in temperature, similarly due to each respective cells high ESR. The JM Energy cell was able to complete the full range of testing, unlike the General Capacitor cell that was only able to complete the 100 A and 200 A tests, both cells reaching temperatures above 50°C. This experiment shows the electrical and thermal advantages that the Skeleton cell gains by having a lower ESR than the other cells.

The same set of tests were conducted at the module level, where various low voltage modules and two high voltage modules were compared, respectively. With respect to the low voltage module testing, the Skeleton 51 V module performed better than the others electrically and thermally. Due to the individual cells low ESR, the Skeleton 51 V module experienced the lowest transitional voltage drop. Similar to the tests at the cell level, the module that experienced the lowest transitional voltage drop and performed better thermally as well. The Skeleton module 51 V module was the only of the low voltage modules to complete the full range of testing without reaching thermal cutoff. The next best thermal performance was given by the Ioxus 48 V module, which was able to complete the 250 A test and reached thermal cutoff during the 300 A test. The

Maxell module was only able to complete the 200 A test before reaching thermal cutoff during the 250 A test, despite the similar electrical characteristics. This was likely due to the fact the Ioxus fills their modules with a thermal epoxy upon completion, whereas the Maxwell module only contains the cells and bus work without any thermal interface to the modules walls. The JM Energy 45 V module was only able to complete the 100 A test due to the modules high impedance and the method of module construction.

The two high voltage module that were compared in this study were the 96 V Ioxus module and the 170 V Skeleton module, both capable of liquid cooling. Both modules were cycled in an open room environment, with and without the use of coolant and with a fluctuating ambient temperature that would be more representative of their normal operational condition. The Skeleton 170 V module showed to produce a smaller transitional voltage drop than the 96 V Ioxus module. Both modules were able to complete the full range of tests, when using liquid cooling. The difference being, the maximum temperature that the Skeleton module experienced was nearly 40°C below the maximum temperature the Ioxus module recorded. Without the use of liquid cooling the Skeleton 170 module was able to complete the 100 A and 200 A tests before reaching thermal cutoff, while the Ioxus 96 V module was only able to complete the 100 A test before reaching thermal cutoff during the remaining tests. This again goes to show that the impact of having a significantly lower ESR than the other competitive cells.

Overall the objective of this study was to make a like-for-like comparison of multiple UCs from leading competitors for integration into existing power system architectures. It is apparent from the series of experiments conducted that the Skeleton UCs have significantly lower ESR than any of the other cells obtained for this study. The cells low ESR results in a much higher power density than the other EDLCs as well. The benefit of this can be seen in the repetitive transient testing,

where the Skeleton cell was able to cycle at higher rates than the other cells and produced less heat in the process.

Chapter 3: Voltage Transient Suppression

Voltage Transient Experimental Setup

The experimental setup is similar to the one used in 2015 with the only difference being the type of battery that is utilized. In 2015, a 10S/1P battery made up of 30 Ah cells was used. In the work performed here, the battery module, shown in Figure 53, consists of a 10S/1P array of 20 Ah LFP, lithium iron phosphate, cells contained within an aluminum cooling module. An ACTIA® battery management system (BMS), is also used to ensure that the cells are balanced. This battery module had already been constructed and therefore was used in this experiment, note that the transients produced in this study are representative of transients induced by any electrochemical energy storage module with the same OCP.

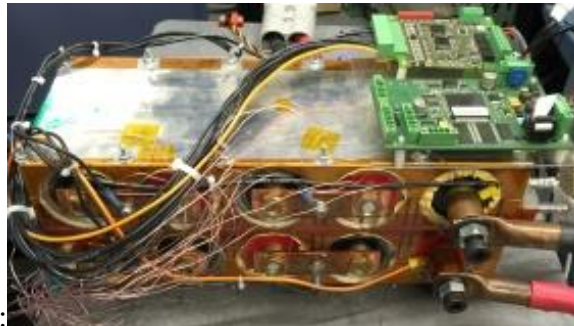


Figure 53: The battery module in a 10S/1P configuration with BMS board attached.

The cells have a nominal voltage of 3.3 V, a max voltage of 3.8 V, and an approximate ESR of 1.3 m Ω . They have a rated peak continuous current as high as 500 A and are recommended not to exceed a temperature of 65°C. In this configuration, the nominal pack voltage is approximately 33 V and should not exceed 38 V. The transient profile is generated by a NI-USB-6211 multifunction

IO device that supplies analog signals to a Chroma model 63209 programmable load and two Chroma model 62050P power supplies, all of which can be seen below in Figure 54.

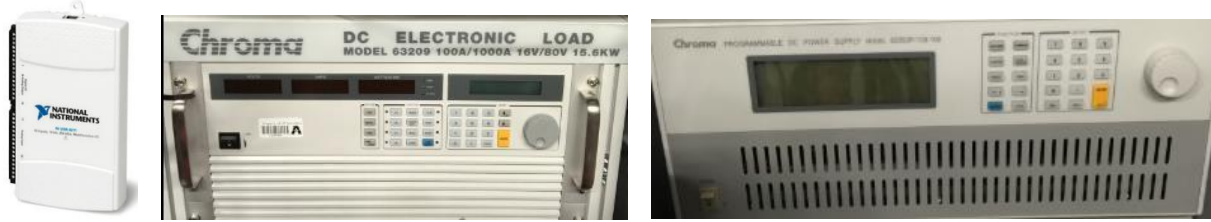


Figure 54: The NI-USB-6211 multifunction IO device used to control the load and supplies (left) the Chroma load used for discharge current (middle) one of the two Chroma supplies used for the charge current (right).

The Chroma load is used in the available 1000A/80V/15.6kW range. The Chroma power supplies used are configured in a master-slave setup and are each capable of 100V/100A/5kW. The current profile used to induce the voltage transients is very similar to the profile of interest used in the 2015 experiment, with the only difference being that the charge current is limited to 180 A. The supplies and load are connected to a common copper bus block, which is also connected to the battery module using 3/0 gauge welding cable. These cables introduce inductance to the system based off of the cable's length and diameter. The formula for calculating the inductance can be see below in equation 6.

$$L = 2l \left(\ln \left(\left(\frac{2l}{d} \right) \left(1 + \sqrt{1 + \left(\frac{d}{2l} \right)^2} \right) \right) - \sqrt{1 + \left(\frac{d}{2l} \right)^2} + \frac{\mu}{4} + \left(\frac{d}{2l} \right) \right) (H) \quad (6)$$

Using equation 6, the inductance can be calculated for a certain length of cable assuming the diameter of 3/0 gauge cable as 0.582 inches. This experiment expresses interest in how a change in inductance affects the transients induced and the effectiveness of the different suppression techniques. With that, two different lengths of cable have been used and data has been collected from each. Prior to experimentation, models were developed and run using LTSpice. TVS models

are supplied by the manufacturers and then imported into the model. Unfortunately, the manufacturer did not have models for the MOVs procured for this study. The battery module is modeled as a very large capacitor with a designated initial voltage and a series resistance. The capacitance of the module is estimated at roughly 50,000 F and the series resistance of the battery and the cables is approximately 38 m Ω . As previously mentioned, the cables introduce inductance to the system and therefore will be modeled using a non-ideal inductor. The two cable lengths used are 465 cm and 584 cm. Using equation 6 and the cable dimensions, the approximate inductance introduced by these cables is 6.8 μ H and 8.82 μ H, respectively. In order to induce a voltage transient in the model, a MOSFET is used along with a transient voltage source that will act as a switch in the circuit, simulating the fast changes in current in the profile of interest. The simulation is run for 50 ms and the initial condition of the battery is set at 33 V, the nominal voltage of the module. The model is shown in Figure 55, along with a photograph of the experimental setup. The rise time and fall time on the voltage source are set to closely match that of the supplies and load. The schematic is the same for both lengths of cable with only the inductance value changing. The voltage source driving the FET will first turn on at 10 ms and then off at 30 ms, which is where we expect to see the voltage transients. Based on equation 1, we are to expect a larger transient when the longer cables are used, due to a larger inductance. The transient voltages obtained from simulation are shown in Figure 56 for each respective cable length. As shown, the 465 cm cable should produce a roughly 56 V transient while the 584 cm long cable is expected to produce transients of nearly 64 V. Both cables produce transients that are within the load's voltage range to prevent any possible damage.

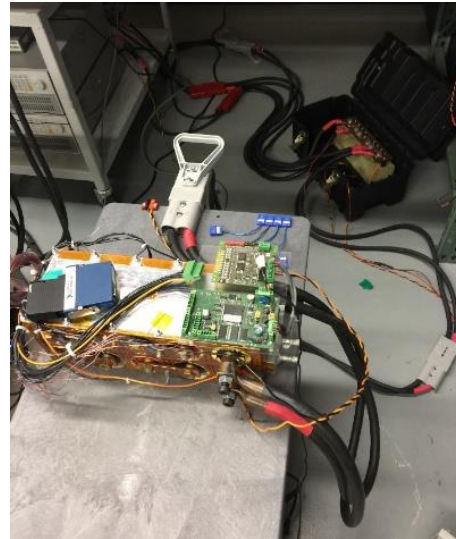
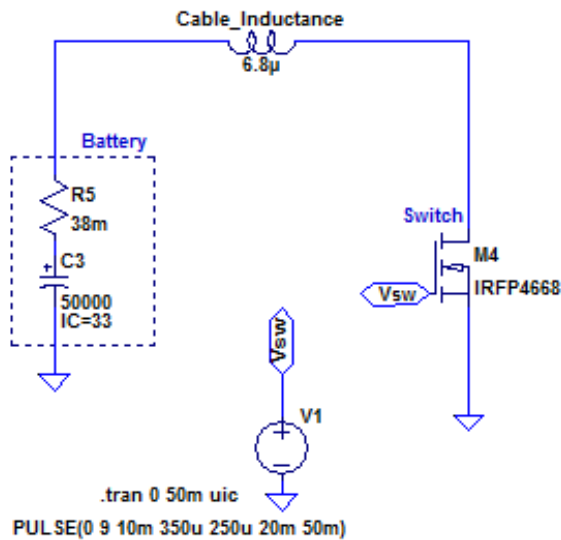


Figure 55: The schematic of the experimental setup (left) a photograph of the experimental setup used to produce voltage transients (right).

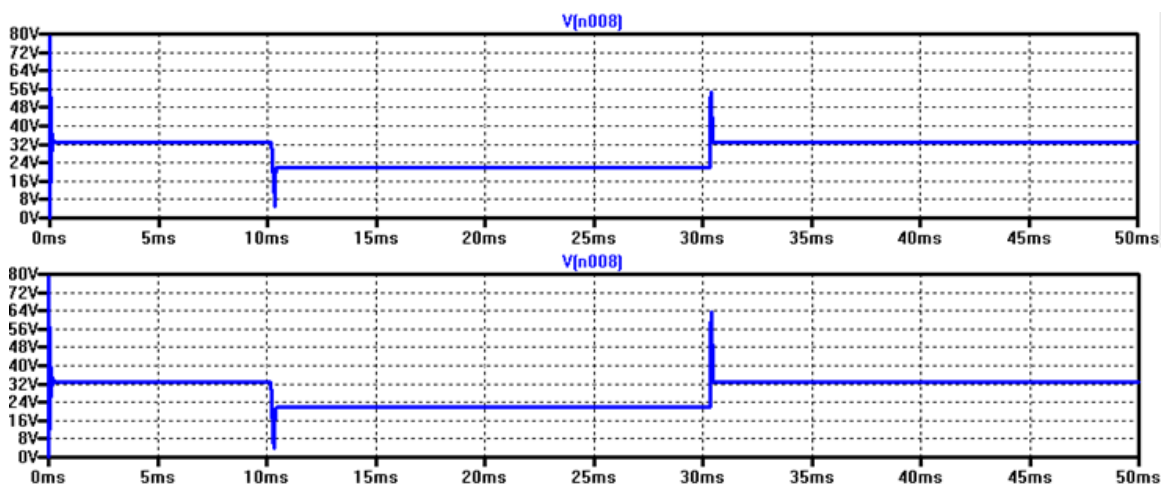


Figure 56: Output from the system modeling the use of the shorter cables with an inductance of $6.8 \mu\text{H}$ (top) and $8.82 \mu\text{H}$ cables (below).

Voltage Transient Suppression Results

Unprotected Transient Results

The programmable load and supplies are controlled by the NI-USB-6211 multifunction IO device, which controls output voltages using a LabVIEW program. Together, the LabVIEW program and the NI device deliver analog signals to the load and supplies corresponding to the desired command. During this study, each of the two cable lengths were evaluated three times for

repeatability. Figure 57 shows an overlaying plot of the transient voltages recorded for both lengths of cable, along with the corresponding current profile.

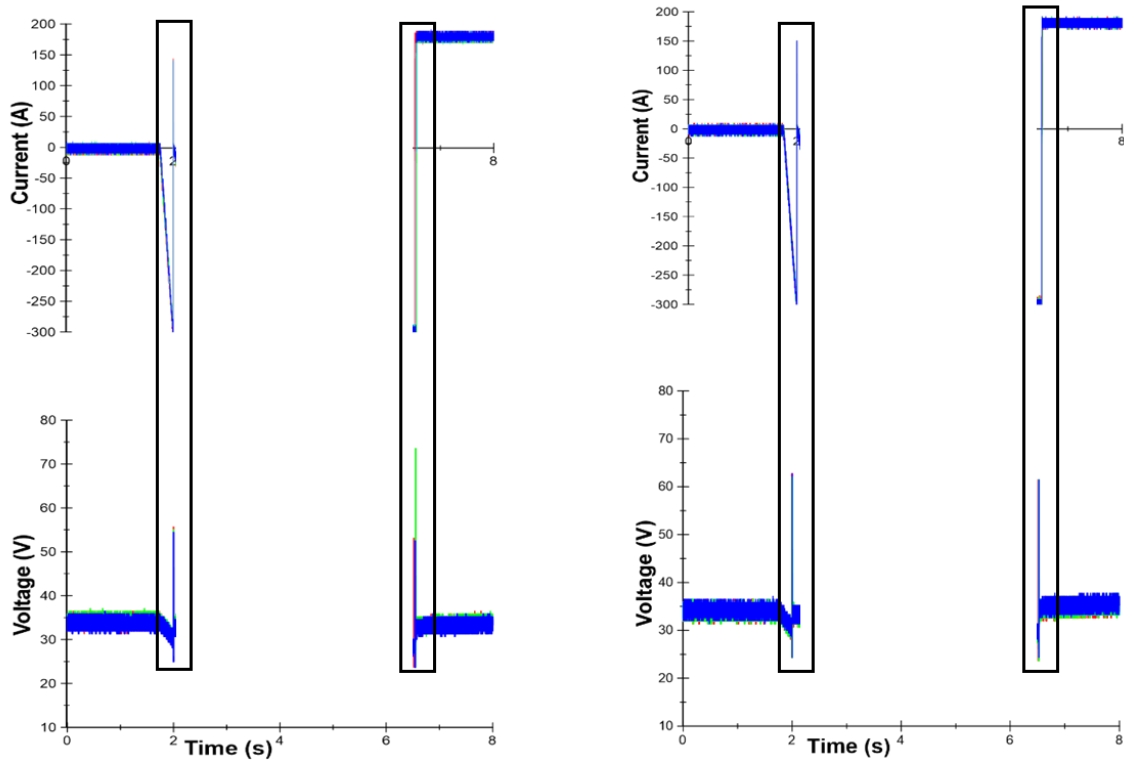


Figure 57: Current (above) and voltage (below) profiles for 465 cm cable (left) and 584 cm cable (right) respectively.


Figure 57 illustrates how the transients align with the abrupt changes in the current profile for each length of cable. The simulation results are also verified as the transient voltages obtained experimentally closely match the simulation values obtained in Figure 56. Once the simulations were experimentally proven to be accurate, the objective was to begin to evaluate the ability of the suppression topologies to suppress transients.

TVS Protected Transient Results

The TVS diodes that were evaluated were procured from Littelfuse, who offers a wide selection of devices across a range of different voltage and power levels. As mentioned earlier, Littelfuse provides SPICE models on their website and were used in evaluating the simulation model. Based

off of the battery modules voltage, two TVS diodes were chosen to be evaluated in this study. One was sized for the modules nominal voltage and the other was chosen assuming the module was operated fully charged. Those are the 15KPA33CA and the 15KPA40CA, respectively. The electrical characteristic for the two TVS diodes are listed in Table 6 below.

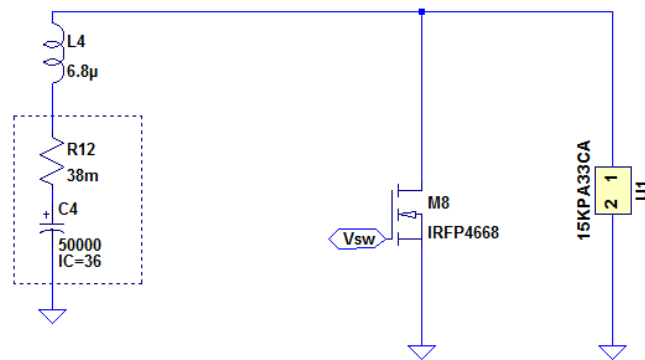
Table 6: The characteristics of the two tested TVS diodes, the 15KPA33CA and the 15KPA40CA.

Electrical Characteristics ($T_A=25^\circ\text{C}$ unless otherwise noted)									
Part Number (Uni)	Part Number (Bi)	Reverse Stand off Voltage V_R (Volts)	Breakdown Voltage V_{BR} (Volts) @ I_T		Test Current I_T (mA)	Maximum Peak Pulse Current I_{PP} (A)	Maximum Reverse Leakage $I_R @ V_R$ (μA)	Maximum Clamping Voltage $V_C @ I_{PP}$ (V)	Agency Approval 
			MIN	MAX					
→ 15KPA33A	15KPA33CA	33	36.9	40.4	5	276.1	2	54.7	X
→ 15KPA36A	15KPA36CA	36	40.2	44.0	5	252.5	2	59.8	X
→ 15KPA40A	15KPA40CA	40	44.7	48.9	5	229.5	2	65.8	X

The two TVS diodes were chosen based on three main characteristics - reverse standoff voltage (V_R), maximum peak pulse current (I_{PP}), and maximum clamping voltage (V_C). The first characteristic, reverse standoff voltage, is important to ensure the TVS does not affect the driving voltage. Ideally V_R is chosen to be equal to the peak operating voltage of the circuit, but the 15KPA33A is chosen to examine the suppression effects if the module charged to its nominal voltage. The second characteristic, peak pulse current, defines the maximum current the TVS diode can handle without damaging the diode. Finally, the third important characteristic is the maximum clamping voltage, which defines the peak voltage across the diode when subject to I_{PP} . The power rating for both of these devices is 15 kW, which is higher than that required by the experiment but, given the repetitive nature of the expected transients, it was decided that more power capability is safer.

LTSPICE simulations of the system using the 15KPA33CA and 15KPA40CA TVS diodes are shown in Figure 58. The TVS diode under test is placed in parallel with the point of common

coupling among the system components. As shown in Figure 58A, the TVS diode limits the peak voltage to 48 V, as opposed to 56 V seen without the TVS diode in the circuit. This is where the drawback to TVS diodes starts to be seen. Ideally, the voltage should be clamped to only a few volts above the nominal operating voltage however due to the I-V curve only starting to conduct just above the desired clamp voltage, a significant voltage is allowed to build up before the diode is fully turned on. The discrete nature of the available TVS clamping voltages introduces further deviations from the desired clamp voltage. Picking one with a higher or lower clamp voltage may either allow the device to conduct even in the nominal operational range or allow a transient further over the desired clamp voltage, making it difficult to choose the appropriate device from the limited availability. The models demonstrate that TVS diodes can be used to limit transient events similar to those observed in these types of systems. This allows for the maximum transient to be sized and accommodated for within the supply, bus, and load systems, respectively.



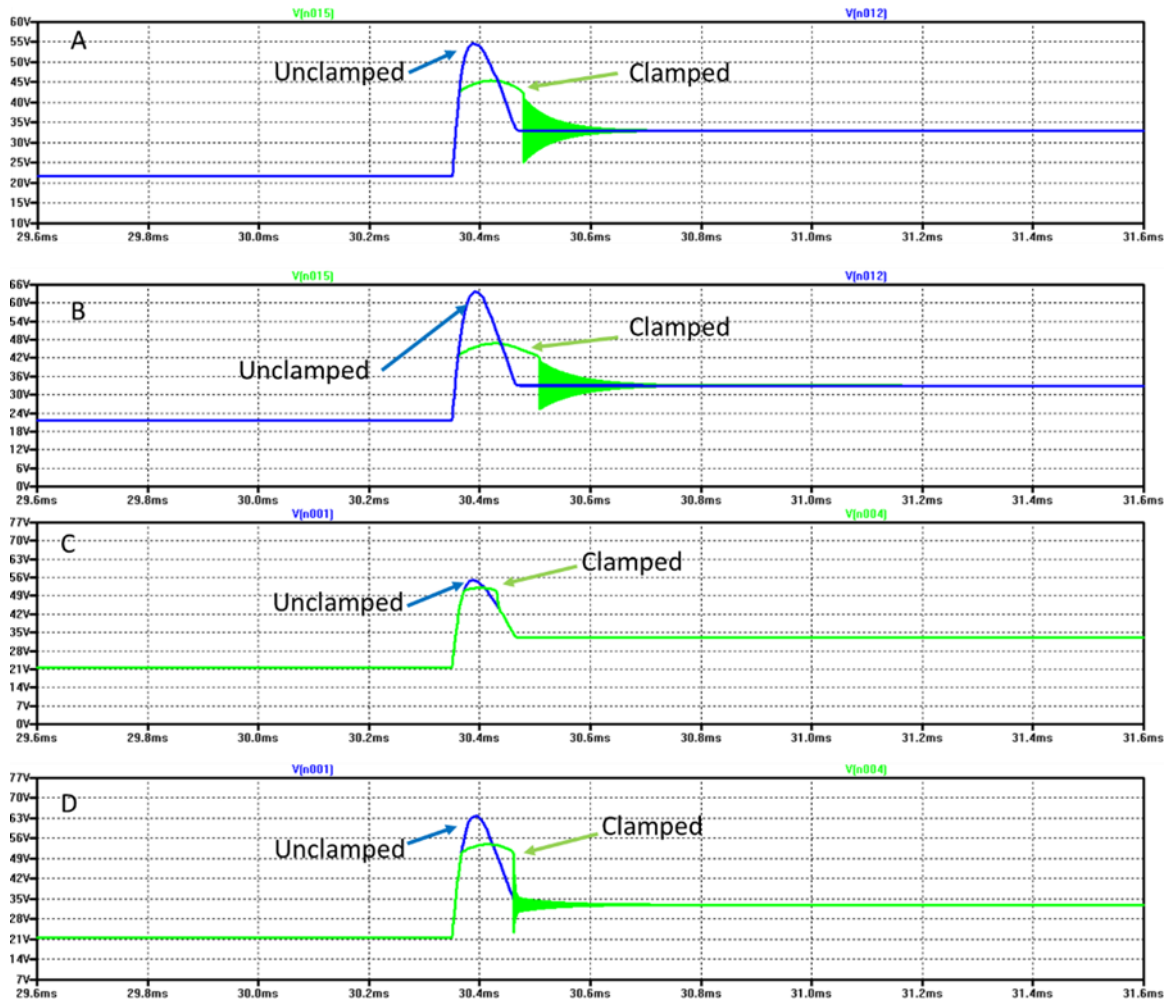


Figure 58: Simulation results of (A) 15KPA33CA using 465 cm long cable, (B) 15KPA33CA using 584 cm long cable, (C) 15KPA40CA using 465 cm long cable and (D) 15KPA40CA using 584 cm long cable.

The first TVS diode experimentally evaluated is the 15KPA33CA using the 465 cm long cable. A LeCroy WaveSurfer digital oscilloscope is used to capture the transient voltage and current profiles which are measured using LeCroy differential voltage probes and a clamp-on current meter. These diagnostics are shown integrated into the setup in Figure 59.



Figure 59: The system setup using the 15KPA33CA, differential voltage probes, and current meter.

Voltage and current waveforms measured during three experiments using the 465 cm long cable and the 15KPA33CA in place is shown in Figure 60. The transient voltage profile shows consistent transient clamping throughout all three tests at roughly 45 V, nearly 10 V less than the transients produced in the unprotected system and only 3 V less than the peak voltage the simulation suggested would be induced. The current shunted by the TVS diode is between 160 A and 175 A for the transients induced. The next step was to evaluate how well the TVS would handle repetitive operation of the current waveform with transients occurring every few seconds for an extended period of time. Prior to experimentally evaluating the repetitive operation, the energy dissipated during a single cycle was computed as shown in Figure 61, using equations 7 and 8. Knowing the energy dissipated in a single cycle, the energy dissipated in repetitive cycling could be calculated along with the expected rise in temperature.

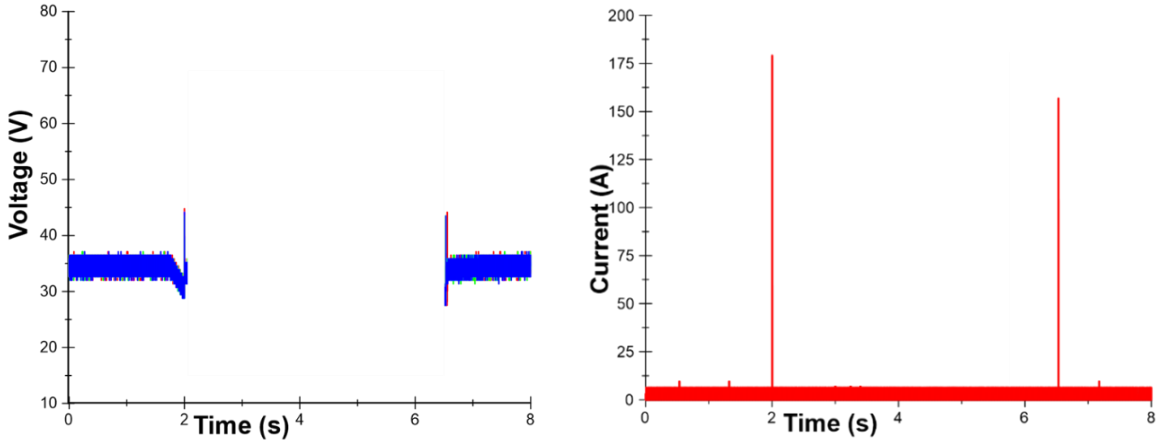


Figure 60: The transient voltage profile using the 15KPA33CA for suppression (left) the current shunted through the TVS diode (right).

$$P = V * I (W) \tag{7}$$

$$E = \int P * dt (J) \tag{8}$$

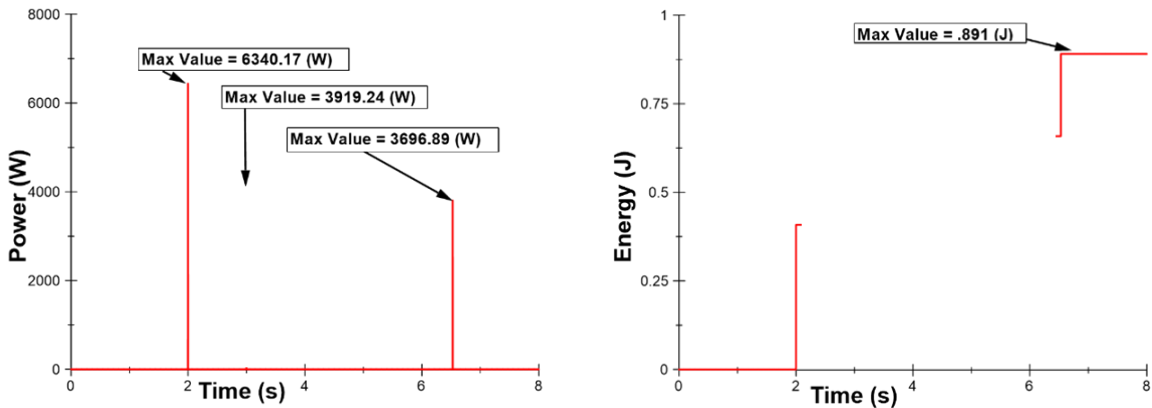


Figure 61: The power consumed by the 15KPA33CA for each voltage transient produced (left) the power consumed integrated to energy of the same profile, both calculated using the equations 7 and 8 respectively (right).

As shown in Figure 61, each full cycle only dissipates roughly 0.9 J of energy. It was assumed that a continuous run consists of 60 cycles performed repetitively over roughly 10 min. The total energy dissipated by the diode is found by multiplying 0.9 J by 60, resulting in roughly 54 J. The average power is calculated by dividing the total energy dissipated by the length of the test, 600

sec, which is roughly 90 mW. Referring back to the data sheet, the typical thermal resistance of junction to ambient is said to be 40 °C/W. If the average power is multiplied by the thermal constant then it is estimated that the TVS diode increases in temperature by about 3.5°C. Since the device is also cooled by the ambient air, it was determined that the diode would be able to sufficiently handle the repetitive test. The results of which are shown in Figure 62, where a T type thermocouple was used to validate the temperature rise of the diode. As shown the diodes temperature rises by roughly 3°C in each of the three experiments performed. The last two cycles of suppressed transients recorded during the 60 cycle test are shown graphically in Figure 63.

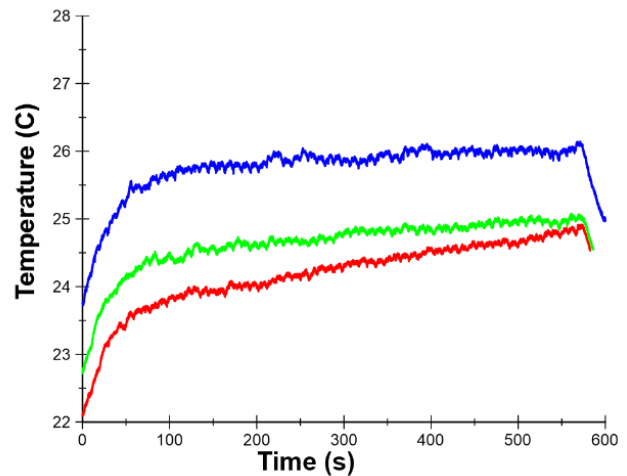
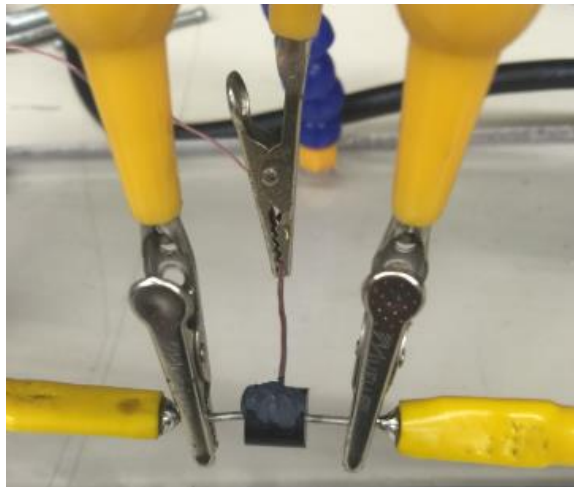


Figure 62: 15KPA33CA with a T-type thermocouple thermal epoxied to the diode for temperature measurements (left) three tests showing the temperature rise of the TVS diode during the 60 cycle tests (right).

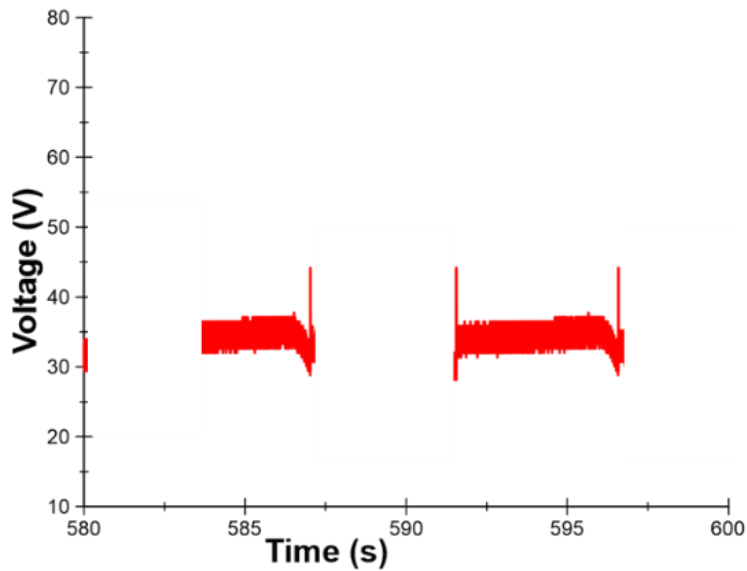


Figure 63: Transient voltage profile recorded during the last two of the 60 cycle test using the 15KPA33CA diode.

Figure 63 illustrates that the 15KPA33CA is a reliable choice for suppressing repetitive voltage transients when the module is used at its nominal voltage. As discussed earlier, TVS diodes have a very nonlinear I-V curve and while it works well at the nominal voltage, it doesn't necessarily mean it will work at the modules full 38 V charge voltage. When the TVS was used with the battery fully charged, the 15KPA33CA's resistance was low enough to significantly draw current from the battery, depleting its charge and causing it to heat up quickly, seen in Figure 64. It was still able to suppress the transients, however the steady rise in temperature shows that the TVS should not be used for an extended period of time if the battery is operated fully charged. This brings about the main limitation of TVS diodes in that it is desirable to have one that suppresses transients quickly enough but acts as an open circuit across the full desired operational range.

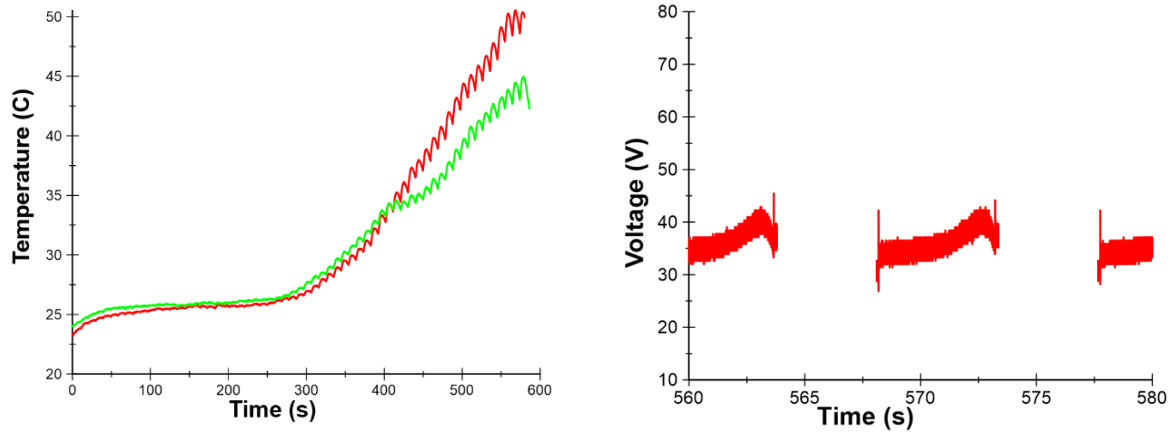


Figure 64: With the module nearly at peak charge the temperature started to increase drastically over long term use (left) the voltage suppression is identical to when the module was charged to its nominal voltage (right).

The next round of testing involved using 15KPA40CA with the 584 cm long cable. The setup is exactly the same as was previously documented with the only differences being the use of the 15KPA40CA diode in place the 15KPA33CA diode and the longer cable to induce larger transients. The voltage of the bus, including the transients recorded, during three independent experiments are shown in Figure 65 along with the current measured through the device.

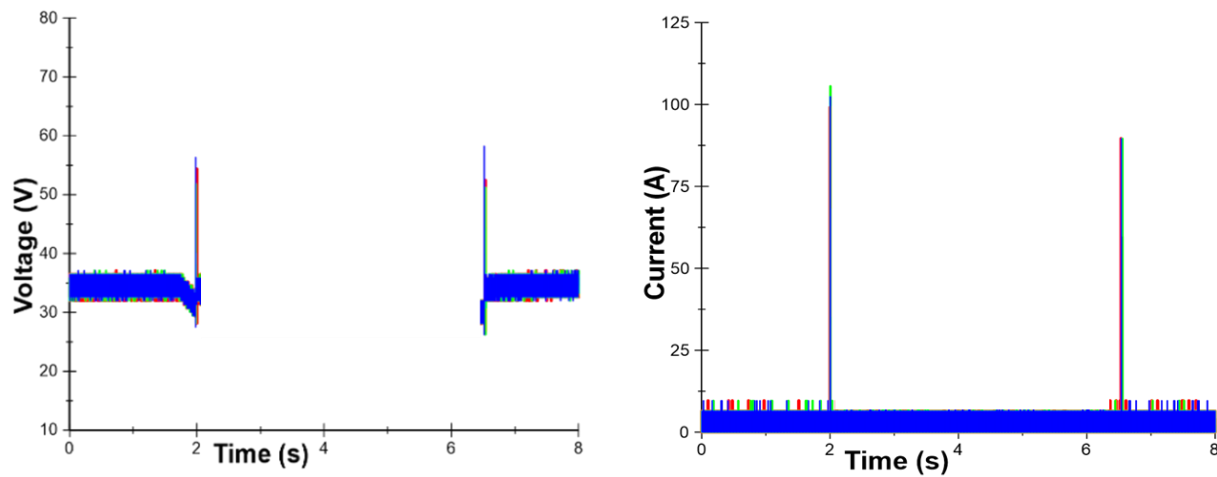


Figure 65: Transient voltage profile using the 15KPA40CA and the 584 cm cable (left) the current shunted by the 15KPA40CA (right).

The 15KPA40CA was able to limit the voltage transients to roughly 55 V which is slightly higher than the transients suppressed by the 15KPA33CA, as expected. This further demonstrates the tradeoffs of TVS diodes. Choosing one that is better matched for the desired operational voltage range comes at the cost of allowing transients to reach a slightly higher voltage. Since both diodes have roughly the same thermal constant, it is expected that they would heat up similarly when put through the same 60 cycle repetitive experiment. A photograph of the diode and a plot containing its temperature during three identical 60 cycle tests can be seen in Figure 66. Figure 67 plots the diode's voltage and current profiles measured during two identical experiments. As shown there is a slight variation in the clamped transient voltage but each transient is approximately 54 V.

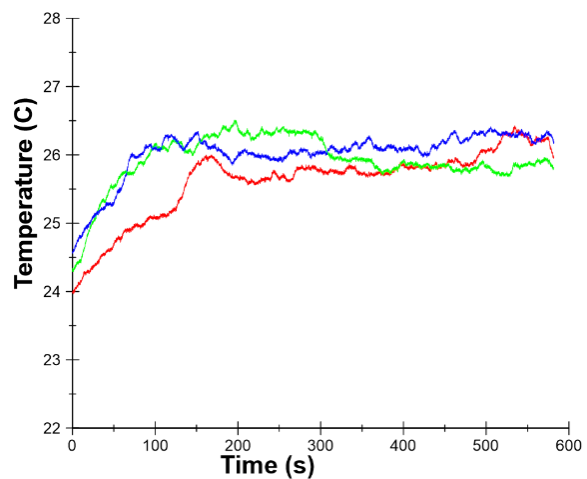
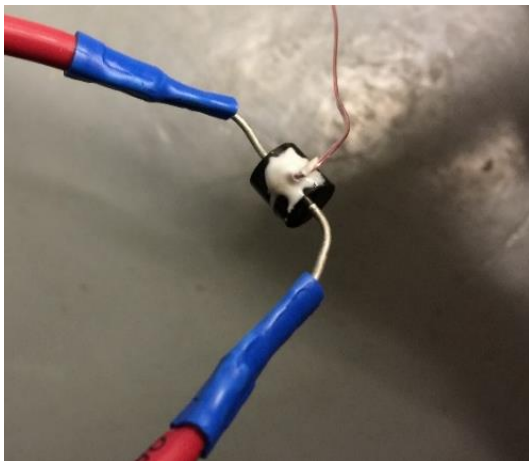


Figure 66: The 15KPA40CA with a T-type thermocouple thermal epoxied to the diode for temperature measurements (left) three tests showing the temperature rise of the TVS diode during the 60 cycle tests (right).

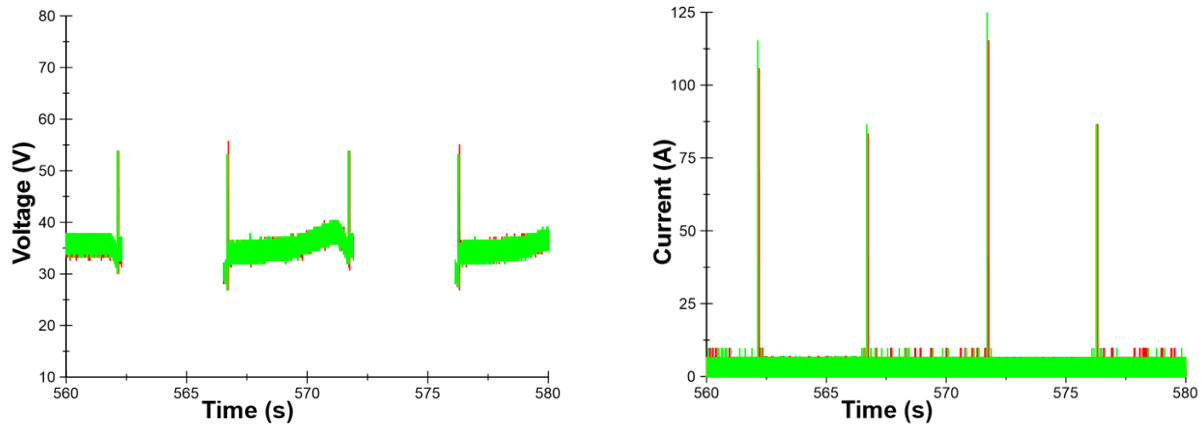


Figure 67: Transient voltages recorded (left) and current recorded through the 15KPA40CA diode (right) during the last few cycles of a repetitive experiment using two identical diodes in two different experiments to demonstrate consistency of the TVS diode.

MOV Protected Transient Results

The next transient suppression device studied was MOVs. Table 7 displays the datasheet properties of a few MOVs of interest as taken from the Littelfuse website. Like TVS diodes, MOVs are offered in discrete increments of operational and clamping voltages. Through consultation with Littelfuse, an MOV that has a maximum continuous voltage that is 20% higher than the modules voltage is preferred. In the case of the 33 V module, the V20E35P appears to be the best choice. The other two MOVs shown in Table 2, the V07E30P and V10E23P, were also evaluated based off the full battery module voltage range and because simulation models of them were unavailable from Littelfuse.

Table 7: The electrical characteristics for the MOVs used in this experiment, the V10E23P, V07E30P, and V20E35P.

Epoxy Coated Models		Phenolic Coated Models ²		Size Disc Dia. (mm)	Max Continuous Voltage		Varistor Voltage at 1mA			Maximum Clamping Voltage		Max Peak Current (8 x 20µs 1 pulse)	Energy Rating (2ms, 1 pulse)	Typical Capacitance f = 1MHz
Part Number (Base part)	Branding	Part Number (Base part)	Branding		V _{MACRMS}	V _{MDCI}	V _{NOM Min}	V _{NOM Nom}	V _{NOM Max}	V _C	I _{PK}			
					(V)	(V)	(V)	(V)	(V)	(V)	(A)			
V10E23P	P10E23	V10P23P	P10P23	10	23	28	32.4	36.0	39.6	71	5	2000	12	3200
V07E30P	P7E30	V07P30P	P7P30	7	30	38	42.3	47.0	51.7	93	2.5	1000	7	1350
V20E35P	P20E35	V20P35P	P20P35	20	35	45	50.4	56.0	61.6	110	20	8000	115	10500

MOVs have three main characteristics that were considered when examining their specifications. These include the maximum continuous voltage ($V_{M(DC)}$), max clamping current (I_{PK}), and the maximum clamping voltage (V_C). Disk size is also a factor as larger disk sizes come with an increased single transient event current I_{TM} and energy dissipation W_{TM} capability, respectively. Of those shown in Table 2, the lowest I_{TM} is 1000 A and the lowest W_{TM} is roughly 7 J, both of which are well above the ratings needed for transients induced in this experiment.

The MOVs were then tested in the same fashion as the TVS diodes were. Each of the three MOVs were tested using both the 465 cm and 584 cm long cables, respectively. Figure 68 contains photographs of the three of the MOVs evaluated.



Figure 68: The V10E23P placed parallel to the bus with the differential voltage probes and the clamped-on current meter (left) the V07E30P with the same exact set up (middle) the V20E35P also with the same exact set up (right).

The first MOV evaluated was the V10E23P, whose 1 mA conduction current occurs when a voltage between 32.4 V and 39.6 V is applied. Its maximum clamping voltage is roughly 71 V, which is relatively high relative to many of the transients seen here. Keep in mind that the 15KPA33CA TVS diode’s maximum clamping voltage is listed at roughly 55 V. Figure 69 presents voltage and current data recorded during three independent experiments using the 465 cm long cable. Referring back to Figure 57, in which a plot of the voltages recorded with no current suppression applied, it should be noticed that the V10E23P appears to have little effect suppressing transient lower than 55 V. It does, however, suppress the few higher voltage transients seen in the unprotected voltage profile. This data suggests that the V10E23P is not effective solution for clamping the transients observed here. The data collected from the 584 cm long cable using the V10E23P is shown in Figure 70 where very similar results were obtained.

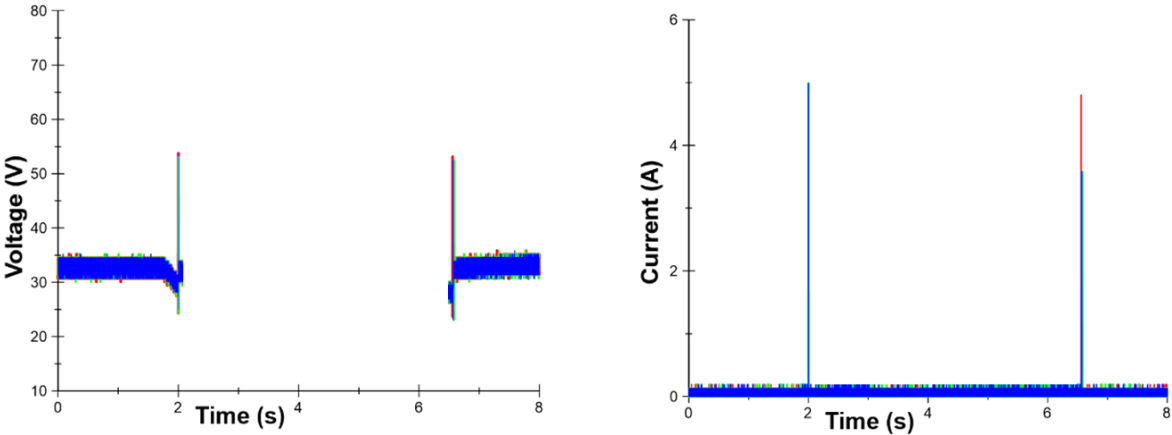


Figure 69: Transient voltage profiles measured during three tests performed using a 465 cm cable and a V10E23P MOV. Voltage (left) and MOV current (right) are shown.

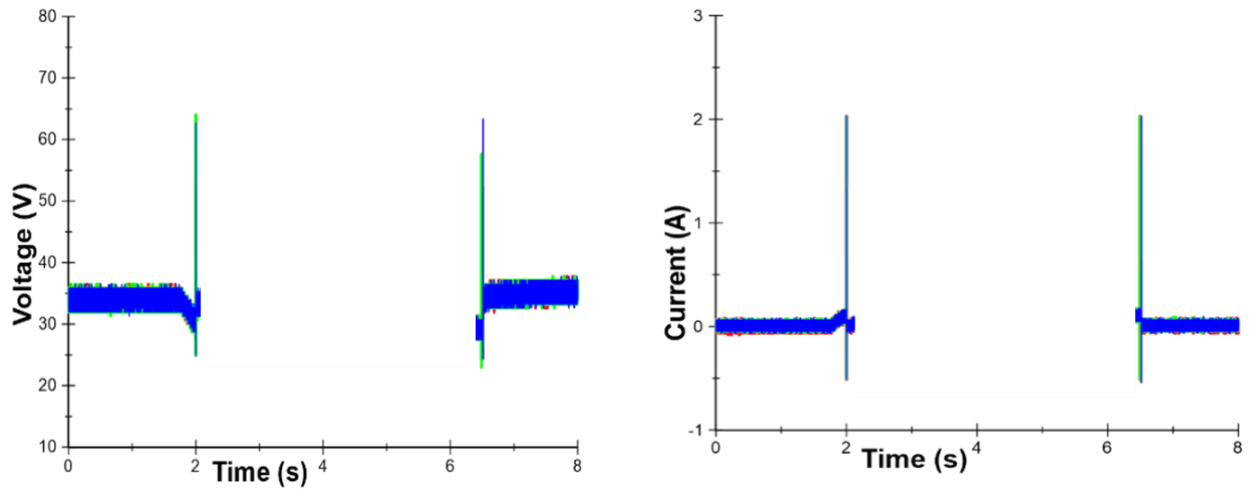


Figure 70: Transient voltage profiles measured during three tests performed using a 584 cm cable and a V10E23P MOV. Voltage (left) and MOV current (right) are shown.

From these results, it is clear that better suppression should be obtained if an MOV with lower operational and maximum clamping voltage ratings is utilized. From Table 2, the other two devices listed, V07E30P and the V20E35P, each have higher nominal operating voltage and clamping voltage ratings than the V10E23P and are likely to be less effective. This hypothesis was confirmed with the data presented in Figures 71 through 74.

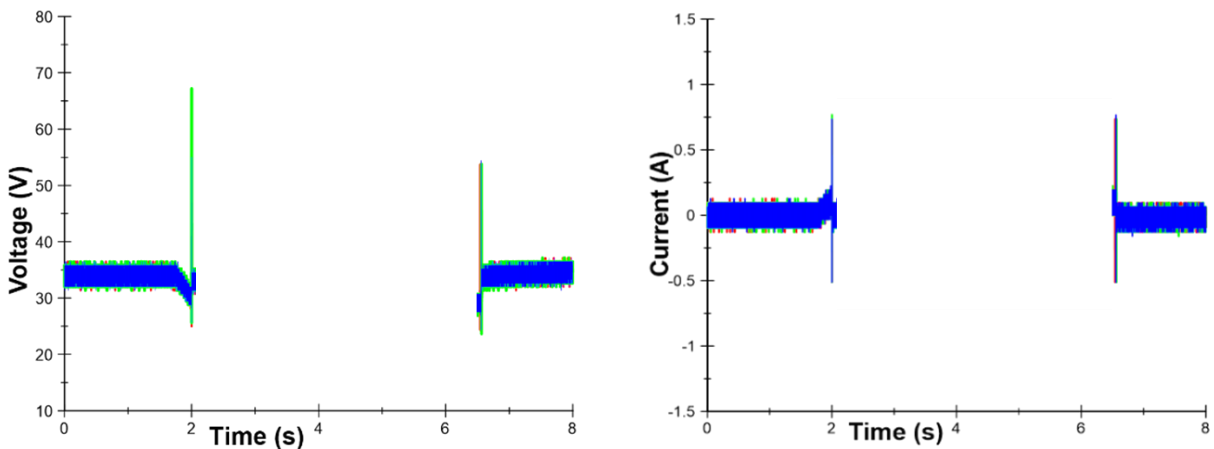


Figure 71: Transient voltage profiles measured during three tests performed using a 465 cm cable and a V07E30P MOV. Voltage (left) and MOV current (right) are shown.

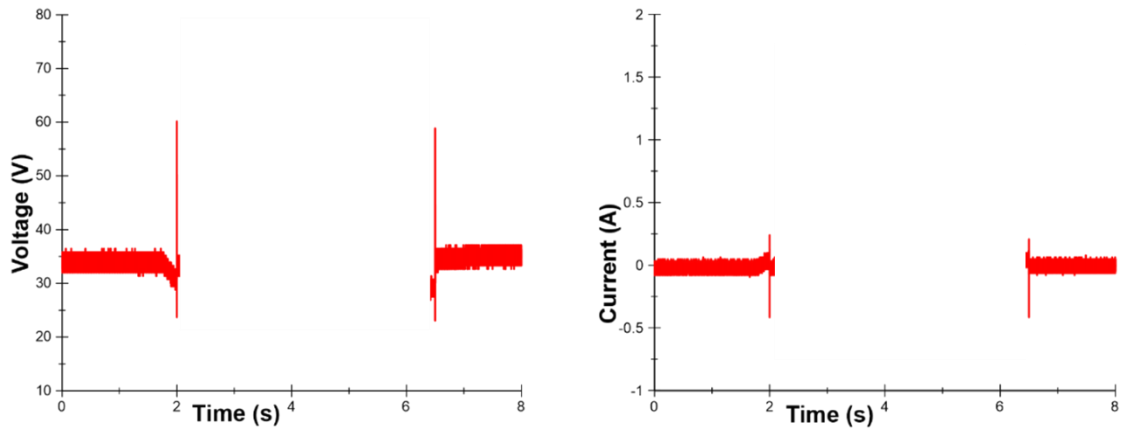


Figure 72: Transient voltage profiles measured during three tests performed using a 584 cm cable and a V07E30P MOV. Voltage (left) and MOV current (right) are shown.

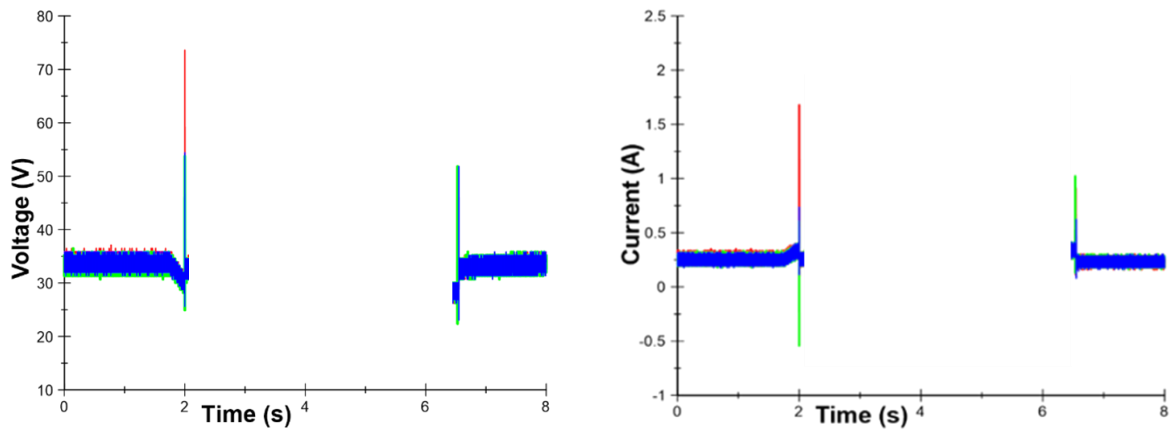


Figure 73: Transient voltage profiles measured during three tests performed using a 465 cm cable and a V20E35P MOV. Voltage (left) and MOV current (right) are shown.

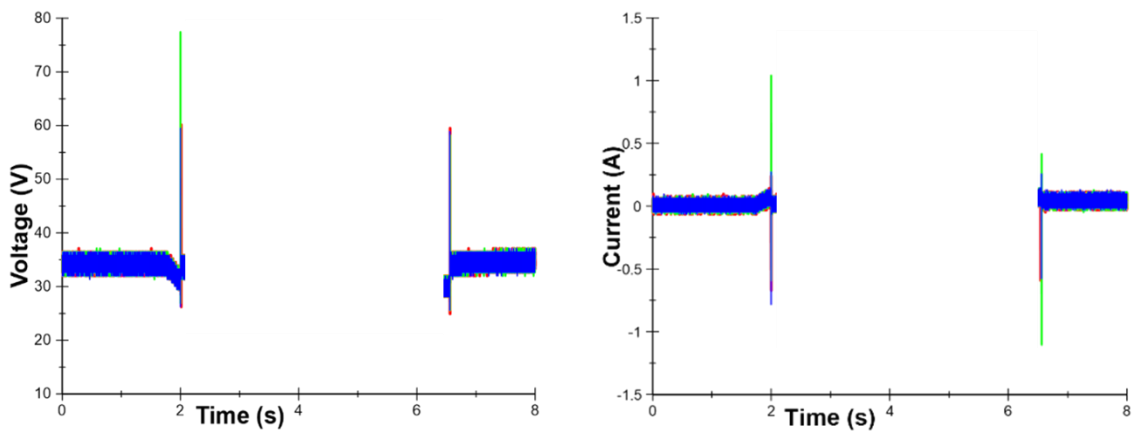


Figure 74: Transient voltage profiles measured during three tests performed using a 584 cm cable and a V20E35P MOV. Voltage (left) and MOV current (right) are shown.

The V10E23P was evaluated in the same repetitive manner as the TVS diodes to validate its repetitive effectiveness as well as its thermal response. A T-type thermocouple was affixed to the MOV using thermal epoxy and then it was subjected to the current profile of interest 60 consecutive times. A photograph of the epoxied thermocouple on the MOV along with a plot of the MOV's temperature during the experiment is shown in Figure 75. The voltage and current data recorded during the last few cycles is shown in Figure 76 when the 465 cm long cable was used. As shown in Figure 32, the MOV did not effectively suppress any of the transients except the higher ~75 V transients occasionally seen. As expected, the MOV's temperature rises only slightly due to the lack of current conducted through it.

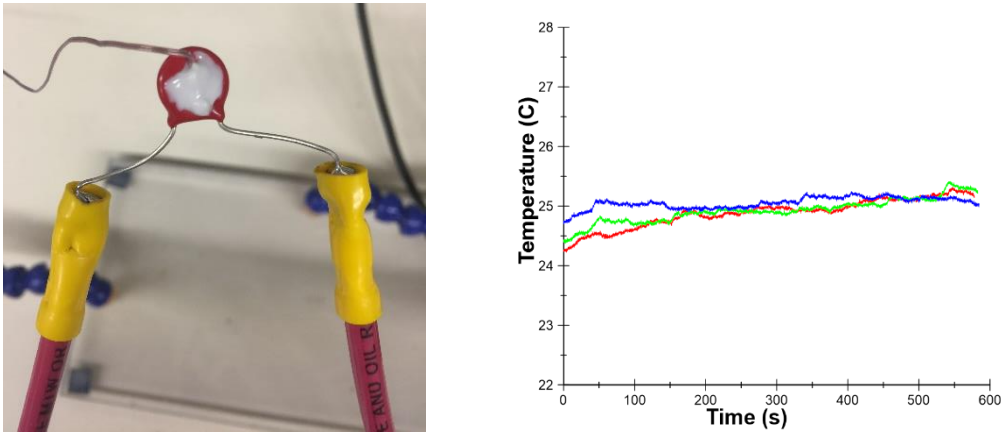


Figure 75: V10E23P with a T-type thermocouple attached using thermal epoxy for temperature measurements during the 60 cycle test (left) three temperature measurements of the V10E23P while clamping voltage transients during the 60 cycle tests (right).

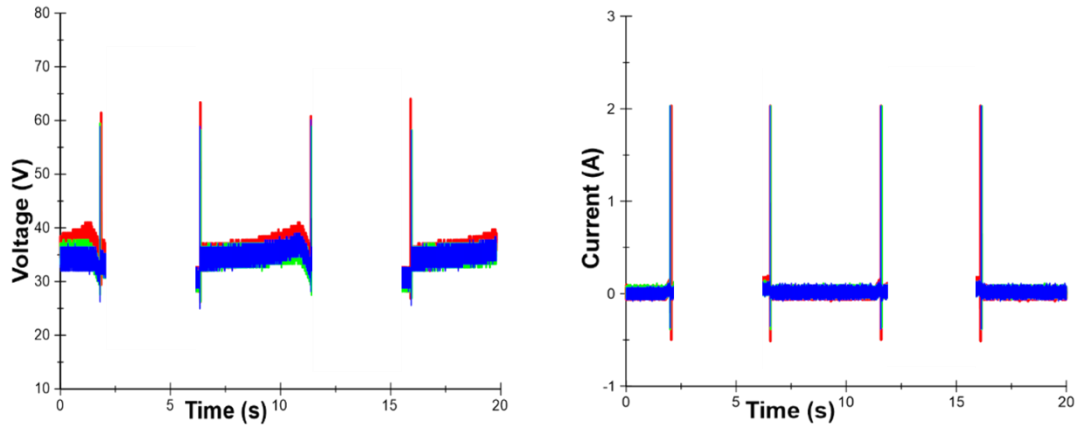


Figure 76: Transient voltage profiles of the last two cycles during the 60 cycle test (left) current shunted by the V10E23P corresponding to the transient voltage profiles (right).

From the experiments conducted it is likely that MOVs are not as effective in this application of suppressing transients. Similar to TVS diodes, the MOVs only come in discrete voltage increments and the maximum clamping voltage is significantly higher than the nominal operational voltage range meaning that the voltage transients have to be quite significant in order to actually be suppressed.

Active Circuit Protection Results

As mentioned previously, TVS diodes and MOVs each suffer from discrete voltage ranges they operate in. One possible solution to overcoming these limitations is to use actively controlled electronics to more accurately control the clamping voltage. Two different designs were conceived, simulated, and evaluated with mixed results. The first design is shown in Figure 77. The intent of the circuit is to redirect the transient energy through a shunt resistor (R7) when the bus voltage exceeds 39 V. The Zener diode (D7) is intended to enter reverse breakdown when 39 V is applied. Once the transient reaches a voltage higher than 39 V, the gate-to-source voltage (V_{GS}), or the voltage across the pull-up resistor (R10), of the P-channel MOSFET is negative, with respect to the bus voltage, causing it to start conducting. The Zener diode (D8) is specified to enter

reverse breakdown at 27 V. The voltage across the pull-down resistor (R9) is then $V_{\text{TRAN}} - 27$ V then allowing the N-channel MOSFET (M5) to start conducting. R11 limits the current into the N-channel MOSFET. Once the N-channel MOSFET begins conducting, the transient voltage is applied across the low impedance power resistor (R7) intended to shunt away the stored inductive energy. Figure 78 presents simulation results in which the transients are well suppressed at just over 39 V. Figure 79 contains two photographs of the actual circuit evaluated on the experimental setup. The first is a close-up of the device soldered on a protoboard and the second shows the PCB layout that was designed of the same circuit. Because there was concern that a MOSFET could fail and shunt the battery to ground through the low impedance power resistor permanently, a fuse as well as an electromechanical relay were placed in series with the power resistor as an extra precaution. Figure 80 contains the results recorded from the oscilloscope during the initial round of experimentation with this active design.

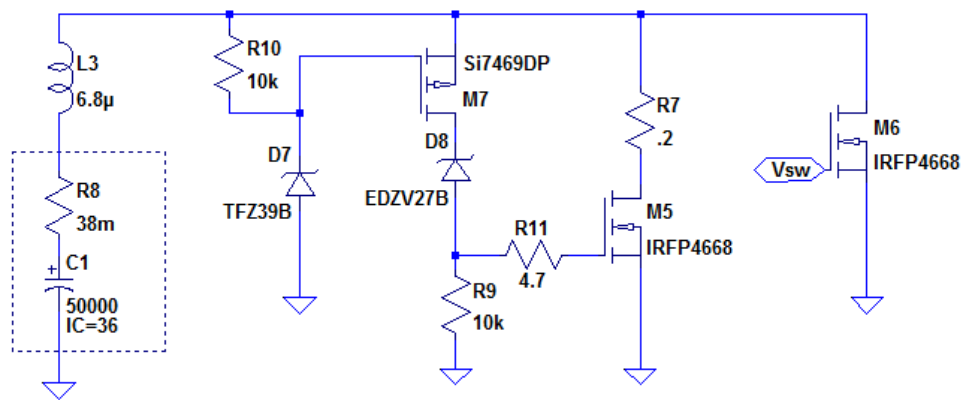


Figure 77: Circuit diagram of one active voltage transient suppression topology.

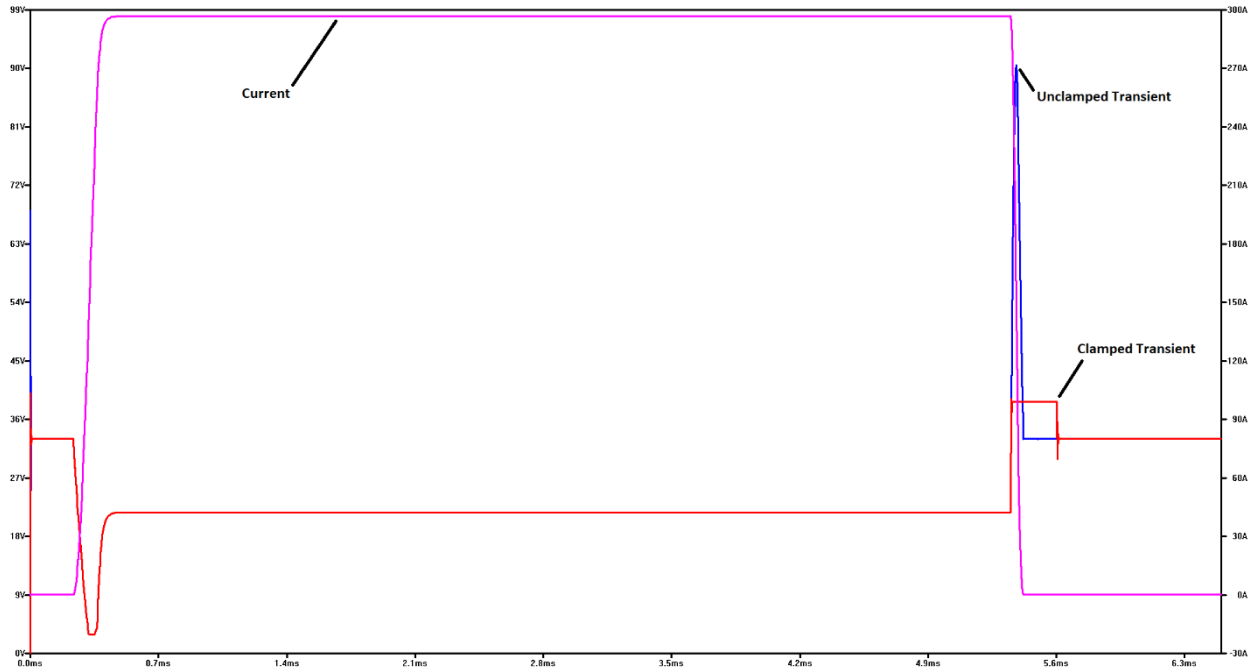


Figure 78: LTSPICE simulation results obtained from the active circuit topology shown in Figure 30.

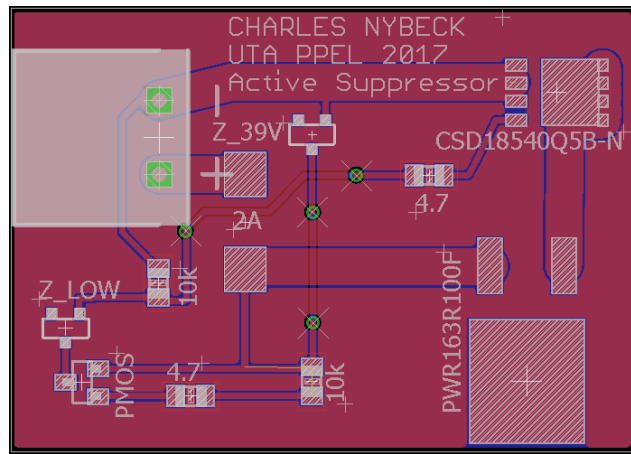
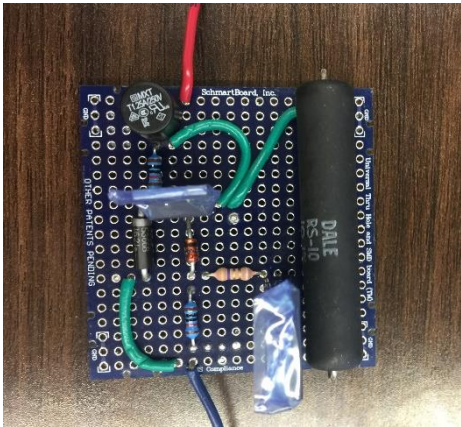


Figure 79: Active voltage transient suppression device designed to mitigate voltage spikes. Photos of the protoboard circuit (left) and the PCB layout of the same circuit (right) are shown.

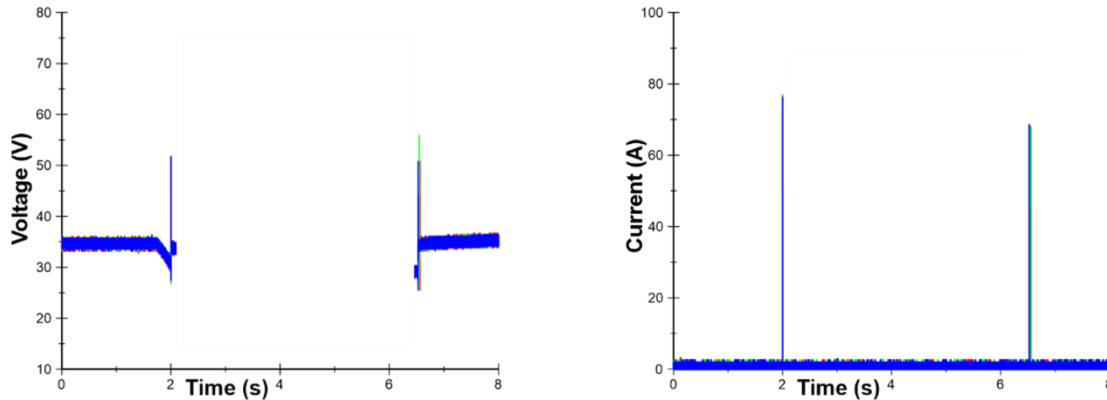


Figure 80: Voltage (left) and power resistor current (right) waveforms recorded from three experiments performed using the active suppression circuit shown in Figure 31.

Despite being designed to turn on at 39 V, the active transient suppression device appears to have clamped the voltage consistently at just over 50 V when the 584 cm long cable was used. Keep in mind, Figure 57 shows that the unsuppressed voltage transients range anywhere from just over 60 V to nearly 80 V. The current shunted by the device is between 75 A and 80 A. The reason the clamping voltage is not as low as in the simulation is thought to be that the turn on time of the MOSFETs is slow since there is no high current driver utilized in the circuit. This was done so as to minimize any additional power supplies needed to operate the circuit. Attempts at using a resistance less than 0.2 Ω were made but each time the device conducted too much current and often times the MOSFET would also fail due to both heat and transient voltages induced when the device turned off.

A schematic of the second design conceived is shown in Figure 81. This design utilizes a voltage comparator circuit to detect a transient event. The use of the comparator and a tunable reference voltage allows the turn-on voltage to be manually adjusted by the operator. When the bus voltage goes higher than the reference voltage, the comparator (U1) goes high, supplying current to the gate three MOSFETs connected in parallel. A 0.1 Ω shunt resistor is connected in series with the three MOSFETs to suppress the transient energy. Three MOSFETs are used to

distribute the transient energy and prevent them from overheating. Due to the driver opening and closing the gate so quick, new transients are formed within the circuit each time the suppression begins that causes the circuit to oscillate. An RC circuit was then utilized at the output of the driver circuit that limits the turn on and turn off of the MOSFET switches to prevent transients from occurring. A photograph of the snubber circuit with the RC timer added to the driver output is shown in Figure 82.

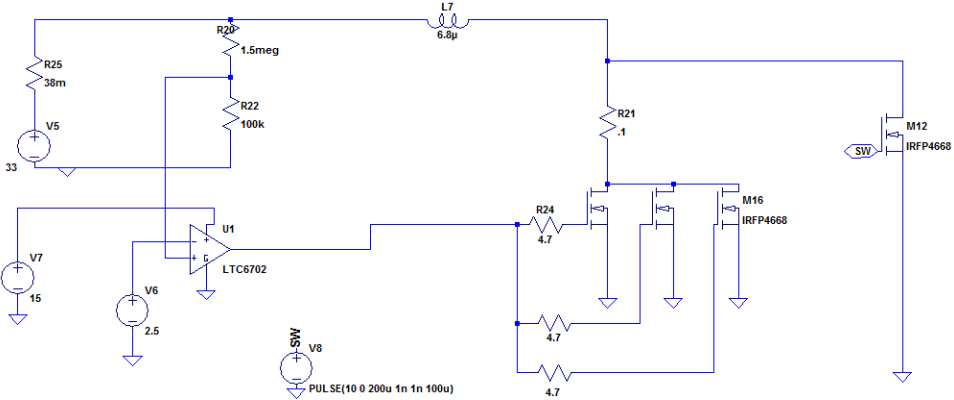


Figure 81: Schematic of the active transient suppression design using logic for a variable clamping voltage.

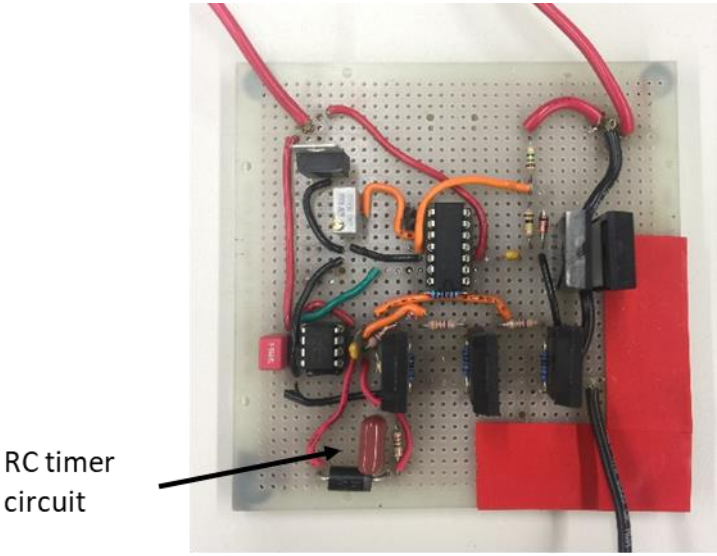


Figure 82: Photograph of the active transient suppression design shown in Figure 81 constructed on a protoboard.

The design benefited greatly with the additional MOSFETs and the comparator circuit allowing the clamping voltage to be adjustable. This design could be used to clamp transient voltage spike for modules of different OCPs by simply adjusting the reference voltage. The results of the three tests are shown in Figure 83 containing the clamped voltage and current profiles using the 584 cm long cables. The reference voltage was set so that the voltage would be clamped at 40 V. Although the voltage transient was suppressed it still managed to reach 45 V, which is nearly half of the voltage spike witnessed without protection and 5 V lower than with the first active design.

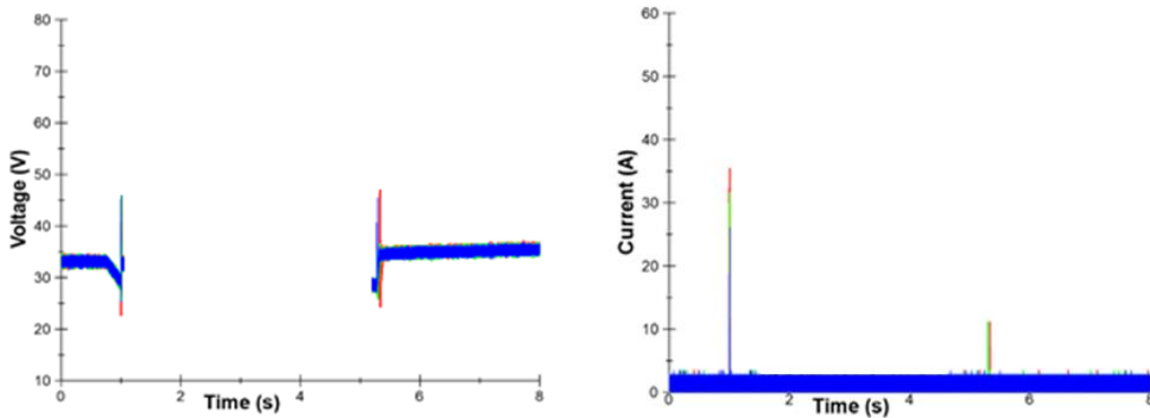


Figure 83: Voltage (left) and power resistor current (right) waveforms recorded from three experiments performed using the revised active suppression circuit.

Conclusion

It is clear from the data shown here that voltage transients should be of concern when electrochemical energy storage devices are used to supply high rate intermittent currents to transient loads in stationary and mobile microgrids. The fast switching of the current and the large inductances present in long cable networks could induce significant voltage transients with quite a bit of energy that must be shunted away. If not shunted away, the voltages could be large enough to quickly damage other components within the electrical system, including the battery itself. Three different suppression techniques have been studied here, including TVS diodes, MOVs, and

active electronic topologies. It was shown that TVS diodes and MOVs can be effective at shunting away voltage transients, however they are offered in discrete voltage ranges that do not always line up with the voltages that need to be continuously applied and transients that need to be shunted. Both devices have a nonlinear I-V curve with their resistance decreasing quickly above a certain point. Since the point at which the resistance decreases rapidly needs to be greater than the nominal operating voltage, the device must allow for some transient to occur which may or may not be within the allowable tolerance of the system. Active topologies are more flexible but they are most likely larger in size, may require additional external hardware to function, and are not commercially available off the shelf.

The work performed here has highlighted the concerns that high voltage transients bring to a high voltage system and the need for some sort of suppression technology. TVS diodes appear to be the most feasible solution but it is possible that either the design of the battery will need to be somewhat flexible around the voltage of TVS diodes available if there is not one readily available. Another option is closer coordination with the TVS diode manufacturer in order to design a TVS diode with the right doping levels to meet the requirements of the system. If this will not suffice the active transient suppression design will likely be the best option.

Chapter 4: Effect of Vented Electrolyte

Lithium-ion batteries similar to those used in the transient suppression experiment are being considered for use in a host of applications in stationary and mobile microgrids. In some applications, batteries with open-circuit-potentials as high as 1 kV are being considered and voltage regulators will be used to adapt the voltage to that required by the load. Electric field enhancements on the surfaces of the cells or conductors could amplify the electric field significantly and therefore dielectric breakdown under any possible scenario is something that

should be studied in detail before batteries are used at the 1 kV level. Among these scenarios is the one where the ambient air condition is flooded with vented carbonates from a failed battery. The work being discussed here is aimed at studying this condition and has been previously documented in [32].

Dielectric Breakdown Testbed

The work performed here is aimed at studying the dielectric strength of an air environment that is flooded with gas from a vented LFP battery. The experimental setup is shown graphically in Figures 84 through 87, respectively. Figure 84 presents a schematic diagram of the entire test setup and Figure 85 shows the entire setup photographically. Figures 86 and 87 each presents a different respective subsection in greater detail.

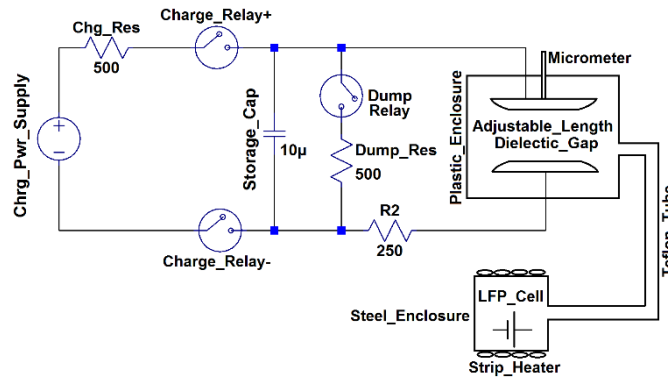


Figure 84: Schematic of the dielectric breakdown test setup.

As shown in Figures 85 and 86, respectively, a charging power supply is used to charge up a 10 μF capacitor to potentials as high as 4 kV. The capacitor acts as an intermediate energy storage device that limits the energy dissipated in an arc across the dielectric gap. Current limiting resistors are used both when charging the capacitor and to limit the current through the gap during discharge. Isolation relays are used to take the charging power supply out of the circuit prior to discharge. The charge and dump portion of the circuit is shown photographically in Figure 86. The

dielectric gap is housed within an acrylic chamber that is shown in Figure 87.

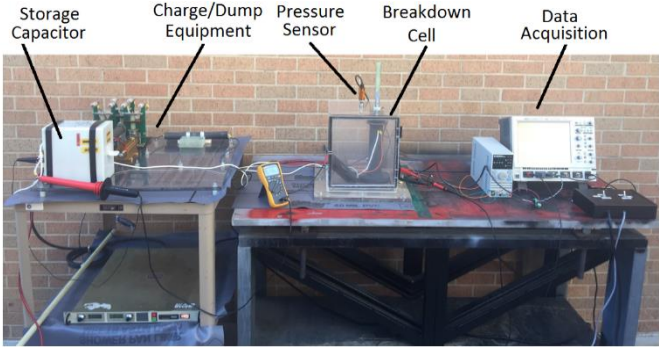


Figure 85: Photograph of the entire dielectric breakdown test setup.

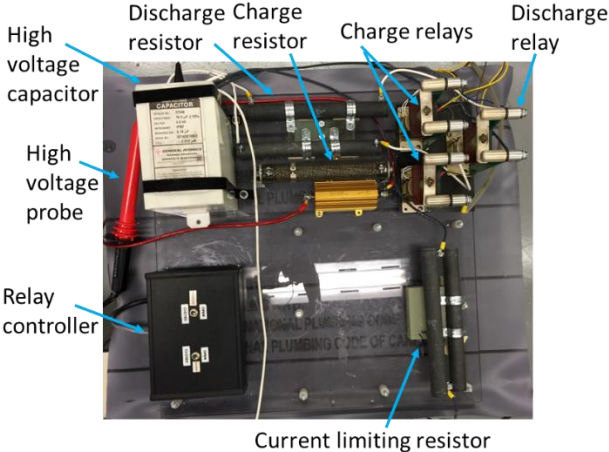


Figure 86: Photograph of the UTA dielectric breakdown experimental circuit setup.

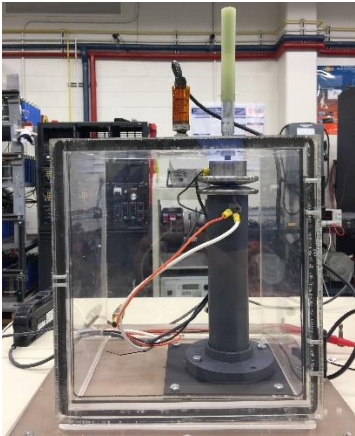


Figure 87: Sealed acrylic chamber containing electrodes used to induce voltage breakdown.

As presently configured, the chamber is not sealed to hold a constant applied pressure or vacuum. A pressure sensor is mounted on the top of the chamber for measurement of the chamber's bulk pressure during experimentation. The gap is fabricated of two 4340 steel electrodes machined with a Bruce profile [27] to ensure uniform dielectric field across the gap. The uniformity of the gap separation is ensured using Pressurex® film prior to experiments being performed. The upper electrode is mounted to a micrometer that has accuracy to ± 0.00015 in so that the gap separation can be adjusted accurately. A G-10 insulator is used to prevent human contact with the micrometer while the gap is charged up, allowing for adjustment. High temperature Teflon tubing is used to pipe gas from the vented LFP cell into the chamber. The lower electrode is fixed and mounted to a PVC stand that is affixed to the lower wall of the chamber.

Cylindrical lithium ion cells of the 26650 form factor and the LiFePO_4 chemistry are being used in the experiments documented here. Individual cells are failed in a controlled manner and the vented gas is piped into the acrylic chamber using the Teflon tubing discussed earlier. To fail the cells, they are enclosed in a 31.75 mm diameter steel tube that is capped at one end and vented to the other end using a brass barb fitting. The cell is placed within the tube and outer perimeter of the tube is wrapped with 220 VAC, 1 kW, resistive heat tape. The heat tape is used to heat up the steel and subsequently the cell within it. Once temperatures in excess of 200°C are reached, the cell's pressure cap bursts and the vented carbonates are piped out into the chamber. A photograph of the steel tube wrapped in heat tape is shown photographically in Figure 88.



Figure 88: Pipe housing, heat tape, and LiFePO₄ cell setup used to direct vented gas into the acrylic test chamber.

During an experiment, a cell is vented and the chamber is filled with vented gas. It should be noted that a small brushless DC fan, not shown in Figure 85, is placed on the lower wall of the test chamber to provide gas circulation with minimal disruption. Once gas begins to pipe in, the capacitor is charged up to the desired charge voltage and isolated from the charging supply. The gap is then adjusted closer together until breakdown occurs. Data is saved, the gap is expanded quickly, and the charge/breakdown process is repeated while the chamber is still filled with gas. Typically four to six measurements are able to be made using the gas from a single cell. Multiple cells have been vented so that a statistically relevant sample size is obtained.

While being charged, the capacitor's voltage is measured using a 40 kV Fluke high voltage probe connected to a Fluke millimeter. During a breakdown experiment, the gap voltage is measured using a LeCroy PPE4kV high voltage probe with a bandwidth of 400 MHz. The gap discharge current is measured using a LeCroy CP150 with a bandwidth of 10 MHz. Pressure is monitored using a Omega PX309 sensor that is able to measure up to 345 kPa with 0.25% accuracy. All of these measurements are collected using a LeCroy WaveSurfer oscilloscope.

Vented Electrolyte Breakdown Results

Four different sets of experiments will be reported here. In the first, the applied gap voltage was varied between 0.5 kV and 2.5 kV, with increments of 0.1 kV, in an ambient air environment and

the gap distance at which breakdown occurs with each respective applied potential was recorded. This data was collected to establish a baseline of the breakdown voltage vs pd for the experimental setup being used and for comparison against similar data published in the open literature. The data that was collected will be presented two ways, in Figures 89 and 90 respectively. In Figure 89, the breakdown voltage is plotted as a function of the gap distance at which the breakdown occurred. Error bars represent the standard deviation recorded among the five measurements recorded with each applied voltage. As shown, the data is quite repeatable with few outliers observed. Figure 90 plots the breakdown voltage as a function of pd where d is the same gap distance plotted in Figure 89. Since the pressure did not vary significantly over the experiments performed, the two plots look nearly identical as expected. The gap distances recorded were used in Paschen's voltage breakdown equation, equation 2, to determine their accuracy. Figure 90 shows a comparison of the data recorded and the breakdown voltage calculated using the respective recorded distances, illustrating the accuracy of the data recorded.

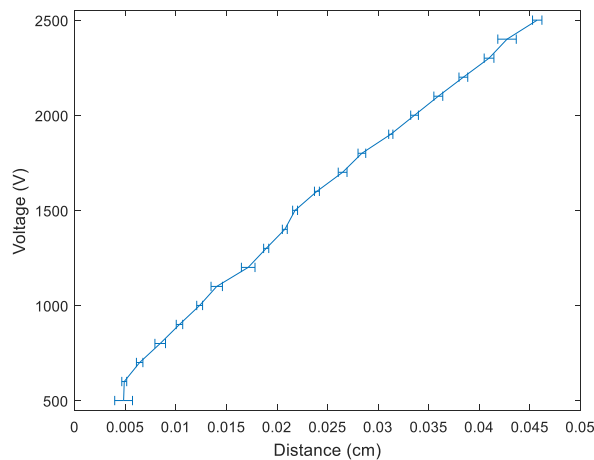


Figure 89: Breakdown voltage as a function of average gap distance. Error bars represent the standard deviation recorded over five measurements with each applied voltage.

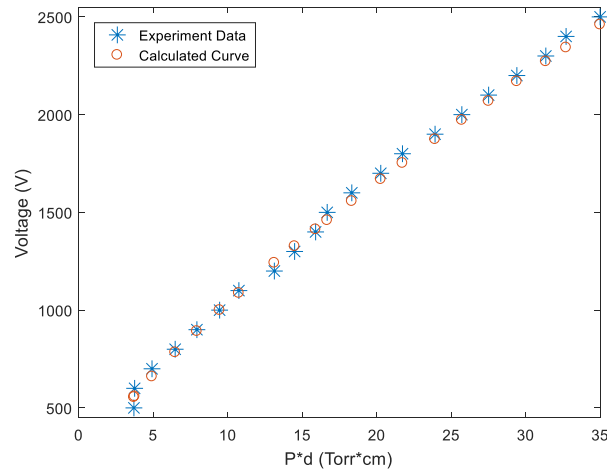


Figure 90: Breakdown voltage plotted as a function of the product of chamber pressure and breakdown gap distance, for both experimental and calculated data.

The next three sets of experiments are those collected when vented electrolyte filled the chamber using the procedure discussed earlier. Each series of experiments are identical with the only difference being the applied voltage. A 1 kV lithium-ion battery will have an open circuit potential around 1 kV but a conduction voltage that varies between roughly 0.75k V and 1 kV. Though there is no reason that the potential should go over 1 kV, but in the event it does, voltages of 0.75 kV, 1 kV, and 1.25 kV were chosen for evaluation here. In each series of experiments, three LFP lithium-ion cells were vented and as many measurements as could be recorded with each were made. The data presented with an applied voltage of 0.75 kV, 1.0 kV, 1.25 kV are plotted in Figures 91, 92, and 93 respectively.

In each of the three plots, similar trends are observed with the gap distances being slightly wider, between 10% and 20% on average, when vented electrolyte is present in the chamber. Though there is some variation within the measurements, there are no significant outliers that would bring any uncertainty to the data. When evaluating the results, it is important to remember the discussion earlier about the breakdown potentials of CO₂, H₂, and air for a given *pd* product. The hypothesis discussed earlier appears to be verified that the breakdown potential is slightly higher than that of

air due to the high CO₂ volume but that it may be slightly reduced from that expected of CO₂ due to the presence of H₂ and other smaller volume chemical contents. What is verified here is that the presence of H₂ and the other contents does not dramatically impact the breakdown potential meaning that in the design of a high voltage battery, it is likely sufficient to design dielectric gaps assuming an air dielectric with the appropriate safety factors accounted for.

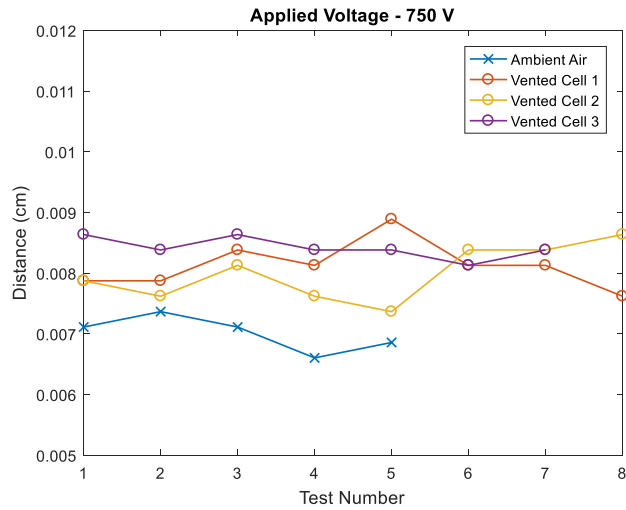


Figure 91: Breakdown distance measured multiple times from three identical vented LFP cells as well as ambient air, respectively, with an applied gap potential of 0.75 kV.

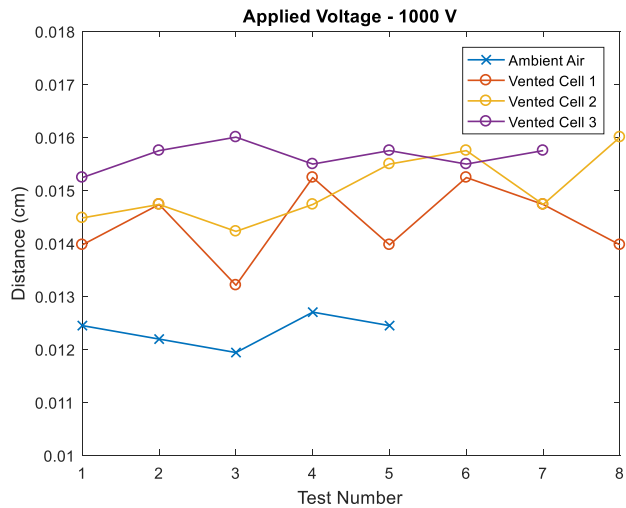


Figure 92: Breakdown distance measured multiple times from three identical vented LFP cells as well as ambient air, respectively, with an applied gap potential of 1.0 kV.

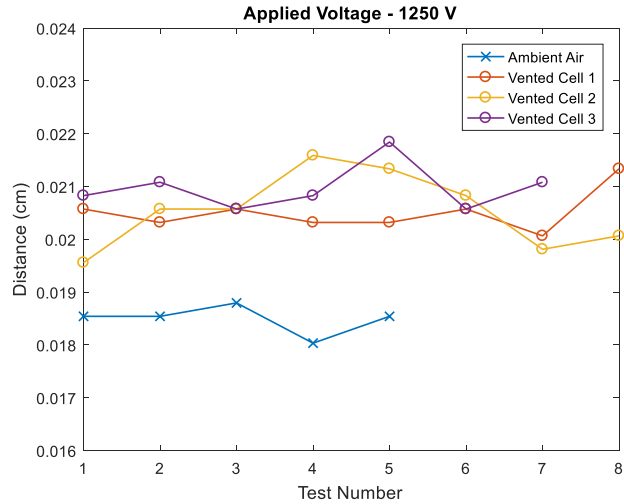


Figure 93: Breakdown distance measured multiple times from three identical vented LFP cells as well as ambient air, respectively, with an applied gap potential of 1.25 kV.

Conclusion

The results from ambient air testing proves to be relatively linear over the voltage range tested, meaning that the curve plotted in Figure 90 is part of the linear section of the Paschen curve. Also according to Figure 89 the standard deviation for each voltage is low, the largest being $\pm .001$ cm, proving that the breakdown electrode gap distance does not vary much during testing. With the preliminary, ambient air, testing complete and verified to be accurate the testing then involved venting the LFP gases into the chamber to determine its effect on dielectric strength.

The three voltages investigated are 0.75 kV, 1 kV, and 1.25 kV, as seen in Figures 91-93. According to the data the LFP gases did in fact have an effect on the dielectric strength of the test chamber environment. For all three voltages the breakdown electrode gap distance increased in the presence of the vented gases. The breakdown distance increase due to the vented LFP gases ranged anywhere from .001 - .003 cm, meaning the gases vented into the test chamber increased the dielectric strength by a small amount. The results prove promising for storage purposes, so that

the specified clearance or method of storage in ambient air conditions will not cause problems in the event of battery failure and the presence of vented LFP gases.

Chapter 5: Final Conclusion

The work presented here was aimed in an effort to investigate the challenges of integrating electrochemical energy storage into high voltage distributed generation power system architectures. Several experiments were conducted using LFP batteries and UCs as a means of electrochemical energy storage to determine their impact to mobile and stationary microgrid applications. The first experiment performed was an effort to characterize a number of different UC's, three EDLCs and two LICs, with similar characteristics to conduct a like-for-like comparison. In this effort three separate tests were conducted to each cell, EIS for an impedance characterization, single transient discharge to verify each cells impedance and to evaluate each cell's transient power density, and finally repetitive transient cycling to evaluate electrical and thermal characteristics. This information is essential when designing energy storage as a buffer for high voltage distributed generation power system, such as mobile and stationary microgrids.

From the data collected it is apparent that Skeleton Technologies use of curved graphene instead of traditional activated carbon to coat their electrodes had a large payoff. This technology significantly lowered their cell's ESR and therefore increased its overall power density, allowing the cell to source significantly more transient power than the other cells tested. Its low ESR also allowed the cell to be cycled at higher rates without generating as much heat as the other UCs. This could be quite beneficial depending on the intended use or the location of the energy storage module. The other two EDLCs, Maxwell and Ioxus, had very similar results throughout all three tests but fall short of the performance of the Skeleton cell due to their higher impedance. The two LICs tested, JM Energy and General Capacitor, both have a significantly higher ESR due to their

chemistry. Though they may be more energy dense than the EDLCs they are lacking in transient power and are likely not a solution for buffering transient loads of microgrids. Of the modules tested two stand out, the Ioxus 96 V and the Skeleton 170 V modules. Both modules were potted, allowing for optimal dissipation and they both had liquid cooling capabilities. Although the Ioxus 96 V module performed well during its testing, Skeleton Technologies' 170 V module was ultimately able to cycle at higher rates without reaching thermal cutoff making it a more viable solution for buffering transient loads.

The second experiment conducted was a product of tests performed in 2015 when concerning voltage transients were witnessed during an experiment. With electrochemical energy storage used as a buffer in high voltage systems, it is essential to determine methods to suppress dangerous transients. For this study three methods of transient suppression were investigated for their effectiveness at mitigating inductively induced voltage spikes. The three methods include, TVS diodes, MOVs, and an active transient suppression device. Between the TVS diode and the MOVs it was clear that the TVS diodes were able to suppress the voltage transient induced much more effectively. Of the three MOVs tested none of them appeared to have a large impact on the magnitude of the transients produced. The active designed was the most capable suppression technique of all three. The active designs were able to clamp the transients at a lower voltage and the final active design allowed for its clamping voltage to be adjusted. Making the final active design the most effective and the most versatile device to protect energy storage devices.

The final experiment performed was to investigate the effects of vented electrolyte on the dielectric strength of the surrounding air. Once the severity of the voltage transients induced was realized, there was concern that if a battery had vented its electrolyte and a transient were to occur, it could cause failure propagation due to the effects in the surrounding air's dielectric

strength. Therefore the experiment was constructed to simulate this event by filling a chamber with the vented electrolyte of an LFP battery and breakdown was induced. The distance between electrodes at the time of breakdown in the vented electrolyte environment was compared to the distance recorded when breakdown was induced in ambient air. The results show that the vented electrolyte from an LFP battery slightly strengthened the surrounding air's dielectric strength. Therefore the specified clearance or method of storage in ambient air conditions will not cause cell failure propagation in the event of battery failure and the presence of vented LFP gases in mobile or stationary microgrids.

Disclaimer

This material is based upon work supported by US Office of Naval Research (ONR) under contract numbers in support of the ONR Multi-function Energy Storage Module (MF-ESM) program. The author would like to express thanks to ONR for their continued support. Any opinions, findings, and conclusions or recommendations expressed in this publication are those of the author and do not necessarily reflect the views of the US Office of Naval Research.

References

- [1] "Lithium iron phosphate battery", *En.wikipedia.org*, 2017. [Online]. Available: https://en.wikipedia.org/wiki/Lithium_iron_phosphate_battery. [Accessed: 19- May- 2017].
- [2] A. Golubkov, D. Fuchs, J. Wagner, H. Wiltsche, C. Stangl, G. Fauler, G. Voitic, A. Thaler and V. Hacker, "Thermal-runaway experiments on consumer Li-ion batteries with metal-oxide and olivin-type cathodes", *RSC Adv.*, vol. 4, no. 7, pp. 3633-3642, 2014.
- [3] E. Roth and C. Orendorff, "How Electrolytes Influence Battery Safety", *Interface magazine*, vol. 21, no. 2, pp. 45-49, 2012.
- [4] Elena Danila, "History of The First Energy Storage Systems," *3rd International Symposium on the History of Electrical Engineering and of Tertiary-level Engineering Education*, Oct. 2010.
- [5] T. E. of E. Britannica, "Alessandro Volta," *Encyclopædia Britannica*, 07-Mar-2019. [Online]. Available: <https://www.britannica.com/biography/Alessandro-Volta>. [Accessed: 26-Mar-2019].
- [6] M. Wang, S. Tan, C. Lee and S. Y. Hui, "A Configuration of Storage System for DC Microgrids," in *IEEE Transactions on Power Electronics*, vol. 33, no. 5, pp. 3722-3733, May 2018.
- [7] G. Iwanski, P. Staniak and W. Koczara, "Power management in a DC microgrid supported by energy storage," *2011 IEEE International Symposium on Industrial Electronics*, Gdansk, 2011, pp. 347-352.

- [8] H. Bašić, T. Dragičević, H. Pandžić and F. Blaabjerg, "DC microgrids with energy storage systems and demand response for providing support to frequency regulation of electrical power systems," *2017 19th European Conference on Power Electronics and Applications (EPE'17 ECCE Europe)*, Warsaw, 2017, pp. P.1-P.10.
- [9] "How does a battery work," *Mit Engineering*. [Online]. Available: <https://engineering.mit.edu/engage/ask-an-engineer/how-does-a-battery-work>. [Accessed: 26-Mar-2019].
- [10] Batteryuniversity.com. (2019). *Advantages and limitations of the Different Types of Batteries - Battery University*. [online] Available at: https://batteryuniversity.com/learn/archive/whats_the_best_battery [Accessed 11 Feb. 2019].
- [11] Burke, A. (2000). Ultracapacitors: why, how, and where is the technology. *Journal of Power Sources*, 91(1), pp.37-50.
- [12] Blomquist, Nicklas. (2016). Large-Scale Nanographite Exfoliation for Low-Cost Metal-Free Supercapacitors. 10.13140/RG.2.2.36561.33126.
- [13] D. A. Dodson, "Design, Evaluation, and Modeling of Medium Voltage DC Energy Conversion Testbed with Emphasis on Electrochemical Energy Storage," Publication Pending
- [14] J. Thongam, et al. "All-electric ships—A review of the present state of the art," *8th International Conference and Exhibition on Ecological Vehicles and Renewable Energies*, pp. 1-8, March 2013

- [15] Next Generation Integrated Power System, NGIPS Technology Development Roadmap, Ser 05D / 349, November 30, 2007.
- [16] D.A. Wetz, P.M. Novak, B. Shrestha, J.M. Heinzl, and S.T. Donahue, 'Electrochemical Energy Storage Devices in Pulsed Power,' *IEEE Transactions on Plasma Science*, Vol. 42, No. 10, Part 2, pp. 3034 – 3042, October, 2014.
- [17] D.A. Wetz, B. Shrestha, and P.M. Novak, 'Pulsed Evaluation of High Power Electrochemical Energy Storage Devices,' *IEEE Transactions on Dielectrics and Electrical Insulation*, Vol. 20, No. 4, pp. 1040 – 1048, August, 2013.
- [18] Cohen, I.J.; Wetz, D.A.; Kelley, J.P.; Heinzl, J.; Donahue, S., "Evaluation of a high rate hybrid energy storage module (HESM)," *Electromagnetic Launch Technology (EML)*, 2014 *17th International Symposium*, vol., no., pp.1, 7, 7-11 July 2014
- [19] Office of Naval Research. "Hybrid Energy Storage Module (HESM): Amendment 001" 13-SN-0007 [Online]. Available: <http://www.onr.navy.mil/~media/Files/Funding-Announcements/Special-Notice/2013/13-SN-0007-Amendment-0001.ashx>. [Accessed 10 Dec 2013]
- [20] "What are TVS diodes", *SEMTECH.com*, 2017. [Online]. Available: http://www.semtech.com/images/promo/What_are_TVS_Diodes.pdf. [Accessed: 05- Apr- 2017].
- [21] "Product Catalog & Design Guide", *Littelfuse.com*, 2013. [online] Available at: https://www.littelfuse.com/~media/electronics/product_catalogs/littelfuse_tvs_diode_catalog.pdf [Accessed 11 Oct. 2018].

- [22] "Varistor | Metal Oxide Varistor - Littelfuse", *Littelfuse.com*, 2017. [Online]. Available: <http://www.littelfuse.com/products/varistors.aspx>. [Accessed: 13- Feb- 2017].
- [23] "Truth About MOVs - Zero Surge", *Zero Surge*, 2017. [Online]. Available: <https://zerosurge.com/truth-about-movs>. [Accessed: 05- Feb- 2017].
- [24] L. Berzak, S. Dorfman and S. Smith, "Paschen's Law in Air and Noble Gases", p. 1, 2006.
- [25] Friedrich Paschen (1889). "Ueber die zum Funkenübergang in Luft, Wasserstoff und Kohlensäure bei verschiedenen Drucken erforderliche Potentialdifferenz (On the potential difference required for spark initiation in air, hydrogen, and carbon dioxide at different pressures)". *Annalen der Physik*. 273 (5): 69–75
- [26] C. Helling, M. Jardine, C. Stark and D. Diver, "Ionization in Atmospheres of Brown Dwarfs And Extrasolar Planets. III. Breakdown Conditions for Mineral Clouds", *The Astrophysical Journal*, vol. 767, no. 2, p. 136, 2013.
- [27] High-voltage engineering, 1st ed. New Delhi: M. S. Naidu, V. Kamaraju, p. 234.
- [28] "Gaseous Breakdown & Paschen's Law", *Home.earthlink.net*, 2017. [Online]. Available: <http://home.earthlink.net/~jimlux/hv/paschen.htm>. [Accessed: 18- May- 2017].
- [29] "Electrostatics and Surface Physics Laboratory", *Physics.ksc.nasa.gov*, 2017. [Online]. Available: <https://physics.ksc.nasa.gov/CurrentResearch/Breakdown/Breakdown.htm>. [Accessed: 19- May- 2017].
- [30] Oldham, K. B. "A Gouy-Chapman-Stern model of the double layer at a (metal)/(ionic liquid) interface." *J. Electroanalytical Chem.* Vol. 613, No. 2, 2008, pp. 131–38.

- [31] "Supercapacitor," *Implement generic supercapacitor model - Simulink*. [Online]. Available: <https://www.mathworks.com/help/physmod/sps/powersys/ref/supercapacitor.html>. [Accessed: 13-Mar-2019].
- [32] C. N. Nybeck, D. A. Wetz, D. A. Dodson and J. M. Heinzl, "Investigation of the Dielectric Breakdown Strength of Vented Li-Ion Electrolyte," in *IEEE Transactions on Plasma Science*, vol. 46, no. 10, pp. 3438-3443, Oct. 2018.

Biographical Statement

Charles N. Nybeck was born in Arlington, Texas in 1991, and received the B.Sc. degree majoring in electrical engineering from The University of Texas at Arlington in 2016. He then went to work as a Graduate Research Assistant with The University of Texas at Arlington, pursuing a Ph.D. in the Pulsed Power & Energy Laboratory under the supervision of Dr. David A. Wetz. His research interests include microgrid applications, electrochemical energy storage, control systems, and power systems design.